

A Suspended Fiber Network Platform for the Investigation of Single and Collective Cell Behavior

Puja Sharma

Dissertation submitted to the faculty of the Virginia Polytechnic Institute and State University
in partial fulfillment of the requirements for the degree of

Doctor of Philosophy

In

Biomedical Engineering

Amrinder S Nain, Chair

Bahareh Behkam

Jerry S Lee

Rafael Davalos

Yong Woo Lee

John Robertson

June 30, 2016

Blacksburg, Virginia

Keywords: Leader cell, Nanofiber, Cell migration, Mechanobiology, Gap closure

A Suspended Fiber Network Platform for the Investigation of Single and Collective Cell Behavior

Puja Sharma

ABSTRACT

Cells interact with their immediate fibrous extracellular matrix (ECM); alignment of which has been shown influence metastasis. Specifically, intra-vital imaging studies on cell invasion from tumor-matrix interface and wounds along aligned fibers describe invasion to occur as singular leader (tip) cells, or as collective mass of a few chain or multiple tip cells. Recapitulation of these behaviors *in vitro* promises to provide new insights in how, when and where cells get the stimulus to break cell-cell junctions and ensue invasion by migrating along aligned tracks. Using Spinneret based Tunable Engineered Parameters (STEP) technique, we fabricated precise layout of suspended fibers of varying diameters (300, 500 and 1000 nm) mimicking ECM dimensions, which were interfaced with cell monolayers to study invasion. We demonstrated that nanofiber diameter and their spacing were key determinants in cells to invade either as singularly, chains of few cells or multiple-chains collectively. Through time-lapse microscopy, we reported that singular cells exhibited a peculiar invasive behavior of recoiling analogous to release of a stretched rubber band; detachment speed of which was influenced with fiber diameter (250, 425 and 400 $\mu\text{m/hr}$ on small, medium and large diameter fibers respectively). We found that cells initiated invasion by putting protrusion on fibers; dynamics of which we captured using a contrasting network of mismatched diameters deposited orthogonally. We found that vimentin, a key intermediate filament upregulated in cancer invasion localized within a protrusion only when the protrusion had widened at the base, signifying maturation. To develop a comprehensive picture of invasion, we also developed strategies to quantify migratory speeds and the forces exerted by cells on fibers. Finally, we

extended our findings of cell invasion to report a new wound healing assay to examine gap closure. We found that gaps spanned by crosshatch network of fibers closed faster than those on parallel fibers and importantly, we reported that gaps of 375 μm or larger did not close over a 45-day period. In summary, the methods and novel findings detailed from this study can be extended to ask multiple sophisticated hypotheses in physiologically relevant phenomenon like wound healing, morphogenesis, and cancer metastasis.

A Suspended Fiber Network Platform for the Investigation of Single and Collective Cell Behavior

Puja Sharma

GENERAL ABSTRACT

Disease phenomenon like cancer invasion and wound healing have a myriad of things in common including cell migration and the ability of cells to remodel their immediate environment. Often times these singular or group migratory events of cells are initiated and directed by peculiar cells called tip/leader cells that explore cellular environment and make room for migration. While research in the last few decades has yielded a tremendous wealth of information as to how biochemical factors influence their behavior, our understanding of how the biophysical properties of the environment affect their behavior is in its infancy. This lack of understanding can somewhat be attributed to the difficulty in fabricating mechanically well-defined substrate systems that can be tailored to recapture these invasive episodes in a controlled setting outside of a living organism. In this study, we utilize a novel Spinneret based Tunable Engineered Parameters (STEP) technique to fabricate mechanically tunable nanofibers that show close resemble to native cellular environment. Cells were made to interact with these fibers and it was shown for the first time that factors like fiber spacing, diameter and topography can significantly affect the types of leader cells and their trajectory. Furthermore, once these cells come out of the simulated tumors/wounds, their migratory behaviors were still affected by mechanical properties of the fibers. Similarly, we also showed for the first time that the ability of the gaps to close in simulated wound healing settings could be significantly dependent on size, shape, and properties of fibers. These findings offer a novel outlook to our current understanding of single and collective cell behavior and how the biophysical properties of the native cellular environment can affect these behaviors. This can not only expand our understanding of how this invasive episodes occur, but also help us come up with preventive

measures to inhibit such episodes for a better prognosis of diseases like cancer and chronic wounds.

To Mamu, Buwa and Rupen

Acknowledgement

I am grateful to a lot of people who have inspired, mentored and supported me throughout my time at Virginia Tech. Here is my humble attempt to thank some of them.

First of all, I would like to thank my advisor Dr. Nain for motivating me to work hard, helping me appreciate the little things in life, and helping me grow as a researcher. I will forever value his guidance and mentorship. I would also like to thank Dr. Behkam, Dr. Lee, Dr. Robertson, Dr. Lee and Dr. Davalos for agreeing to serve on my Ph.D. committee and for providing me with helpful research insights as I developed my research projects. I am equally grateful to the School of Biomedical Engineering, especially, Dr. Clay Gabler, Ms. Tess Sentelle, Ms. Pam Stiff and Ms. Amanda Covey for helping and supporting me with administrative tasks. This would not have been possible without the incredible support of my colleagues Kevin, Ji, Zhou, Colin, Brian, Sean, Tim, Amritpal, AhRam, Abinash, Aniket, Shikha, Carrie, Appy, Alex, Paige, Goeff, Josiah, Aziz, Stephen, Tracee, Megan, Yuxin, Jack, Brendon, Eduardo, Sapna, Austin, and Ian from STEP and MicroN BASE labs. Working together with all of you has been fun and rewarding. I wish you all the best for your future endeavors in your respective lives.

Finally, I am extremely thankful for my family and friends who were always there when I needed them. Thank you Mamu for everything you have done for me, Buwa for always encouraging me, and Phuchu for being an awesome brother. Thank you Raisha, Pallabi, Manisha, Nanin, Chetana, Shraddha, Ebu, Isha, Apsana, Supriya, Ashmita, Sudha, Prativa, Sadikshya and 600/0 'C' friends for patiently listening to me, encouraging me, and uplifting my spirits when I needed it. I feel extremely blessed to have you all in my life.

Attribution

Chapter 3:

Brian Koons (MS, Mechanical Engineering, 2015): Brian Koons worked on manufacturing small, medium and large diameter fiber with circular cross sections.

Zhou Ye (PhD Candidate, Mechanical Engineering, 2016): Zhou Ye worked on manufacturing the flat nanofibers, and analyzing the protrusion dynamics of cancer cells on flat diameter fibers.

Dr. Meng Horng Lee (Postdoctoral Fellow, Johns Hopkins University, 2016): Meng Horng Lee worked on silencing the cytoskeletal protein vimentin using shRNA technique. We were provided with vimentin knockout versions of DBTRG-05MG and MDA-MB-231 cells in order to investigate the influence of vimentin on protrusion formation.

Chapter 5: Published in Integrative Biology, 2013

Dr. Kevin Sheets (PhD, Biomedical Engineering, 2013): Kevin Sheets is a co-author on the paper and helped performed initial experiments on blebbing dynamics of DBTRG-05MG cells.

Dr. Subbiah Elankumaran was an associate professor of Virology at the Virginia-Maryland College of Veterinary Medicine. He is a co-author on the paper and helped with manuscript editing.

Dr. Amrinder S. Nain is an associate professor of Mechanical Engineering at Virginia Tech. He is a co-author on the paper and helped in design of the experiments and manuscript editing.

Chapter 6: Published in Biofabrication, 2014

AhRam Kim (MS, Mechanical Engineering, 2015): AhRam Kim is an equal contributing author on the paper. She worked on manufacturing of the force scaffolds, and performing experiments and analysis of glioma cell-force measurements.

Amritpal Gill (MS, Mechanical Engineering, 2015): Amritpal Gill is a co-author on the paper and worked on glioma cell force measurement experiments and analysis.

Dr. Ji Wang (PhD, Biomedical Engineering and Mechanics, 2015): Ji Wang is a co-author on the paper and worked on mechanical characterization of fibers to measure structural stiffness of the fibers using a three point bending test using Atomic Force Microscopy (AFM).

Dr. Kevin Sheets (PhD, Biomedical Engineering, 2013): Kevin Sheets is a co-author on the paper and worked on cell-force measurement experiments.

Dr. Bahareh Behkam is an associate professor of Mechanical Engineering at Virginia Tech. She is a co-author on the paper and helped in design of the experiments and manuscript editing.

Dr. Amrinder S. Nain is an associate professor of Mechanical Engineering at Virginia Tech. He is a co-author on the paper and helped in design of the experiments and manuscript editing.

Chapter 7:

Colin Ng (MS, Mechanical Engineering, 2013): Colin Ng is a co-author on the manuscript, and performed initial experiments on wound healing using poly (lactic-co-glycolic acid) or PLGA scaffolds.

Paige Szymanski (BS Candidate, Bioengineering, 2015): Paige Szymanski is a co-author on the manuscript, and worked together on the analysis of suspended cell sheet migration dynamics (Figure 7.2E, H and I).

AhRam Kim (MS, Mechanical Engineering, 2015): AhRam Kim worked together on preliminary experiments involving collective fibroblast migration on STEP nanofibers.

Harrison Bolinger, Luke Grant, Giancarlo DiBase, Drew Smith, Ryan Grove, Liam Han, Mark Healy, and Yuxin Zheng (Undergraduate volunteers): They helped analyze the closure dynamics of parallel and crisscross scaffolds (Fig. 7.1G). Graduate student volunteers Aniket Jana and Abinash Padhi helped in the analysis of cell stream dynamics (Fig. 7.1F)

Table of Contents	Page
List of Abbreviations	xiii
List of Figures	xiv
Chapter 1: Overview	1
1.1 Importance of fiber based platforms for probing cell behavior	1
1.2 Research Objectives	1
1.3 Organization of the document	2
Chapter 2: Introduction	4
2.1 Motivation	4
2.1.1. Cell-microenvironment interactions	4
2.1.2. Cell, fibrous microenvironment and diseases	6
2.2 Comparable technologies to probe cell behavior	9
2.3 Lack of tunable suspended fibrous platforms: the STEP Advantage	11
2.4 Using STEP fibers to facilitate the formation of leader cells	13
2.5 Summary	14
Chapter 3: Leader cell formation and detachment dynamics	16
3.1 Introduction	16
3.2 Materials and Methods	20
3.3 Results and Discussion	24
3.4 Conclusion	43
Chapter 4: Spheroid dynamics on STEP nanofibers	45
4.1 Introduction	45
4.2 Materials and Methods	46
4.3 Results and Discussion	48
4.4 Conclusion	49
Chapter 5: Migration and blebbing dynamics of single glioma cells	51
5.1 Introduction	51
5.2 Materials and Methods	54
5.3 Results	57
5.4 Discussion and Conclusion	63
Chapter 6: Single glioma cell forces	66
6.1 Introduction	66
6.2 Materials and Methods	69
6.3 Results and Discussion	72
6.4 Conclusion	79

Chapter 7: Collective cell migration dynamics	82
7.1 Introduction	82
7.2 Materials and Methods	84
7.3 Results	89
7.4 Discussion and Conclusion	98
Chapter 8: Project summary and concluding remarks	100
8.1.1 Leader cell formation and detachment dynamics	103
8.1.2 Single cell-nanofiber interactions	104
8.1.3 Collective cell migration dynamics	106
8.2 Deliverables	107
Chapter 9: Impact and future directions	110
9.1 The bigger picture	110
9.2 Future Directions	111
9.3 Publications	113
References	117
Appendix A	141
Appendix B	144

List of Abbreviations

AFM: Atomic Force Microscopy

ANOVA: Analysis of Variance

CL: Chain Leader

DAPI: 4', 6'-diamino-2-phenylindole

DMEM: Dulbecco's Modified Eagle's Medium

ECM: Extracellular Matrix

FBS: Fetal Bovine Serum

FCS: Fetal Calf Serum

nN: nanoNewton

PBS: Phosphate Buffered Saline

PS: Polystyrene

PU: Polyurethane

RLC: Recoiling Leader Cell

SCS: Suspended Cell Sheets

SD (also DS): Double Suspended

SS: Single Suspended

STEP: Spinneret based Tunable Engineered Parameters

TACS: Tumor Associated Collagen Signatures

List of Figures

Figure	Page number
Figure 3.1. The influence of fiber spacing on the generation of the type of fibroblast leader cells. The relative percentage of chain leader cells coming off of a single fiber (A), and double fibers (B) as a function of fiber spacing (Chain cells: small diameter N=60, medium diameter N=136, large diameter N=52). The percentages of recoiling leaders coming off of the fibers at various fiber spacing are shown in C (small diameter N=70, medium diameter N= 165, large diameter N=52). Small: 200nm, Medium: 500nm, Large: 1000nm diameter fibers.....	25
Figure 3.2. Time lapse images of recoiling and chain leaders (A, B). Migration dynamics of RLC and CL: C) cell displacement of CL (N=21) and RLC (N=156) at various stages of detachment, D) persistence (displacement/distance) of CL and RLC after detachment, E) the number of cells following the leader cells. RLC and CL interactions with neighboring cells: F) number of cells in contact, G) circumferential cell contact length, and H) the time the leader cell is in contact with at least one cell.....	26
Figure 3.3. RLC and CL cell morphology analysis: A) cell length, B) cell width, C) aspect ratio, D) cell-fiber gap, E) angle, and F) cell area.....	28
Figure 3.4. The migration dynamics of a recoiling leader cell. (N=165).....	30
Figure 3.5. The influence of conditioning time and recoiling angle on cell length of RLC before detachment. (N=165).....	31
Figure 3.6. (A-C) Cell morphological factors that have the least, (D-F) some, and (G-I) the most influence on recoiling speed. (N=165).....	32
Figure 3.7. Increasing recoiling speed (A) and kinetic energy (B) of RLC as potential energy increases. (N=165).....	33
Figure 3.8. RLC displacement dynamics without (A, N=165), with 10 μ M (B, N= 106), and 20 μ M (C, N= 80) γ -27632 exposure. Max displacement (D) and persistence (E) of RLC without, with 10 μ M, and 20 μ M γ -27632.....	35
Figure 3.9. Schematic diagram showing the base and protrusion fiber (A), scanning electron micrographs of the fibers (B) and protrusion dynamics of DBTRG-05MG and MDA-MB-231 cells on flat and round fibers (C).....	37
Figure 3.10. Vimentin and protrusion lengths and eccentricities of a MDA-MB-231 cell in a typical protrusion extension (A (i)), The average eccentricity of the protrusion when vimentin first appears in a protrusion (A (ii)), Protrusion length and eccentricity diagrams of MDA-MB-231 and DBTRG-05MG WT and shVim cells (B), and a time lapse image of a MDA-MB-231 cell protrusion and its respective vimentin expression on the right (C).....	38
Figure 3.11. Average maximum protrusion lengths of DBTRG-05MG (A) and MDA-MB-231 (B) with (shVim) and without (WT) vimentin silencing. N=10 for each. No statistically significant differences were observed.....	39
Figure 3.12. Protrusion maturation representative profiles of small (A), medium (B) and large (C) diameters. Blue line represents the length of the protrusion and red line represents eccentricity (E).....	40

Figure 3.13. The influence of changing (A) cell length, B) aspect ratio, and C) cell area of RLC on detachment speeds. Average D) detachment speed, E) change in aspect ratio, F) change in area, G) displacement 1 hour after detachment, H) slip distance, and I) conditioning times of RLC on different diameter fibers. (Small, N= ; Medium, N= ; Large, N=).....41

Figure 3.14. Recoiling MDA-MB-231 (A) and ZR751 (B), chain T47D (C), and recoiling DBTRG-05MG (D) leader cells from the monolayer (shown by an arrow). Scale bar is 50 μ m.....42

Figure 4.1 Time lapse images showing retraction of a cell stream (shown by arrow). Scale bar is 50 μ m.....48

Figure 4.2. Time lapse images showing the migration of spheroids along the fibers (A), merging of two adjacent spheroids (B) and the area and circularity of the spheroid over time (C).....48

Figure 4.3 Time lapse images of a leader cell detaching from a spheroid (A), and detachment speed of leader cells (N=72) as a function of spheroid area (μ m²).49

Figure 5.1 Optical images of cellular morphologies on SS: (i) spindle (indicated by arrow), (ii) rectangular (indicated by rectangle)), and on SD nanofibers (iii) (circular (indicated by *), spindle (indicated by arrow), rectangular (indicated by rectangle) and polygonal (indicated by triangle), Immunostained images of DBTRG-05MG cells (iv) on flat, (v) spindle shaped on a single nanofiber, (vi) rectangular between two parallel nanofibers, and (iv) polygonal on an intersection of two orthogonal nanofibers. Stains: blue (DAPI, nucleus), red (Phalloidin, F-actin), and green (Alexa Fluor ®, focal adhesion paxillin). Scale bar = 50 μ m.....57

Figure 5.2 Time lapse of a single DBTRG-05MG migrating along a single nanofiber at 10 minute intervals. (i) and (ii) show the extension of leading edges (marked by arrows) , and (iii) and (iv) show retraction of the trailing edge. Cell does not bleb when spread (i) and (ii), and starts blebbing (shown by *) once the spread area reduces (iii), and (iv). Scale bar = 50 μ m.....58

Figure 5.3 (i) DBTRG-05MG migration on flat (N=14), single suspended (SS, parallel, N=56), and double suspended (SD, orthogonal , N=62) nanofibers \pm SE of lengths 6mm. Statistical difference was observed between migration on flat, SS, and SD nanofibers (Student’s t-test, p=0.0004 for SS-flat, p=0.0294 for SD-flat, and p=0.0171 for SS-SD), (ii) Cell migration of single DBTRG-05MG cells on single suspended (SS, parallel) fibers \pm SE. Cells migrated significantly faster on fibers of lengths 10mm (N=60), 6mm (N=101) and 4mm (N=120) compared to flat (N=14). Statistically significant differences were observed between all lengths (Student’s t-test, p<0.0001 for 10mm-flat, 10mm-4mm, 6mm-flat, 4mm-flat, p=0.0001 for 10mm-6mm, and p=0.0439 for 6mm-4mm). The average structural stiffness within 750 μ m either sides from the center of the 4, 6, and 10mm nanofibers was experimentally determined to be 3.4, 1.5, and 0.75 mN/m respectively. * shows statistical significance.....59

Figure 5.4. DBTRG-05MG cell blebbing dynamics. (I) Continuous plasma membrane blebbing of DBTRG-05MG on flat, (II) While the spread cell has no blebs, the circular cell (shown with an arrow) is blebbing on suspended fiber networks, (III) Actin (Phalloidin) immunofluorescent stain of a blebbing DBTRG-05MG. The bleb actin cytoskeleton (white arrow) of the bleb is separated from the actin cortex (blue arrow). Scale bars are 20 μ m, 50 μ m

and 5µm for (I), (II), and (III) respectively, (IV) Time lapse images at 20 minute intervals of DBTRG-05MG cell blebbing dynamics on STEP fibers (shown using arrow). Blebbing decreases or disappears as cell spreads along the nanofibers (b, c, f, i, j, l), and increases or reappears as cells reduce their spreading area (a, d, e, g, h, k). Scale bar is 50µm. Respective cell spread areas are shown on top right corners.....61

Figure 5.5. Increasing cell spread area inversely influenced both bleb occurrence and size in single DBTRG-05MG cells (i) Bleb size for cells with spread area 150-650µm² (N=109) was significantly higher than those for areas 651-1150 µm² (N=80), and 1151-1650µm² (N=36) (Student’s t-test, both p<0.01). Bleb size for cell spread area 651-1150 µm² was almost significantly higher than those for areas 1151-1650µm² (Student’s t-test, p=0.05). (ii) Similarly, bleb count for cell spread area 150-650µm² was significantly higher those for areas 651-1150µm² and 651-1150µm² (Student’s t- test, p<0.01 for 150-650µm²-651-1150µm² and 150-650µm²-1151-1650µm², p=0.02 for 651-1150µm²-1151-1650µm²). * shows statistical significance.....62

Figure 5.6. Blebbing DBTRG-05MG cells migrate slowly. DBTRG-05MG cell migration was significantly slower for blebbing cells (N=31) compared to those that were not blebbing (N=30) (ANOVA, p=0.002). * shows statistical significance.....62

Figure 6.1. Scanning electron microscopy (SEM) images of suspended STEP nanonets showing: (i-ii) orthogonal patterns of bigger and smaller diameter fibers, and (iii) fused fiber junctions. The scale bars are 100, 2 and 1 µm respectively. Schematic illustrations of the STEP based force measurement probes: (iv) inside-out, and (v) outside-in.....70

Figure 6.2. A single DBTRG-05MG cell exerting forces on two parallel fibers. Once exposed to 2 µM cytochalasin D, the ‘inside-out’ forces exerted by the cell decreases. The respective time scales and force values have been shown on top left corner and next to the deflecting fibers respectively. Original position of fibers are shown by dotted line and fused nodes by stars. Scale bars are 50 µm.....73

Figure 6.3. A single DBTRG-05MG cell after being strained by a micropipette (shown by *). The ‘outside-in’ force (shown by arrow) exerted by the cell is calculated by the deflection of the bottom trailing fiber (shown by dotted line). Scale bars are 50 µm.....73

Figure 6.4. ‘Inside-out’ forces exerted by a single DBTRG-05MG cell over time. The maximum deflections of the small diameter fiber have been shown by arrows. Original profile of the fiber is shown by dotted white lines, and the fixed boundary conditions are shown by black stars in 1 hour panel. Scale bars are 50 µm.....74

Figure 6.5. ‘Inside-out’ migratory forces exerted by single DBTRG-05MG cells under the influence of 0.5 µM cytochalasin D. Scale bars are 50 µm.....75

Figure 6.6. Average ‘inside-out’ forces exerted by single DBTRG-05MG cells without (N=116), and with 0.05 µM (N=10), 0.1 µM (N=45), 0.2 µM (N=63), and 0.5 µM (N=49) cytochalasin D exposure. Forces reported were measured after thirty minutes exposure to the drug. Error bars represent standard errors.....75

Figure 6.7. Changing cell spread area of single DBTRG-05MG cells with and without exposure to 1 µM cytochalasin D. Respective cell spread areas and times have been shown on the top right and left corners respectively. Scale bars are 50 µm.....77

Figure 6.8. Changing cell spread area of single DBTRG-05MG \pm standard error (SE) over time with (0.05: N=13, 0.1: N=10, 0.2: N=15, 0.5: N=11, 1: N=8, 2: N=10, 3 μ M: N=9) and without (N=15) exposure to cytochalasin D.....77

Figure 6.9. A series of time lapse images showing a single DBTRG-05MG cell exposed to 2 μ M cytochalasin D being stretched by a probe. As the drug exposure time increases, the ‘outside-in’ force (shown by decreasing fiber deflection) decreases. The position of the undeflected fiber has been shown by dotted lines, the fixed points of the fiber by stars, and the respective times and forces on top left and right corners. Scale bars are 50 μ m each.....78

Figure 6.10. ‘Outside-in’ forces exerted by single DBTRG-05MG cells under the influence of 0.05 μ M (N=35), 0.2 μ M (N=31), and 2 μ M (N=24) cytochalasin D concentrations over time. Error bars indicate standard errors.....79

Figure 7.1. Cell emergence modes, cell stream dynamics and gap closure. (A) A schematic illustration of cell seeding, and cell stream/sheet advancement on the suspended STEP nanofibers. (B) Cells leading the monolayer exhibiting three distinct emergence modes: *single recoil leaders*, *chain* and *collective* groups. (C) Schematic illustrating cell stream and SCS. Detailed time-lapse images of (D) cells leaving monolayer, and (E) cell streams and SCS. (F) Cell stream increase in length and width over days (n=10), and black dot represents the lengths when SCS advancement reached at least 100 μ m. (G) The influence of fiber architecture on global gap closure. SS represents parallel (number of substrates, N=7), and DS (number of substrates, N=9) represents crosshatch patterned fibers. (H) Optical images of DS and SS closure over two-week period. (I) local gaps (circular (i) and oval (ii)) formation (both on DS and SS, Supplementary movies 5 and 6). Scale bars are 25 μ m for B, 100 μ m for D, 500 μ m for E and H, and 50 μ m for I.....88

Figure 7.2. SCS and Cell stream advancement on SS fibers. (A) Normalized average number of cell streams (normalized with respect to average number of cell streams on day 6), (B) average distance between the cell streams, and (C) average suspended cell sheet advancement distance over time \pm SE (number of cell streams (n): 2400), (D) Representative schematics and time-lapse images of cell stream and SCS advancement over time. Scale bars are 200 μ m. (E, F) Examples of coordinated (in-phase and out-of-phase) advancement of SCS showing displacement over time of different SCS. (E, G (i)) Percentages of coordinated and uncoordinated advancement of SCS relative to their position and a (G (ii)) detailed analysis of the coordinated SCS migration behavior (number of SCS (n): 201). Examples of SCS front advancement distance over time shown by black arrows for SCS spanning (H) 60 μ m and (I) 250 μ m. Scale bars are 100 μ m.....92

Figure 7.3. Closing vs. non-closing gaps. (A) Circularity and area of gaps that closed and did not close over a period of 45 days (number of individual gaps (n): 49) ; Relevant studies from literature shown as star (scratch wound assay $>1,000,000\mu\text{m}^2$ closed within 20 days²²⁹), triangle (gaps created on flat surface using PDMS pillars of approximate area $500\text{-}18,000\mu\text{m}^2$ closed within approximately 14.5 days²²⁸), and rectangle (suspended gaps of about $5,000\mu\text{m}^2$ observed, but closure dynamics not shown²⁰³); (B) Optical mosaic images of gaps that closed and did not close. (C) The circularities of nucleus and their respective distances from the edge of gaps that closed (green, n= 305), and did not close (red, n= 485); (D) Immunostained images of a gap that did not close over 45 days showing oval nuclei along the edge of the gap; (Red= Actin, Blue= Nucleus). Scale bars are 500 μ m for B, 100 μ m for D and 50 μ m for inset in D.....93

Figure 7.4. Shape factor and aspect ratio driven gap size distribution: The frequency distribution of (A) Shape Factor (number of gap areas (n): 1094), and (B) Aspect Ratio (number of gap areas (n): 1360) of the gaps $<40,000 \mu\text{m}^2$ with representative images from time-lapse movies. Scale bars are $50 \mu\text{m}$, (C) Gap area as a function of aspect ratio (n=819). No gaps were observed in shaded region, suggesting large area gaps to not be elongated ovals (high aspect ratio). Scale bars are 200 and $50 \mu\text{m}$ respectively for gaps with areas $39,900$ and $4,300 \mu\text{m}^2$**95**

Figure 7.5. Kinetics of small local gap closure and the influence of y-27632. Changing gap areas over time for gaps without (A, number of individual gaps (n): 25), and with y-27632 exposure (B, black=without, blue= $10 \mu\text{M}$, and green= $20 \mu\text{M}$ y-27632). The horizontal dotted line indicates slower closure rates for gaps $<10,000 \mu\text{m}^2$. Similarly, closure rates of gaps $<10,000 \mu\text{m}^2$ show significantly faster closures when exposed to 10 (n=20) and 20 (n=38) μM y-27632 concentrations compared to those not (n=25) exposed to the drug. Respective changes in major and minor axes of the gaps (C) without, with (D) $10 \mu\text{M}$, and (E) $20 \mu\text{M}$ y-27632 exposure. (F) Color contour representation of closure speed variation in response to gap shape, with circular gaps having similar closure rates from each principle direction, and elliptical gaps favoring closure from high curvature and low span distance ($\Delta' < \Delta$) direction.....**97**

Figure A1 (i) Schematic of non-electrospinning, STEP nanofiber manufacturing platform, (ii-iii) electron micrographs of highly aligned parallel fibers in single direction (Single Suspended, SS) and (Double Suspended, SD) fibers respectively, (iv-v) schematics of possible nanofiber deposition with user desired diameters (example: d_1 and d_2), and spacing (example: Δ_1 and Δ_2); SS and SD respectively.....**141**

Figure A2: Fixed boundaries are validated by observing no fiber movement at the passive fiber interface (blue circles). Scale bars are $50 \mu\text{m}$ **143**

Figure B1. Mosaic images of entire simulated wound gaps over time for SS and SD scaffolds. Scale bars are $500 \mu\text{m}$**144**

Figure B2. Schematic representation of gap closure on SS (A) and DS (B) fibers.....**145**

Figure B3. Temporal relationship between SCS and cell stream advancement distances. Arrow demonstrating compromised SCS advancement beyond $375 \mu\text{m}$ cell stream separation distance (A, total number of SCS (n): 2400). Absolute velocities of SCS as a function of cell stream distance (B, total number of cell streams (n): 644).....**145**

Figure B4. Migration dynamics of (A) uncoordinated, (B) combined in phase and out of phase SCS advancement, and (C) SCS advancement dynamics as a distribution of stream separation differences.....**145**

Figure B5. Nucleus area of the cells surrounding local gaps as a function of their distance from the edge. Gaps that closed (number of nuclei (n): 305), and gaps that did not close (number of nuclei (n): 485).....**146**

Figure B6. The distribution of shape factor for local wound gaps (number of gap areas (n): 2400)..... **146**

Figure B7. Size dynamics of local gaps over time when exposed to 10 (number of individual gaps (n): 8) and $20 \mu\text{M}$ (number of individual gaps (n): 19) y-27632.....**147**

Figure B8. A schematic of the measurements for aspect ratio, circularity and shape factor of a local gap.....**147**

Figure B9. Immunostained images of cell monolayers showing the arrangement of cells on a flat substrate (A), and on SS or DS suspended fiber networks (B). (Red= Actin, Blue= Nucleus). Scale bars are 100 μm for A and 50 μm for B. Single cell migration pathways on SS (C, number of cells (n): 26) and DS (D, number of cells (n): 25) fibers.....**148**

Chapter 1: Overview

1.1 Importance of fiber based platforms for probing cell behavior

Cells constantly interact and obtain biochemical and biophysical cues from their immediate fibrous extracellular matrix (ECM). While research in the last decade has highlighted the importance of bulk biophysical properties of the ECM in influencing cell behavior, recent studies have demonstrated that local level ECM properties like pore size, alignment, and fiber size can have a stronger impact on the behavior of cells. As the ECM is a major driver of various physiological phenomenon like morphogenesis, immune response, wound healing, and cancer metastasis, it is imperative that we invest in understanding cell-fiber interactions better. Hence, a platform that allows for repeatable manufacturing of mechanistically tunable fibers with user defined properties is highly warranted. Most platforms currently available in literature do not allow for repeatable control of mechanistic properties of the fibers. Hence, our knowledge of single cell-fiber interactions is limited.

1.2 Research objectives

In this proposed study, we utilized a previously explained non-electrospinning Spinneret based Tunable Engineered Parameters (STEP) technique to manufacture highly aligned suspended polymeric nanofibers of known fiber properties like elasticity (N/m^2), structural stiffness (N/m), fiber diameter, alignment, spacing and architecture. This platform allows cells to align along the direction of the fiber, wrap around the fiber to be influenced by fiber diameter, the elastic modulus, and architecture of the fiber layout thus, providing an opportunity to investigate the influence of each on cell behaviors.

The overarching goal of this work was to understand single and collective cell-nanofiber interactions in order to facilitate the design of suspended nanofiber scaffolds that encourage the formation of leader cells. Given the importance of cell-ECM interactions in wound healing

and cancer metastasis, single and collective cell behaviors of fibroblast, breast cancer and glioma cells have been investigated.

Specifically, the influence of fiber properties on single cell detachment from monolayers and spheroids in order to identify fiber properties that encourage the formation of leader cells, the influence of fiber properties on single cell behaviors including cell migration and force generation, and the influence of fiber architecture on collective cell migration and gap closure dynamics have been investigated.

1.3 Organization of the document

The document provides a comprehensive outline of studies performed using the STEP technique to interrogate single and collective cell behaviors. Furthermore, it investigates specific properties of fibers in order to address the overarching hypothesis that metastasis occurs by a biophysical conditioning phase causing cells to become migratory leaders partly in response to biophysical cues obtained from its immediate fibrous environment. In particular, Chapter 2 describes the importance of using fiber based platforms to study cell behavior, current technologies used, the uniqueness of the STEP system, and its novel use in the study of leader cell formation. Chapter 3 describes the use of STEP fibers in interrogating the mechanobiological changes of a leader cell as a function of fiber diameter. It proposes that fibroblast cells are conditioning their detachment by first protruding onto the fibers and detaching as leader cells depending on the properties of the fibers. It also describes protrusions and cytoskeletal protein vimentin interactions as glioma and breast cancer cells interact with the STEP fibers. Chapter 4 describes spheroid formation dynamics on STEP nanofibers. As published in the *Integrative Biology* journal, Chapter 5, describes the influence of structural stiffness and spread area on migration and blebbing dynamics of glioma cells. Similarly, Chapter 6 (as published in the *Biofabrication* journal) describes the use of nanonets capable of measuring cell forces with and without the influence of actin polymerization inhibitor

cytochalasin D. Chapter 7 describes the use of STEP nanofibers in interrogating the influence of fiber architecture in collective migration and gap closure dynamics of fibroblasts. Chapter 8 summarizes the project and highlights the deliverables of each of the chapters, and Chapter 9 describes the potential impact of the results obtained from the study along with suggested future experiments. The references are listed in Chapter 10, and the mathematical formula used to calculate the cell forces in Chapter 6 is presented in the Appendix as Chapter 11.

Chapter 2: Introduction

2.1. Motivation

2.1.1. Cell-microenvironment interactions

Cells are constantly interacting with their immediate extracellular matrix (ECM). The ECM is an organized meshwork composed of fibrous proteins like collagen, elastin, laminin and fibronectin with polysaccharides like glycosaminoglycans, hyaluronic acid and proteoglycans. While polysaccharides form a gel like hydrated matrix, the fibrous proteins serve as adhesive sites for the cells to attach^{1,2}. A transmembrane protein called integrin binds to specific proteins on the ECM and facilitates the formation of focal adhesion complexes which are cell-ECM contact points³⁻⁵. A focal adhesion complex (FAC) can incorporate an incredibly complicated array of over 50 different proteins that contribute to establish a connection between the cytoskeleton and the ECM *via* integrin. Some of the common proteins recognized by integrin include fibronectin, collagen and laminin. Inside the cell, actin fibers assemble at the FAC and help the cell communicate with their immediate ECM⁶⁻⁹.

Previously thought of as a dormant scaffold for cell attachment, it is now well understood that the cells obtain vital biochemical and biophysical cues from their microenvironment¹⁰. While the influence of biochemical and genetic factors are relatively well understood, the effects of biophysical properties of the environment on cells have only been recognized in the last few decades. Cells also condition and optimize their microenvironment in order to maintain homeostasis¹¹. One of the important cell-ECM interactions involves the exertion of force. Stable focal adhesions activate Rho-associated protein kinase (ROCK) which inhibits myosin light chain (MLC) phosphatase. Inhibition of MLC phosphatase allows myosin to remain phosphorylated and able to interact with actin in order to produce actin-myosin based

contractions¹². Focal adhesion based actomyosin contractions allow cells to exert contractile force and remodel the architecture of the fibers when necessary. Such changes in the ECM can also result in changes in gene expression. Simultaneously, mechanical stimulations like force, stress and mechanical properties of the ECM like stiffness can instigate changes in focal adhesion patterns and initiate ROCK activation, actomyosin contraction or changes in gene expression¹³⁻¹⁵.

One of the elegant studies that demonstrate the influence of microenvironment elasticity (N/m²) on differentiation of mesenchymal stem cells (MSCs) was presented by Engler *et al* in 2006¹⁶. They observed that MSCs that were cultured on soft polyacrylamide gels (E: 0.1-1kPa) exhibited branched morphology and neurogenic markers, those on stiffer gels (E: 8-17kPa) showed spindle morphology and myogenic markers, and those of rigid gels (E: 25-40kPa) showed polygonal morphology and osteogenic markers. Additionally, they showed that by inhibiting nonmuscle myosin II using blebbistatin, the elasticity based differentiation of MSCs was compromised. Similarly, the mechanobiology community has extensively investigated how the mechanical properties of the environment influences different cell behaviors. Studies have shown that properties like cell migration speed^{17,18}, directionality¹⁹, persistence, cellular tension²⁰, cell-cell contact force^{21,22}, cell traction force, cell migration force, and focal adhesion patterns²³ can be influenced by mechanical properties of the substrate. These changes in cell behaviors result from a constant two way biochemical and biophysical interaction between the cell and its immediate microenvironment. Such two way communications between a cell and the microenvironment help operate highly coordinated negative and positive feedback loops to maintain tensional or ECM homeostasis²⁴.

2.1.2. Cell, fibrous microenvironment and diseases

While ECM homeostasis is required to maintain normal physiological conditions, controlled remodeling of the ECM is vital to various physiological phenomenon including morphogenesis²⁵, embryogenesis²⁶, immune responses, wound healing^{27,28}, and diseased conditions like cancer metastasis²⁹. Genetic mutations leading to the production of defective ECM proteins have been shown to cause tissue defects and embryonic lethality in some cases. For instance, lack of one type of laminin in the small intestine basement membrane of mice causes a substitution by another laminin subtype ultimately changing the architecture of the small intestine³⁰. Similarly, ECM deposition and remodeling are crucial during development of intestines, mammary gland and lung where ECM cleavage facilitates the initiation of a side branch, and aligned collagen fibers guide epithelial cells during sprouting^{25,31,32}. Proper functioning of bone also relies on regulated breakdown and synthesis of the ECM, and when ECM breakdown is enhanced, osteoarthritis occurs³³.

The ECM also plays a critical role during wound healing. A normal wound healing process can be divided into inflammation, proliferation and remodeling phases. During the proliferation phase of wound healing, neighboring fibroblasts migrate into the wound and deposit collagen fiber rich ECM in a matter of days to weeks after injury. The deposited matrix is highly infused with blood vessels and neutrophils, and called the granulation tissue. Using granulation tissue as its base, epithelial cells migrate and cover the wound site. Similarly, the fibrous structure of the granulation tissue acts as a bridge for fibroblasts to help remodel the ECM architecture and strengthen the wound³⁴⁻³⁶.

Often referred to as a wound that does not heal, a tumor is very similar to a wound and is associated with phenomenon like vascularization, cell migration and fibrous scaffolding. Tumor cells constantly interact with their immediate fibrous ECM and sometimes utilize it to

migrate off of the primary tumor³⁷. Studies measuring the mechanical properties of a tumor have therefore repeatedly reported enhanced stiffness in tumors. Similarly, high mammographic densities have been associated with poor breast cancer prognosis^{38,39}, and liver cirrhosis has been shown to increase the chance of liver cancer by 20-30%⁴⁰. On the other hand, heterogeneous mechanical properties of a tumor have also been reported in literature. By using indentation-type atomic force microscopy (IT-AFM), Plodinec *et al* have showed that while normal and benign breast tissue exhibit unimodal stiffness (about 1-6kPa) profiles, their malignant counterparts exhibit a heterogeneous stiffness morphology. The stiffness measurements from human breast cancer biopsies demonstrated specks of very high stiffness (up to 18kPa) towards the core of the tumor to a non-uniform distribution of stiffness ranging from 1-18kPa towards the tumor periphery⁴¹.

Besides bulk mechanical stiffness of breast tissues, the alignment and orientation of collagen have been strongly correlated with invasive properties of breast cancer⁴²⁻⁴⁹. Numerous studies show that while normal breast tissue exhibit wavy collagen fiber patterns, collagen fibers surrounding the edge of the tumor become perpendicularly aligned to the tumor as the tumor progresses. This association of aligned collagen structures and highly invasive breast tumors is highly repeatable. Hence, they have been defined as tumor associated collagen signatures (TACS) that serve as indicators of poor breast cancer prognosis. Similarly, studies that have investigated the microarchitecture of collagen matrices independent of gel concentration and bulk stiffness have shown that the microarchitecture of collagen fibers that are in immediate contact with the cells have a higher influence on cell behavior. In particular, Carey *et al* showed that despite similarities in bulk stiffness of collagen, MDA-MB-231 cells exhibited higher polarity and motility when the fibers were larger with higher pore sizes, and rounded morphology with decreased motility when the fibers were smaller with lower pore sizes. Their results show that proliferation of MDA-MB-231s was dependent on bulk stiffness of collagen

gels⁵⁰. Similarly, a recent study by Riching *et al* demonstrated that the efficiency of MDA-MB-231 migration was influenced more by collagen fiber topography than stiffness (N/m²)⁴⁵. They observed that aligned collagen fibers decreased cellular protrusions of migrating cancer cells in directions other than that of the aligned fibers, increased directional persistence, and helped the cells migrate further. The speed of the cells, on the other hand, was not affected by fiber topography. These studies strongly suggest that the local fiber architecture and mechanical properties can have greater influence on initiation of metastasis, perhaps even stronger than the influence of bulk properties of the material. Furthermore, these studies highlight the importance of ECM alignment during cancer cell migration. These studies show that aligned ECM fibers not only enhance persistence of migrating cells by serving as a track for cellular migration, but such aligned structures could be used as diagnostic markers to isolate highly metastatic cancer cells.

The relationship between alignment and cancer metastasis is not limited to TACS in breast cancer. Studies have shown that glioma cells like to migrate using axon bundles called the white matter tracts in the central nervous system^{51,52}. These bundles of axons are categorized into three major types: association fibers which connects parts of the same hemisphere, commissural fibers which connect the gray areas of the left and right hemispheres, and projection fibers which are connected to the spinal cord⁵³. The fibers range from less than 500nm to 7 μ m in diameter, and serve as efficient migration tracts for glioma cells to migrate from one part of the brain to another⁵⁴⁻⁵⁶.

These studies highlight the importance of understanding cell-fibrous ECM interactions. Particularly in the context of cancer, the role of single cell-fibrous ECM interactions rather than the influence of bulk mechanical properties have been shown to be critical. While the role of alignment in enhancing the efficacy of metastatic breast cancer cells is undeniable, the precise mechanisms and mechanical properties of ECM fibers that trigger such metastatic events are

not well understood. Hence, studies probing the underlying local interactions of single cell-fibrous ECM are warranted. Influence of how local microenvironment properties like alignment, porosity, fiber curvature, stiffness can shed light to the not so well understood biophysical triggers for metastasis. Similarly, the knowledge gained from cell-fibrous ECM interactions can be applied to better understand wound healing and treatment of chronic wounds like diabetic ulcers and burn wounds.

2.2 Comparable technologies to probe cell behavior

Cells are simultaneously interacting with numerous biophysical and biochemical cues from their microenvironment *in vivo*. While understanding the cumulative influence of these cues is important, decoupling these factors to study the effects of each is difficult *in vivo*. Hence, researchers have adopted various *in vitro* platforms to investigate the influence of both biochemical and biophysical cues on single and collective cell behaviors.

Widely used traditional platforms include plastic and glass well plates⁵⁷. Cost effectiveness, ease of imaging, ability to fluorescently label desired intercellular components, and the ability to produce high throughput analysis of various cell behaviors have made these platforms extremely popular. These 2D platforms have also been modified to cater the study of specific cell behaviors. For instance, in order to study wound healing, scratch and cell exclusion assays including Woundmaker, Radius exclusion assay, and CytoSelect have been produced^{58,59}.

Similarly, chamber type platforms including Boyden, multiwell and Dunn chambers have a porous filter sandwiched between a layer of cells and a chemoattractant, and are used to investigate cell invasion and protrusion dynamics studies^{60,61}. Also, the filter component of the chambers have been replaced with native basement membrane to investigate the cytoskeletal dynamics of cancer specific protrusions called invadopodia⁶². Microfluidic devices that are

able to establish desired chemical gradients have also been used to investigate the influence of chemoattractants on cell behavior⁶³.

Platforms that probe cell force transmission dynamics include micropillars⁶⁴, fluorescent bead infused gels⁶⁵, atomic force microscopy (AFM)⁶⁶, and micropipette aspiration⁶⁷. Using photolithography techniques, polydimethylsiloxane (PDMS) micropillars of known dimensions and mechanical properties can be manufactured and used as cantilevers whose deflection forces can be back calculated based on micropillar deflections caused by cells interacting with the micropillars. Similarly, cell traction forces can also be calculated by tracking the movement of fluorescent beads embedded in gels of known mechanical properties. AFM utilizes the interaction between cells and cantilevers of known stiffness to study mechanical properties of cells including cell force dynamics. Aspiration of cells using micropipettes have been used to study mechanical properties of cells such as cell stiffness and plasma membrane elasticity. Similarly, polymeric gels (example: polyacrylamide, PDMS) of known stiffness have been manufactured to investigate cell differentiation, migration and gene expression.

While these platforms have yielded a wealth of information on biophysical cell-substrate interactions, they do not recapitulate the fibrous architecture of the ECM. Cell behavior observed on platforms that do not resemble the ECM may not necessarily correlate with what happens *in vivo*. For instance, while cell migration is primarily dictated by filopodial and lamellipodial actin structures on 2D flat substrates, migration of cells in 3D hydrogels have been described using blebbing based phenomenon^{68,69}. Hence, platforms that offer a closer resemblance to the fibrous ECM are necessary. Some examples of platforms that do bear closer resemblance to the ECM include matrigels which are protein structures derived from mouse sarcoma cells^{70,71}, collagen gels^{15,72}, and brain slices⁷³. These platforms provide cells with an

environment that closely resembles the native ECM, and hence, the results obtained from using these platforms can be inferred as similar to what happens in the body.

Besides the use of cell derived platforms like matrigel, the biomedical engineering community has seen a tremendous increase in the use of fiber based platforms to interrogate cell behaviors. The popular use of nano-microfiber based platforms can be attributed to the fact that the diameter of the polymeric fibers can be engineered to closely represent those of collagen fibers (30nm-20 μ m) in the native ECM. Electrospinning is one of the most popular methods to generate polymeric fibers⁷⁴⁻⁷⁷. A polymeric solution exiting from a needle is made to interact with an electric field that extrudes nano-micron scale fibers off of a Taylor cone formed at the end of the polymeric solution reservoir. The fibers are collected on either a stationary conductive plate or a rotating drum. By altering the polymer solution concentration and electric parameters, fibers with desired properties can be manufactured. Not only have electrospun fibers been used to study cell-fiber interactions, their applications in tissue engineering is also being increasingly recognized. Namely, diameter of electrospun have been shown to affect neurite growth and migration of Schwann cells⁷⁸. A more complicated version of electrospun fibers include the incorporation of degradable polymer which elicits the controlled release of a chemical substance that can aid in the differentiation of stem cells⁷⁹. Given the immense potential of fibrous platforms in studying cell-fiber interactions, it is highly desirable to produce fibers with repeatable user defined properties like diameter, alignment, porosity, topography, architecture and degradability.

2.3 Lack of tunable suspended fibrous platforms: the STEP Advantage

Spinneret based Tunable Engineered Parameters (STEP) is a novel non-electrospinning technique that allows for the manufacturing of highly repeatable nano-micron sized polymeric

fibers with user defined parameters like diameter, spacing, orientation, alignment, and material properties⁸⁰⁻⁸³. These fibers can be up to centimeters in length, and can be manufactured to have diameters in the range 50nm- micron. Similarly, the alignment and spacing of the fibers can be highly controlled by the user to be within 2.5° and several μms respectively^{81,84}.

Pioneered by Amrinder Nain in 2008, the STEP technique does not use electricity to generate nano-micron diameter fibers^{80,83}. Briefly, a polymeric solution of known concentration is placed in a glass micropipette attached to a syringe that applies pressure. Upon contact with a substrate, the polymeric solution gives off a fine protrusion of the solution that forms a nanofiber upon reaching the end of the substrate in contact. The nanofiber collecting substrate can be mounted to a motor stage in order to control the spacing of the fibers. Also, fiber junctions of hierarchical layers of fibers can be fused using a solvent treatment method to fuse multiple layers of fibers to form a netlike structure. Using hollow plastic frames, regions of suspended and aligned fibers can be formed. These fibers can be used to study the influence of different mechanical properties of the fibers on cell behavior.

Until now, stem cell differentiation⁸⁵, cell shape and migration control⁸⁶, blebbing dynamics⁸⁷, focal adhesion patterns^{18,86}, nucleus shape¹⁸, collective cell migration, protrusion dynamics, forces exerted by cells⁸⁸, and the response of cells to outside forces include some of the cell behaviors investigated using the fibers manufactured by the STEP technique. Repeatable spindle, rectangular and polygonal shaped cells were formed in response to fiber architecture which also influenced their migration speeds *via* preferential focal adhesion clustering in the direction of the fiber⁸⁶. Furthermore, structural stiffness of the fibers (N/m) have been shown to elicit significant migration, focal adhesion cluster length and nucleus shape changes in a myoblast cell line¹⁸. The influence of structural stiffness independent of material elastic modulus was also observed in glioma cells where fibers of low structural stiffness elicited high migration speeds. Also, the relationship between cell spread area and blebbing dynamics of

glioma cells was investigated and found that cell spreading decreases both the occurrence and size of blebs in glioma cells⁸⁷. Likewise, collective cell migration dynamics of fibroblast have been shown to depend on fiber architecture with crisscross patterned fibers accelerating *in vitro* gap closure. In particular, it has been shown that closure of gaps is dependent on their shape and size. Similarly, formation of spheroids upon retraction by cell clustered streams was also observed. Protrusion dynamics of glioma and breast cancer cells have been shown to be dependent on the cell type and fiber diameter. Similarly, forces exerted by glioma cells and their response to outside forces were measured to be in nN range. Upon exposure to actin polymerization inhibition drug cytochalasin D, glioma cells demonstrated significant decrease in cell spread area and force⁸⁸.

2.4 Using STEP fibers to facilitate the formation of leader cells

An important part of collective cell migration is the presence of leader cells that coordinate the migration procedure. Leader cells have been identified in the context of wound healing²⁷, malignancy^{89,90}, mammary, salivary gland^{91,92}, and *Drosophila* tracheal system formation⁹³. Their major roles include exploration of the native ECM, generation of traction forces and proteolytic cleavage of the ECM to make room for the migrating stream of cells⁹³. Often described to be initiated by chemical factors like transforming growth factor β (TGF β)⁹⁴, leader cells show distinct patterns that include obtaining spindle shaped long morphology, loss of apical basal polarity, transitioning of cell adhesion proteins from E-cadherin to N-cadherin, upregulation of proteins like Delta 1⁹⁵, extracellular signal-regulated kinase (Erk 1/2)⁹⁴, cytoskeletal reorganization including realignment of actin and penetration of microtubules in cellular protrusions²⁷, and upregulation of basal genes including cytokeratin K14 and p63⁸⁹. Platforms that have been used to investigate leader cell behavior include collagen gels, tumor organoids embedded in mice, and 2D well plates. While these platforms have identified several

biochemical components that initiate the formation of leader cells, the influence of biophysics on leader cell generation is relatively less understood. Owing to the fibrous nature of the ECM, it is important that we better understand how fiber biophysics influences the emergence of leader cells. Given the ability to control fiber alignment, spacing, diameter and material properties, the STEP platform serves as an ideal platform to investigate the influence of fiber biophysics on leader cell behavior. The work described here thus investigates single and collective cell-fiber interactions followed by a detailed investigation of leader cell formation and the influence of fiber biophysical properties in the generation of leader cells.

2.5 Summary

Given the recently recognized influence of cell-microenvironment, and in particular how single cell-fiber interactions may contribute to significant changes in cell migration and metastatic behaviors, a fiber based platform that allows the user to selectively and repeatedly control specific mechanical and architectural properties like elastic modulus, structural stiffness, fiber diameter and curvature, alignment and spacing is warranted. Although the influence of bulk mechanical properties of the ECM in diseased conditions have been well recognized, the importance of single cell level-ECM interactions cannot be underestimated. The major advantages of STEP technique over other fiber spinning platforms reported in literature are: highly repeatable control of a) diameter, b) spacing, and c) alignment of the fibers. Hence, allowing researchers to take a reductionist approach to investigating how single mechanical properties like structural stiffness independent of elastic modulus or fiber curvature could influence cell behaviors. Furthermore, selective design and manufacturing of fibers could allow the study of simultaneous influences of multiple aspects of a fiber. For instance, when a cell is interacting with a single fiber, it is able to sense the one dimensional direction of the fiber and align and polarize the cell body along the fiber. At the same time, it is able to wrap around the

fiber, and sense the curvature (as a function of fiber diameter) of the fiber. Similarly, the elastic modulus of the fiber would also be contributing to the behavior of the cell. By adopting a user defined design space of these properties, their individual and collective influence can be studied. While most of the knowledge in current literature of the influence of biophysics on cell behavior is based on bulk mechanical properties of the substrates the cells are interacting with, through this planned work, we propose to put forward the notion that single cell-fiber interactions are just as important in obtaining a comprehensive picture of how ECM biophysics influences cell behaviors. In doing so, the not so well understood questions like what biophysical factors tempt cells to migrate off of a primary tumor or into a wound can be better answered.

In order to obtain this, the proposed work has been divided into leader cell detachment study, single cell migration and blebbing dynamics study, and collective cell migration and gap closure study. Firstly, fibroblast detachment dynamics was investigated in detail as a function of fiber mechanical properties. In particular, leader cell evasion, and protrusion dynamics and its sensitivity to change in fiber properties was evaluated. The overall hypothesis that cell evasion occurs by a biophysical conditioning phase causing cells to become single migratory leaders partly in response to biophysical cues obtained from its immediate fibrous environment was addressed. Furthermore, the influence of structural stiffness (N/m) on glioma cell migration and force exertion was investigated in order to probe the behavior of highly invasive cancer cells. Finally, collective cell migration dynamics of cells was investigated. Specifically, collective cell stream, cell sheet and gap closure dynamics of fibroblast cells as they interacted with suspended and aligned nanofibers of different architecture was studied. The findings from the proposed work will not only add novel insights to the not so well understood realm of cell-fiber based interactions, but also potentially help better understand disease phenomenon like wound healing or metastasis.

Chapter 3:

Leader cell formation and detachment dynamics

3.1 Introduction

Single and collective cell migration starts with the initiation of leader cells. One of the early studies performed in 2003 described leader cells as cells near the edge of a monolayer that reorganized their cytoskeleton, realigned actin, disassembled marginal bundles and moved forward as microtubules penetrated the leading edge of the cells. They described a pivotal role of RhoA protein in the formation of leader cells where inhibition and constitutive expression of RhoA protein transformed most edge cells into leaders and suppressed the formation of leader cells respectively²⁷. Over the last decade, a wealth of studies have investigated the biochemical and biophysical factors that trigger the formation and corresponding changes that occur in leader cells. Formation of leader cells have been deemed important in many physiological phenomenon including wound closure⁹⁴, regeneration of corneal epithelium, *Drosophila* trachea, mammary gland and salivary gland formation⁹⁶⁻⁹⁸, and in diseased conditions like metastasis^{93,95}. The primary functions of leader cells include exploration of their native ECM, generation of tractional forces and proteolytic degradation of the native ECM to make room for the follower cells⁹³.

They have been shown to be triggered by several biochemical components including vascular endothelial growth factor (VEGF), fibroblast growth factor (FGF), epidermal growth factor (EGF), platelet derived growth factor (PDGF), insulin-like growth factor (IGF-1), stromal cell-derived factor (SDF-1), and transforming growth factor beta 1 (TGF β 1)^{93,94,99,100}. These biochemical signals have been shown to impact RhoA (Ras homolog gene family member A),

Rac1 (Ras-related C3 botulinum toxin substrate 1), Cdc42 (Cell division control protein 42), and FAK (Focal adhesion kinase) proteins in the leader cells, eventually causing them to obtain spindle morphology, losing apical basal polarity and migrate as leader cells⁹³.

Given the importance of leader cells, identification of factors that help transform a generic cell to a leader, distinguishing it from a follower cell has been important. Studies have proposed that leader cells are able to interact with the native ECM whereas the follower cells attach to degraded or reconstructed ECM. This allows the leader cells to engage different sets of integrin proteins (particularly $\alpha 2\beta 1$, $\alpha 5\beta 1$, and $\alpha 5\beta 3$) as opposed to follower cells (particularly $\alpha 6\beta 1$, and $\alpha 6\beta 4$) which could lead to differences in polarity amongst leader and follower cells^{99,101}. Similar to epithelial-mesenchymal transition (EMT) markers that include decreased E-cadherin⁹⁰, cytokeratin, and increased N-cadherin, and vimentin levels^{102,103}, studies in the past decade have established distinct leader cell markers. Precisely, Delta1 membrane protein^{93,95}, growth factor sensitivity, extracellular regulated kinase (Erk 1/2)⁹⁴, basal epithelial genes like cytokeratin-14 (K14)⁸⁹, p63 have been shown to be upregulated in leaders, whereas Notch protein in the follower cells. Specifically, while only about 1.4% of the cell population in a tumor organoid embedded in collagen gel consisted of K14+ve cells, 88% the leader cells emerging from the organoids were K14+ve. The study also showed that K14-ve cells were transitioning to K14+ve cells despite being treated by mitosis inhibitor aphidocolin. Furthermore, the invasive behavior of the leader cells was increased by the presence of collagen I indicating a clear influence of the native environment on leader cell behavior⁸⁹. Similarly, studies have also shown that biophysical factors like mechanical compression and access to free space enhanced migratory capacity of leader cells in breast cancer cell lines⁹⁰.

These studies in the last decade have used various *in vivo* and *in vitro* platforms such as 2D well plates, collagen gels, and mice. This has sometimes resulted in conflicting results that suggest that the leader cell-native environment relationship is not well understood. For instance, studies have suggested that a switch from cytokeratin to vimentin is an important factor during cell invasion¹⁰³. At the same time, leader cells coming out of a tumor organoid embedded in collagen gel showed no upregulation of commonly used EMT markers like Twist, Slug and vimentin⁸⁹. These results warrant that leader cell behavior could be substrate dependent. Hence, platforms that closely represent the native migratory environment of leader cells, and allow the user to decouple biochemical and biophysical components are warranted.

In this context, aligned ECM collagen fibers have been well recognized as one of the major indicators of poor prognosis of breast cancer. Over the progress of a tumor, a normal breast ECM which is primarily composed of collagen fibers in wavy patterns evolve to form highly aligned structures that lay perpendicular to the mass of the tumor^{42,44,104}. While the association of bulk mechanical property of the breast tissue like elastic modulus have been associated with higher grades of breast cancer, the biophysical factors that tempt cancer cells to migrate off of the tumor are not well recognized. Identifying biophysical triggers of metastasis in *in vivo* platforms is difficult as it is not possible to isolate individual cell-collagen fiber biophysical interactions among many biochemical and biophysical cues that are present in a native ECM. Among many, platforms that change the bulk properties of a substrate (example, collagen, matrigel and polyacrylamide gels) and study the resultant behavior of cells are popular. With the recognition of ECM collagen fiber alignment as a dominant feature in determining metastatic potential, studies in the last couple of years have focused on the microarchitecture of the gels. The highly repeatable pattern of aligned collagen fibers *in vivo* have been categorized as tumor associated collagen signatures (TACS) which facilitate the metastasis of

cells away from the tumor. Analogous to histologic evidence of aligned collagen structures, recent studies using collagen gels have shown that the microarchitecture of the collagen gel that is in contact with the cells have a higher influence on cell behavior than the bulk mechanical property of the substrate^{50,105}. In particular, they demonstrated that the pore size significantly changed polarization and migration of MDA-MB-231 cells independent of elastic modulus of the substrate⁵⁰. Similarly, directional persistence was observed to be significantly enhanced by alignment of collagen fibers where individual cell protrusions extending in directions other than the alignment of the fiber was observed to be highly reduced¹⁰⁵.

It is therefore highly imperative that further biophysical cues that can potentially trigger leader cell formation be identified. In particular, biophysical properties like the elastic modulus (N/m^2), structural stiffness (N/m), spacing, and curvature as a function of diameter can be investigated. In this study, we therefore utilize the previously reported Spinneret based Tunable Engineered Parameters (STEP) technique to manufacture nano-micron diameter polymeric fibers to closely represent the fibrous architecture of the native ECM. Keeping the elastic modulus of the substrate the same, the influence of fiber curvature as a function of fiber diameter have been investigated. An array of highly aligned polystyrene fibers of specific diameters (200nm, 500nm and $1\mu\text{m}$) were made to interact with a monolayer of fibroblast cells. The emergent cells that made their way to the fibers from the monolayer were termed leader cells and their migratory behavior was characterized. In particular, it was observed that leader cells either migrated as single cells in distinct recoiling patterns (hence termed ‘Recoiling’ cells), or pull along an array of follower cells while maintaining their cell-cell contacts (hence termed ‘Chain cells’). The migration dynamics of recoiling leader cells were observed to be influenced by the curvature of the fibers with cell migrating away from the monolayer at higher recoiling speeds when interacting with fibers of lower curvature (and high diameter). The

results obtained from the study can ultimately be used to better understand the role of fiber properties on the initiation of leader cells.

3.2 Materials and Methods

Scaffold preparation: Rectangular incisions were made into 300 μ m thick plastic cover slips (Fischer Scientific, Pittsburgh, PA) to create gaps of 2x3mm². Polystyrene (PS, Scientific Polymer Products, Ontario, NY, M_w : 2×10^6 g mol⁻¹) was dissolved in xylene (Fischer Scientific, Pittsburgh, PA) at 7% (w/w) to prepare a polymeric solution for fiber spinning. After at least 48 hours of solution preparation, the solution was extruded off of a glass micropipette to deposit 500nm diameter suspended and aligned fibers in parallel and cross-hatch patterns using the previously described Spinneret based Tunable Engineered Parameters (STEP) technique at 15% relative humidity and room temperature. The diameter of the fibers were confirmed with scanning electron micrograph measurements. In order to investigate the leader cell migration dynamics, fibers of a smaller (200nm) and larger (1 μ m) diameters were also manufactured. Fibers of diameters 94nm, 200nm and 545nm were manufactured by Brian Koons to investigate the influence of cancer cell protrusions and the role of vimentin in protrusion dynamics. Similarly, flat fibers of widths 300nm and 600 were manufactured by Zhou Ye in order to investigate protrusive behavior of breast cancer and glioma cells. These scaffolds were tacked down in glass bottom six-well dishes (MatTek Corp., Ashland, MA) using high vacuum grease (Dow Corning, Midland, MI). The scaffolds were sterilized with ultraviolet rays in a sterile Biosafety hood (1300 Series A2, Thermo Scientific, Waltham, MA) for twenty minutes before cell seeding.

Cell culture and seeding: NIH 3T3 mouse embryo fibroblast were obtained as generous gifts from Dr Jarvik, Carnegie Mellon University, Pittsburgh, PA. As recommended by the American Type Cell Culture (ATCC), these cells were grown in T25 cell culture flasks

(Corning Inc., Corning, NY) with Dulbecco's Modified Eagle's Medium (DMEM, HyClone, Logan, UT) and 10% bovine calf serum (ATCC, Manassas, VA). DBTRG-05MG (Denver Brain Tumor Research Group-05MG) cell line was purchased from ATCC (American Type Culture Collection, Manassas, VA). The cells were maintained in RPMI-1640 media (ATCC), supplemented with 10% FBS (HyClone, Canada), 1% Penicillin/Streptomycin (HyClone, Logan, UT), additional 30mg/L L-proline, 35mg/L L-cystine, 3.57g/L HEPES (4-(2-Hydroxyethyl)piperazine-1-ethanesulfonic acid), 15mg/L hypoxanthine, 1mg/L adenosine triphosphate, 10mg/L adenine, and 1mg/L thymidine (Sigma Aldrich, St. Louis, MO) as recommended by ATCC. The cell cultures were maintained at 37°C and 5% CO₂. MDA-MB-231 cells were purchased from ATCC and maintained in L-15 media (HyClobe, Loga, UT) with 10% FBS (ATCC) at 37°C. Vimentin silenced (shVim) DBTRG-05MG and MDA-MB-231 cells were obtained from Dr. Denis Wirtz, Johns Hopkins University, Maryland, USA. Before seeding the cells onto the STEP fibers, the cells were suspended in cell media as follows. Media from a T25 flask containing adherent cells was aspirated out and the adherent cells were rinsed with phosphate buffered saline (PBS, Fischer Scientific, Pittsburgh, PA) twice. They were then incubated with 500µl 0.25% Trypsin (HyClone, Logan, UT) for five minutes at 37°C and suspended in fresh cell culture media. Concentrated cell suspension was seeded on two plastic platforms adjacent to the suspended STEP fibers and the cells were allowed to attach overnight at 37°C and 5% CO₂ (MDA-MB-231 was cultured in CO₂ independent environment). After cell attachment, 2ml of cell culture media with 1% penicillin/streptomycin (HyClone, Logan, UT) was added to the well to facilitate further cell growth. The cell culture media was changed 2 to 3 times a week after rinsing the substrates with PBS.

Cells were transfected with LentiBrite GFP-Vimentin Lentiviral Biosensor (17-10152, EMD Millipore, Billerica, MA) in order to image for live vimentin activity in DBTRG-05MG and MDA-MB-231 cells. As recommended by Millipore, cells attached to STEP fibers of interest

were cultured with LentiBrite biosensor at 30 MOI (multiplicity of infection), with 400ul of media overnight. Additional 2ml of cell culture media was added to the wells after about 12 hours of incubation and the cells were incubated for 24 hours more. The media containing LentiBrite biosensor was then aspirated out, cells were washed with PBS twice, and 2ml of fresh cell culture media was added to the cells. The cells were imaged using a GFP filter 24 hours after the addition of fresh media.

Imaging: The scaffolds were imaged using a Zeiss microscope (Zeiss AxioObserver Z1, Jena, Germany) with incubating capacity (maintained at 37°C and 5% CO₂). Two distinct methods of imaging were used: a) phase contrast mosaic images of the scaffolds were obtained with a 10x objective every day up to two weeks after the first cells started migrating onto the suspended nanofibers, and b) time lapse phase contrast images were obtained using 20x and 40x objectives in order to investigate leader cell migration and local wound closure dynamics on STEP nanofibers every 3 to 10 minutes for up to 30 hour periods.

Data analysis

The mosaic images and time lapse videos were analyzed using AxioVision and ImageJ software.

Leader cell dynamics: Leader cells are defined as the cells that were able to make their way through the dense monolayer and eventually appear and migrate onto the suspended nanofibers. After observing distinct migratory patterns of leader cells, they were categorized into two major types: recoiling and chain. Leader cell dynamics were investigated using morphological and migratory metrics including cell area, length, width, angle and gap with the fiber it is associated with, the number of times it comes back to the monolayer, cell division occurrences, distance, displacement, persistence, the number of cells in contact during detachment, the length of

contact, the number of cells following the leader and cell division occurrences of the follower cells.

Recoiling leader cells exhibited an almost elastic detachment from the monolayer. In addition to the above metrics, the detachment dynamics of recoiling leader cells were further examined. Specifically, the Conditioning time which is the time from the first appearance of a leader cell protrusion on the nanofibers to cell detachment from the monolayer was recorded. Leader cell morphology was characterized by measuring cell area, aspect ratio (cell length to width), angle made by the cell with the fiber, and the gap distance between the cell body and the fiber before detachment. By measuring the distance covered by the cell (measured from the nucleus), the detachment speed of the leader cells were also calculated. In addition to detachment speed, the Slip distance of the cells was also measured. The Slip distance is defined as the distance from the tip of a leader cell protrusion before detachment to the maximum displacement of the cell after detachment from the monolayer. The morphology of the leader cell immediately after detachment was also characterized by measuring the cell area and aspect ratio. The kinetic and potential energy of the cells before and after detachment were also estimated. The potential energy of the cell was estimated by modelling it as a spring. Using a spring constant value (k) of 9.75mM/m obtained by Webster et al. for fibroblasts using Atomic Force Microscopy technique ¹¹, and change in cell length during cell detachment (x), the potential energy was calculated using the formula $\frac{kx^2}{2}$. Similarly, the kinetic energy of the cell during detachment was calculated using the formula $\frac{mv^2}{2}$ where cell mass (m) was considered to be 500pg as estimated by Grover et al. and detachment velocity (v) was measured using AxioVision ¹⁰⁶. Recoiling leader cells mostly obtained a bulb shaped morphology immediately after detachment. Hence, the amount of time taken for the cells to revert back to spindle morphologies were also measured. Additionally, the speed, displacement, and persistence of

the detached leader cells were measured up to one hour after detachment to investigate if the leader cells maintained their ballistic migratory nature.

Cancer cell protrusion dynamics was investigated by fitting an ellipse next to a cell protrusion and using an eccentricity parameter to fit the shape of the ellipse. Eccentricity values of 0 and 1 indicated rod like and triangular protrusions respectively. The protrusion and vimentin lengths were measured using AxioVision and the eccentricity of the ellipses were measured using ImageJ.

Statistical analysis Statistical analysis of the data was conducted using GraphPad Prism (GraphPad Software, Inc., La Jolla, CA) software. In particular, D'Agostino & Pearson omnibus normality test was used to determine the normality of the data. A non-parametric Kruskal-Wallis and two-tailed Mann-Whitney test or parametric ANOVA and two tailed-Student's t-tests were used to determine statistical significance depending on the normality of the data. A p-value of 0.05 was used to determine statistical significance. Standard errors were calculated and represented as error bars in the respective figures.

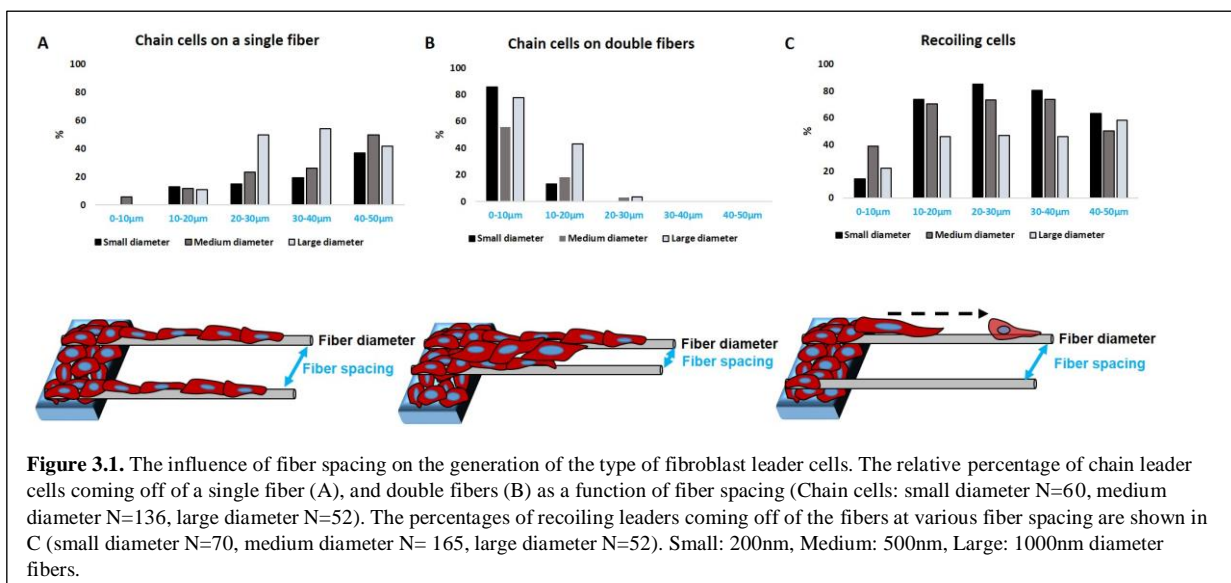
3.3 Results and Discussion

Leader cell dynamics

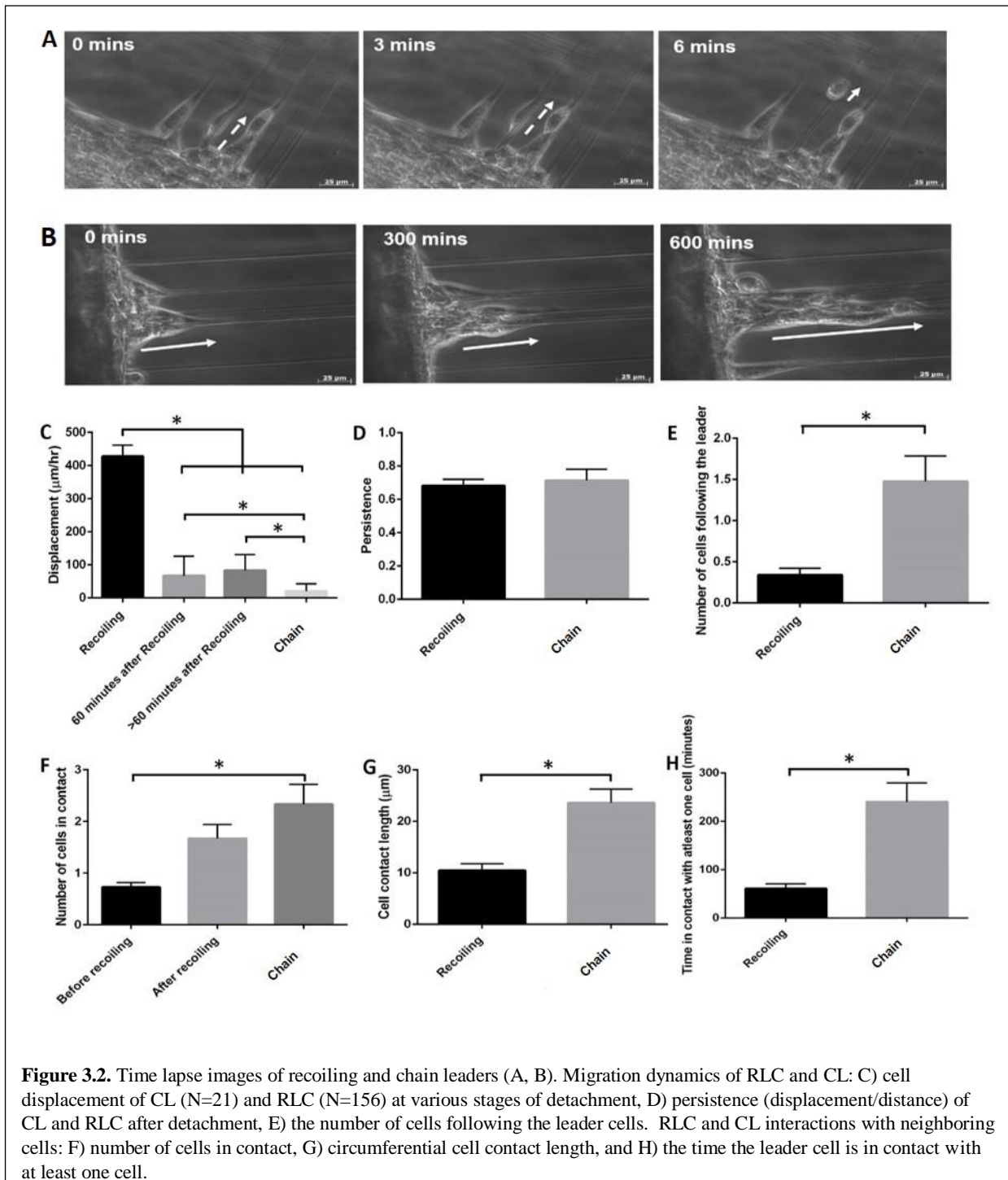
Leader cells were defined as pioneers of collective fibroblast migration on the suspended nanofibers. These cells initiated migration by first extending protrusions on nanofibers, extending their cell body away from the monolayer, and eventually detaching themselves from the monolayer in peculiarly high speeds. Also, leader cells that maintained cell-cell contacts with their follower cells and pulled them away from the monolayer were observed. Hence, we defined two distinct types of leader cells: 'recoiling' leader cells (RLC) which detach from the monolayers at high speeds, and 'chain' leaders (CL) that tug onto their followers and pull them

away from the monolayer towards the nanofiber networks (Fig. 3.1). We then compared and contrasted their migration dynamics, interaction with neighboring cells, cellular morphology, and the dynamics of cells that followed the leaders, or follower cells.

Influence of fiber spacing on leader cell formation: Cells were coming off of the monolayer as either recoiling leaders which stretched along the nanofiber and shot out of the monolayer, or as chain leaders that maintained their cell-cell adhesions with their follower cells and dragged a stream of cells along the fibers. We observed that the fiber spacing played a crucial role in determining the formation of these types of leader (Fig. 3.1). In particular, we observed that recoiling leaders were not as common when the fiber spacing was less than 10 μm (Fig. 3.1C). Once the fiber spacing increased beyond 10 μm , the occurrence of recoiling leaders increased significantly. This behavior was consistent with the three sets of fiber diameters tested. Formation of chain leaders on a single fiber also exhibited a similar pattern (Fig. 3.1A). Specifically, very few chain leaders on a single fiber was observed when the spacing between the fibers were less than 20 μm . However, once the spacing increased beyond this threshold, chain leaders on a single fiber was observed irrespective of the fiber diameter. Chain leaders on double fibers were strictly dependent on the spacing of the fibers (Fig. 3.1B). In particular, almost all the chain leaders observed on double fibers occurred when the spacing between the



fibers were less than $30\mu\text{m}$. This was true for all the fiber diameters tested. In particular, no chain leaders on double fibers were observed when fiber spacing increased beyond $17\mu\text{m}$ for fibers of diameter 200nm , $27\mu\text{m}$ for fibers of diameter 500nm , and $29\mu\text{m}$ for fibers of 1000nm . In essence, these results give rise to a design space for the generation of specific type of leader cells. In order to facilitate the formation of chain cells on double fibers, fiber spacing should

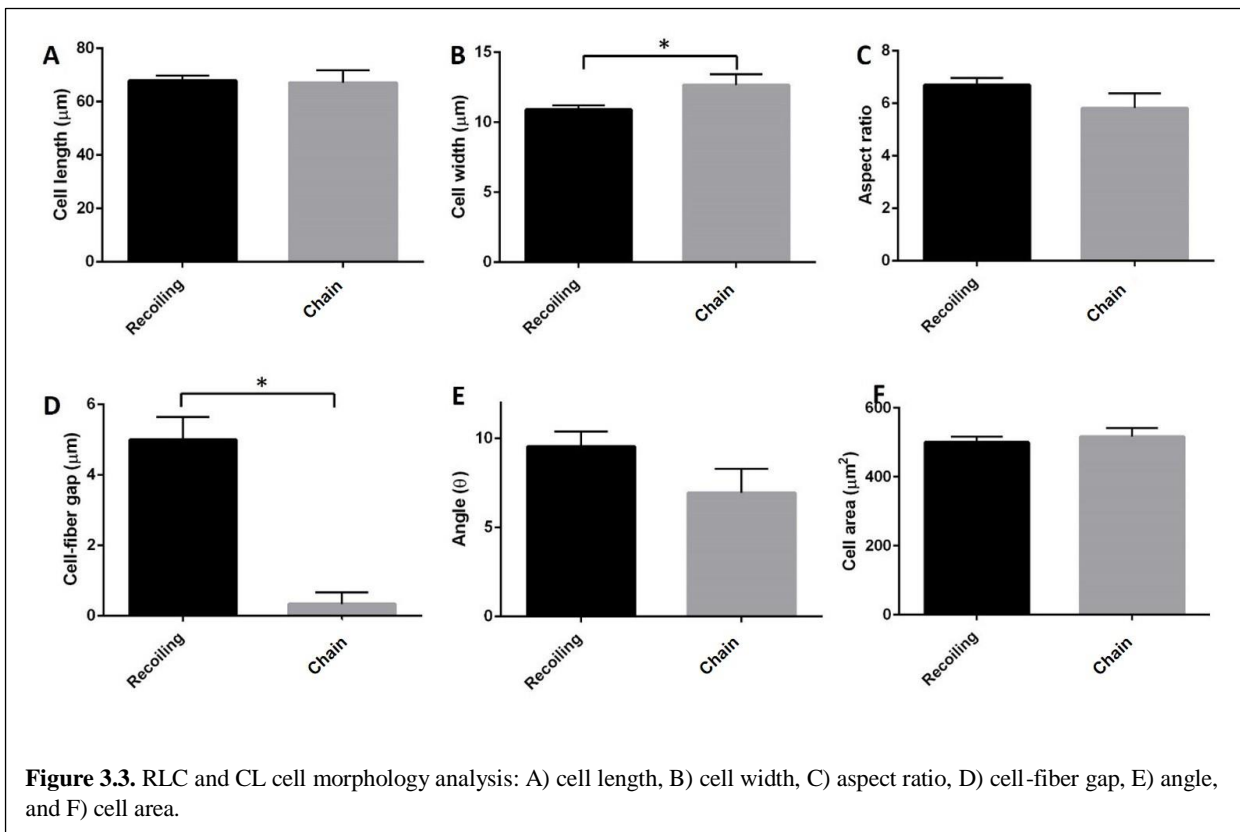


be less than $30\mu\text{m}$ (for fibers of diameter greater than 500nm) and $20\mu\text{m}$ (for fibers of diameter less than 500nm). Similarly, in order to facilitate the formation of recoiling cells or chain cells on single fibers, fiber spacing should be more than $30\mu\text{m}$ (for fibers of diameter greater than 500nm), and $20\mu\text{m}$ (for fibers of diameter less than 500nm). This behavior could be explained by the ability of cells to span the distance between the fibers. Fibroblasts for instance have diameters of about $20\mu\text{m}$, hence they would be able to spread between fibers of similar spacing. In accordance to this, our results indicate that chain leaders occur more on double fibers when the spacing between the fibers is around the diameter of a fibroblast cell. It is however noteworthy that increasing the fiber diameter increases this threshold to $30\mu\text{m}$. It would thus be suggested that increasing fiber diameter also encourages cells to span longer distances.

Migration dynamics: While RLC are characterized by their ability to detach at abnormally high speeds from the monolayers, CL migrated at significantly lower speeds. The detachment dynamics of RLC is further characterized in the following section. Briefly, a recoiling detachment of leader cells from the monolayer base was preceded by cellular protrusions and declining cell-cell contacts. As they continued migrating onto the fibers away from the monolayer, their speeds were not as high. Hence, we measured the displacements of RLC during detachment from the monolayer ($N=70$), in the next 1 hour after detachment if the cell was in frame ($N=56$), and the remaining time the cell was in frame ($N=56$) in order to assess the migratory dynamics of RLC during varying stages of detachment. We then compared these with the displacement of CL ($N=21$). Since the data were not all normally distributed (D'Agostino & Pearson omnibus K_2 normality test; p-values: RLC during detachment: $p < 0.001$; RLC 1 hour after detachment: $p < 0.0001$; RLC >1 hour after detachment: $p = 0.12$; NRCL: $p = 0.002$), a non-parametric Kruskal-Wallis test determined that the magnitude of displacement were statistically significant ($p < 0.0001$). The recoiling speed of the RLC was significantly (almost 4 times) higher than those for CL, its own displacement in the next hour and the

remaining time the cell was in frame (Fig. 3.2C). It was however interesting to note that RLC still had significantly higher displacements than CL 1 hour after detachment and >1 hour after detachment (Dunn's multiple comparison test). This result suggests a superior migratory ability of RLC to CL regardless of its detachment stage from the monolayer.

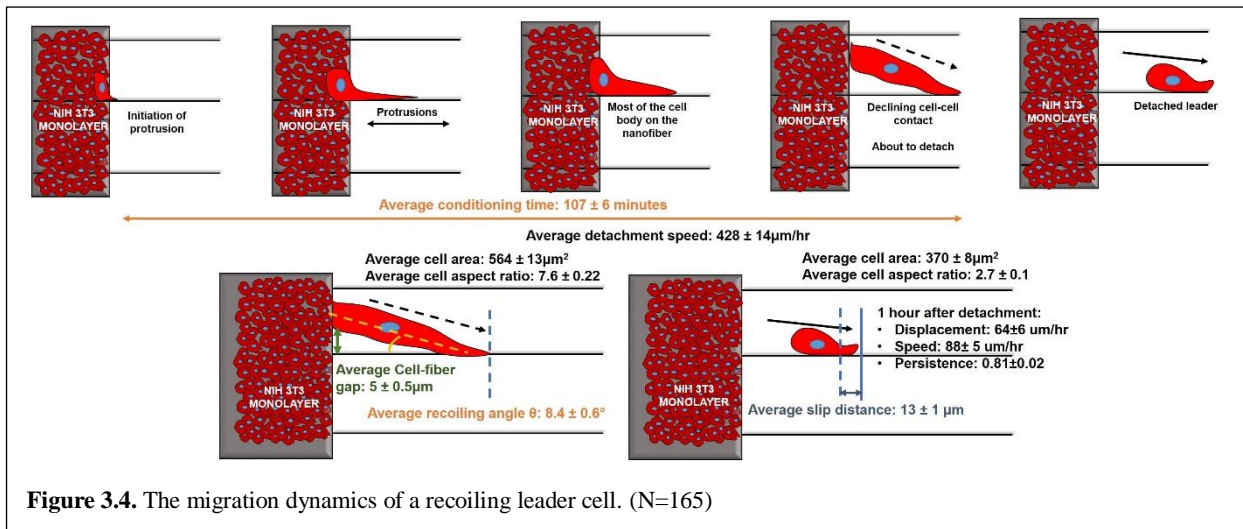
In addition to its displacement, we also measured directional persistence (displacement/distance traveled) of the RLC >1hour after detachment (N=74) and CL (N=21) and found no significant difference between the two (Fig. 3.2D, D' Agostino & Pearson omnibus K2 normality test; p-values: RLC persistence >1 hour after detachment: $p = 0.0015$; CL: $p = 0.26$, and Mann-Whitney test, $p = 0.64$). Similarly, displacement of 15% of RLC >1hour after detachment and 14% of CL were towards the monolayer. On average, RLC were observed for 104 ± 13 minutes after detachment and the CL were observed for 301 ± 35 minutes.



The results obtained from observing the migration dynamics of leader cells indicate that in addition to cell body detachment of RLC at abnormally high speeds, the magnitudes of their displacement is still significantly higher than those of CL. However, once detached, the two distinct leader cell types had comparable persistence, with about 85% of the cells migrating away from the monolayer.

Interaction with neighboring cells: Interaction of the leader cells with their neighbors was assessed by counting the number of cells they had contacts with, the circumferential length of their contact, and the time they remained in contact with at least one cell other than the monolayer. The CL demonstrated superior interaction with its neighboring cells compared to RLC measured by these metrics. On average, the RLC had contact with less than one cell before detaching from the monolayer which was significantly less than the contacts made by CL (Fig. 3.2F). Once detached, RLC interacted with more cells, but the change was not statistically significant. After detachment of the RLC, the number of cells in contact was comparable to those of CL (D' Agostino & Pearson omnibus K2 normality test; p-values: RLC before detachment: $p=0.05$, RLC after detachment: $p < 0.0001$, NRLC: $p= 0.62$, Krushkal-Wallis test: $p = 0.0005$, Dunn's multiple comparison test for analysis among the groups). Similarly, CL had significantly more circumferential contact length with the neighboring cells than the RLC (Fig. 3.2G, D' Agostino & Pearson omnibus K2 normality test; p-values: RLC before detachment: $p < 0.0001$, CL: $p= 0.005$, Mann-Whitney test: $p < 0.0001$). Also, the CL spent significantly more time being in contact with the neighboring cells than the RLC (Fig. 3.2H, D' Agostino & Pearson omnibus K2 normality test; p-values: RLC after detachment: $p=0.0002$, CL: $p= 0.28$, Mann-Whitney test: $p < 0.0001$).

These results suggest that CL primarily like to associate themselves with neighboring and follower cells and potentially influence their migration towards the nanofibers by maintaining



significant cell-cell contact. The RLC on the other hand, are speed oriented wandering cells that do not like to associate with neighboring and follower cells.

Influence on follower cells: The influence a leader has on its follower cells is an important characterization of a leader cell. We assessed this influence by counting the number of cells that followed the leader and the instances where a densely packed steam of follower cells extended from the monolayer and followed the leader. Owing to the higher influence CL had on its neighboring cells, it was not surprising to observe that CL had significantly more number of follower cells (Fig. 3.2C, D' Agostino & Pearson omnibus K2 normality test; p-values: RLC: $p < 0.0001$, CL: $p = 0.1811$, Mann-Whitney test, $p < 0.0001$).

In addition to their influence on neighboring cells, the results show that CL have a more significant ability to bring other cells along their migratory routes although their migration speeds may be lower than those for RLC.

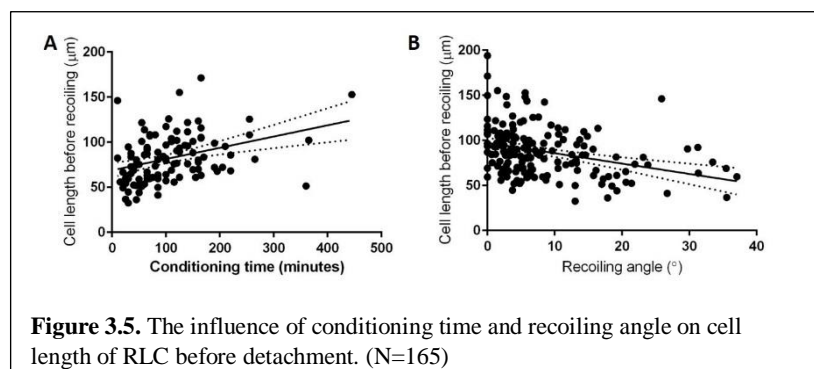
Cell morphology: RLC were mostly inclined at an angle with a measurable gap (in 59% of the cells) between the cell and the nanofiber before detachment. The CL on the other hand, formed triangular structures, but did not have a significant cell-fiber gap when migrating out of the monolayer (Fig. 3.3D, D' Agostino & Pearson omnibus K2 normality test; p-values: RLC: $p = 0.02$, CL: $p < 0.001$, Mann-Whitney test, $p < 0.0001$). The measured angle of the cells before

detachment, however, were not statistically different (Fig. 3.3E, D' Agostino & Pearson omnibus K2 normality test; p-values: RLC: $p=0.0003$, CL: $p=0.43$, Mann-Whitney test, $p=0.2$). Similarly, cell length (Fig. 3.3A, D' Agostino & Pearson omnibus K2 normality test; p-values: RLC: $p=0.002$, CL: $p=0.42$, Mann-Whitney test, $p=0.88$), area (Fig. 3.3F, D' Agostino & Pearson omnibus K2 normality test; p-values: RLC: $p=0.05$, CL: $p=0.75$, Mann-Whitney test, $p=0.5$), and aspect ratio (Fig. 3.3C, D' Agostino & Pearson omnibus K2 normality test; p-values: RLC: $p=0.09$, CL: $p=0.29$, Student's t-test, $p=0.14$) of RLC and CL were comparable to each other. But, the RLC had a significantly smaller cell width compared to the CL (Fig. 3.3B, D' Agostino & Pearson omnibus K2 normality test; p-values: RLC: $p<0.0001$, CL: $p=0.03$, Mann-Whitney test, $p=0.05$).

Despite the pronounced cell-fiber gap observed in RLC, cellular morphology of these types of cells were similar to each other. We then asked if the cell-fiber gap could be contributing to the increased detachment speed of RLC. In other words, is there a morphological signature of the RLC that triggers their detachment from the monolayer? In order to address this concern, we further investigated the detachment dynamics and cell morphology of RLC during detachment.

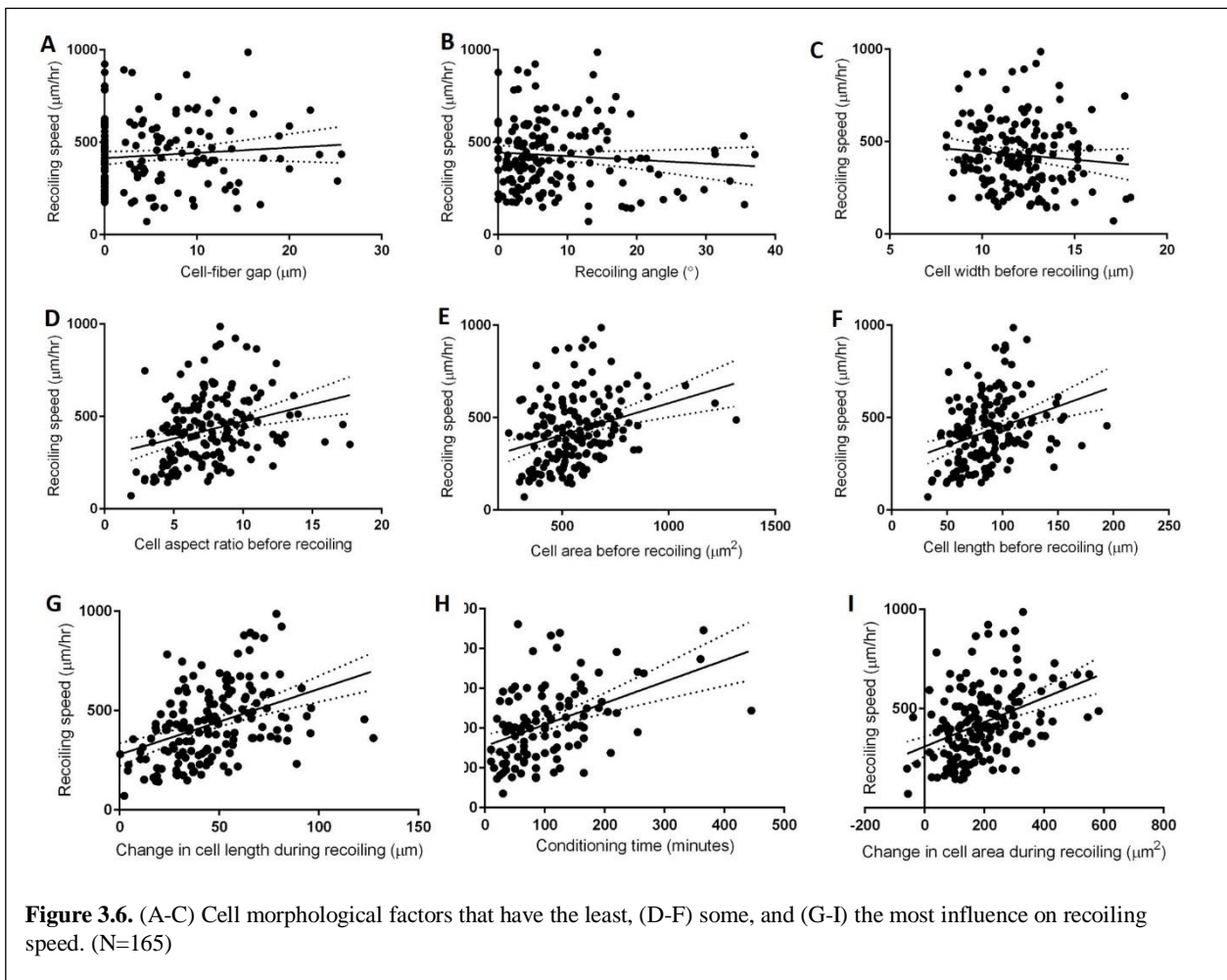
Migration dynamics of a Recoiling leader: Detachment of fibroblast cell bodies from the monolayer at peculiarly high speeds of more than $400\mu\text{m/hr}$ (Fig. 3.4) to the best of our knowledge, has not been reported before. We then asked whether morphological, cytoskeletal or the influence of the environment would trigger the detachments of fibroblast at such significant speeds away from the monolayer. Knowledge of triggering factors could not only

improve the design of tissue engineering scaffolds for faster healing of chronic wounds, but could also potentially highlight the

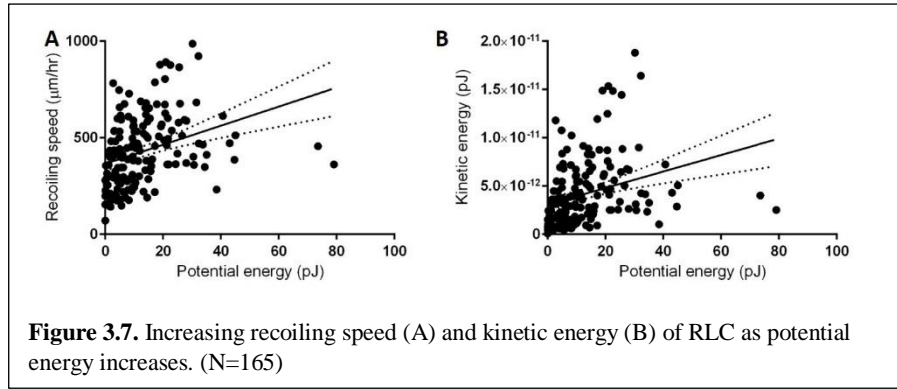


detachment and migration triggering conditions for diseases like cancer ¹⁰⁷. Therefore, we investigated the leader cell morphology, the influence of acto-myosin interaction compromising drug γ -27632 ^{13,108}, and the influence of changing fiber diameters on detachment dynamics of recoiling leaders (N=165).

Influence of cell morphology: Recoiling leaders extended their protrusions on a nanofiber from the monolayer. After repeated protrusion extensions and retractions, they extended their bodies in a triangular shape away from the monolayer. The triangular shape of the cell was quantified by an average cell recoiling angle of $8.4 \pm 0.6^\circ$ before detachment. Interestingly, RLC length and recoiling angle were inversely related with longer cells forming lower recoiling angles and vice versa (Fig. 3.5B, $R^2 = 0.11$). Before detachment, a measurable gap between the cell and



the fiber (averaging $5 \pm 0.5 \mu\text{m}$) was often observed. This was followed by declining cell-monolayer contacts and a sudden



high speed detachment of the leader cell (averaging $428 \pm 14 \mu\text{m/hr}$) from the monolayer. The time taken (conditioning time) by a leader cell to first appear on the nanofiber to detachment from the monolayer was 107 ± 6 minutes on average. Longer conditioning times were correlated with longer leader cell length before detachment (Fig. 3.5A, $R^2 = 0.13$). The leader cells exhibited elongated cell morphology (average aspect ratio of 7.6 ± 0.22) before detachment, and formed a bulb/teardrop like morphology (average aspect ratio of 2.7 ± 0.1) after detachment from the monolayer. The teardrop shape of the detached leader indicates that the rear side of the cell detached from the monolayer and recoiled¹⁰⁹, while the front still remained adhered to the nanofiber. This was further demonstrated by relatively small distance covered by the front of the leader cell during detachment, called the slip distance (average $13 \pm 1 \mu\text{m}$). After detachment, the transition from a teardrop to a more common spindle morphology of the leader cells took about 18 ± 2 minutes. Interestingly, RLC detaching at higher recoiling speeds had lower slip distances although the correlation was very low ($R^2 = 0.03$). After detachment from the monolayer, the RLC mostly migrated away from the monolayer. An average displacement and speed of the RLC after detachment were 64 ± 6 and $88 \pm 5 \mu\text{m/hr}$ respectively, with a persistence of 0.81 ± 0.02 away from the monolayer. We further analyzed the degrees of impact of these cell morphology characteristics on the recoiling speed of the RLC.

Cell-fiber gap, recoiling angle and cell width before detachment had the least correlation with detachment speed of the RLC (Fig. 3.6 (A-C), R^2 values of 0.009, 0.008, and 0.01 respectively). On the other hand, factors like cell aspect ratio, area and length before detachment had some influence on recoiling speed of RLC (Fig. 3.6 (D-F), R^2 values of 0.08, 0.1, and 0.1 respectively). Finally, conditioning time, change in cell length and area during recoiling had the highest influence on detachment speed of RLC (Fig. 3.6 (G-I), R^2 values of 0.19, 0.15, and 0.15).

Overall, the data obtained from observing detachment dynamics of RLC suggest that these cells behave like simple linear elastic springs that are essentially at a tug of war between being attached to the monolayer on one side, and trying to migrate away from the monolayer using the fibers as a highway^{110,111}. As they take time extending their cell bodies away from the monolayer, they are essentially increasing their elastic potential energy which is acquired by virtue of increasing cell length. Upon successful decline of cell-monolayer contacts, this potential energy is used to propel the rear part of the cell forward at recoiling speeds exceeding 400 $\mu\text{m/hr}$. This phenomenon can be deduced by observing the positive correlation of increasing potential energy of the cells with higher recoiling speeds, and eventually kinetic energy (Fig. 3.7, R^2 values of 0.11 and 0.1 respectively). The change in cell area, length and conditioning time are therefore most crucial in facilitating the recoiling of RLC at such high speeds. Factors like cell-fiber gap, recoiling angle and cell width on the other hand, did not seem to play a critical role in facilitating high speed recoiling of leader cells. It is also interesting to observe that the front of the cell migrated only about 13 μm during the recoiling episode. Although these cells are recoiling at exceptionally high speeds, the front of the cell does not migrate as much.

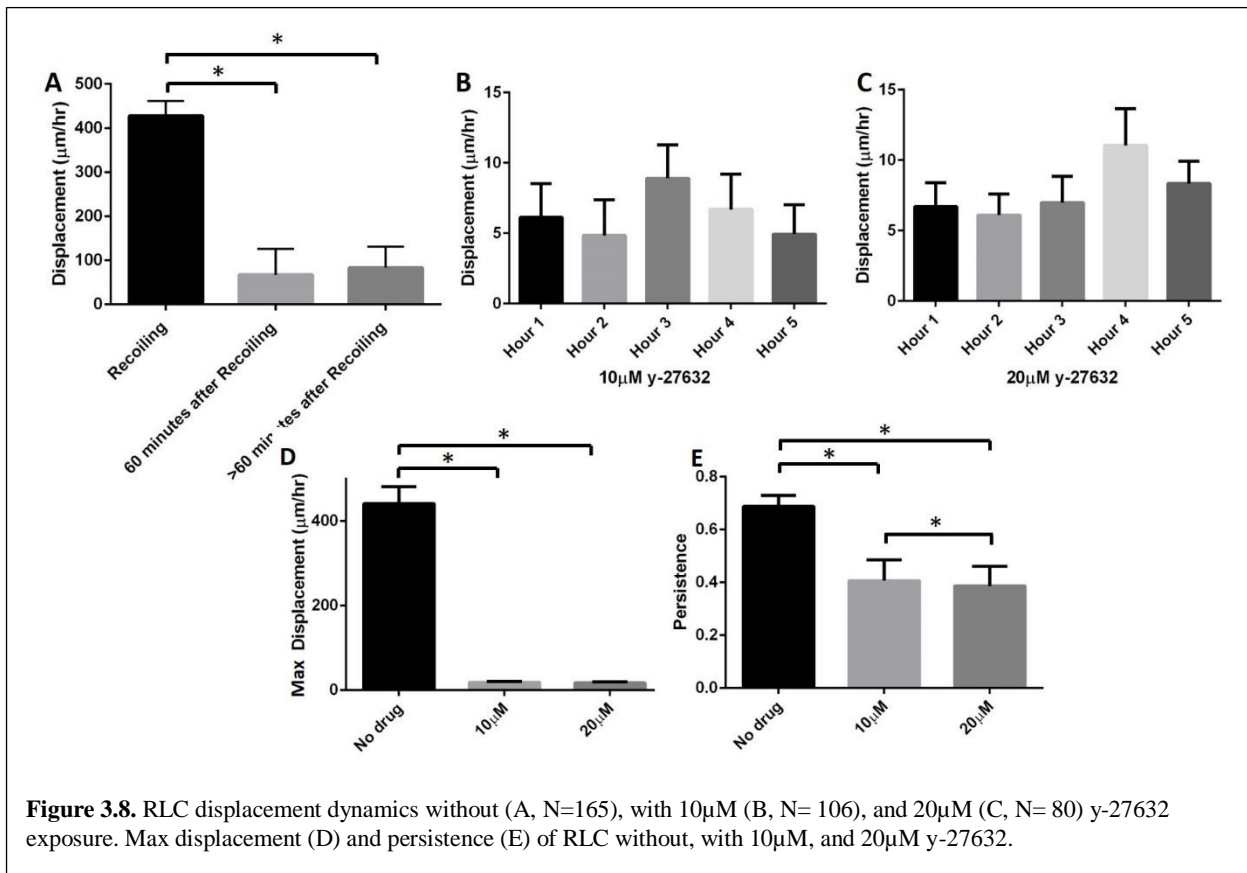


Figure 3.8. RLC displacement dynamics without (A, N=165), with 10 μM (B, N= 106), and 20 μM (C, N= 80) y-27632 exposure. Max displacement (D) and persistence (E) of RLC without, with 10 μM , and 20 μM y-27632.

Migration of the leader cells after detachment however, did not seem to be influenced by the recoiling episode. In other words, leader cells that exhibited high recoiling speeds, did not necessarily migrate faster after detaching from the monolayer. In particular, the displacement of the leader cells an hour after recoiling was very weakly related with cell length before recoiling and the recoiling speed.

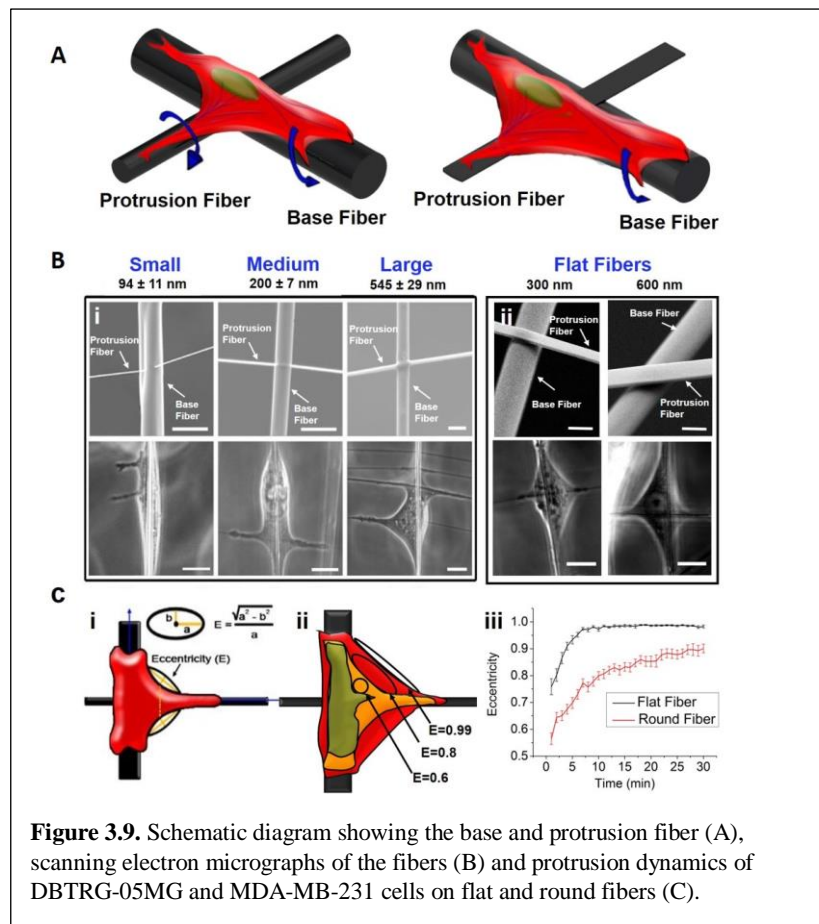
Influence of acto-myosin contractility: In the last few decades, studies have attributed the retraction of cell rear mostly to actin-myosin II interactions^{112,113}. Hence, we asked the question if the recoiling of leader cells can be compromised by inhibiting actin-myosin interactions. We measured the displacement of RLC (N=70, also shown in Fig. 3.2C) during recoiling, 1 hour after recoiling, and >1 hour after recoiling. Similarly, the displacements of leader cells when exposed to 10 μM (N=106), and 20 μM (N=80) ROCK inhibitor y-27632 were investigated¹¹⁴. Average maximum displacements for the cells exposed to y-27632 were significantly lower than those not exposed to the drug (Fig. 3.8 (A-C), D' Agostino & Pearson

omnibus K2 normality test; p-values: Without drug: $p < 0.0001$, y-27632 10 μ M: $p = 0.4413$, 20 μ M: $p < 0.0001$, Krushkal-Wallis test: $p < 0.0001$). Furthermore, while the leader cells exhibited peculiarly high recoiling speeds, and showed a significant decrease to speeds slightly less than 100 μ m/hr after recoiling, cells under the influence of the drug migrated at consistent, and significantly lower speeds of about 5-15 μ m/hr (Fig. 3.8 (A-C)). In particular, the leader cell displacements when exposed to both 10 μ M (Fig. 3.8B, D' Agostino & Pearson omnibus K2 normality test; p-values: Hour 1: $p < 0.0001$, Hour 2: $p < 0.0001$, Hour 3: $p = 0.3$, Hour 4: $p = 0.06$, Hour 5: $p = 0.05$, Krushkal-Wallis test: $p = 0.77$) and 20 μ M (Fig. 3.8C, D' Agostino & Pearson omnibus K2 normality test; p-values: Hour 1: $p < 0.0001$, Hour 2: $p = 0.18$, Hour 3: $p < 0.0001$, Hour 4: $p < 0.0001$, Hour 5: $p < 0.0001$, Krushkal-Wallis test: $p = 0.83$) y-27632 were not statistically different between the 5 hours of observation. Their ability to recoil was significantly compromised as shown by the relatively steady and slow displacements between 5 consecutive hours of observation. Unlike the RLC that were not exposed to y-27632, Only 5% and 2.5% of the leader cells exposed to 10 and 20 μ M y-27632 respectively were able to recoil and detach from the monolayer. Cells exposed to y-27632 were also less persistent in the direction away from the monolayer (Fig. 3.8 (D-E), D' Agostino & Pearson omnibus K2 normality test; p-values: Without drug: $p < 0.0001$, y-27632 10 μ M: $p < 0.0001$, 20 μ M: $p = 0.03$, Krushkal-Wallis test: $p < 0.0001$).

These results strongly reinforce that actin-myosin contractility is one of the most important driving forces for detachment and recoiling of RLC. Compromised actin-myosin interactions not only minimized cell migration speeds, it significantly reduced the occurrence of RLC detachment from the monolayer.

Role of substrate topography and vimentin in cellular protrusions: Change in cytoskeletal proteins is one of the major occurrence during leader cell formation²⁷. Leader cells extend cellular protrusion in their native environment as precursors of migration. Vimentin was first

associated with migrating cells in 1983^{115,116}. Since then, vimentin has been shown to be critical in EMT, wound closure and cancer metastasis. Interestingly, lack of vimentin did not impede embryogenesis in mice suggesting that the role of vimentin may only be important in an adult organism and not during embryonic development¹¹⁵.



Their role has also been implicated in protrusive structures called invadopodia that cancer cells utilize in order to puncture the basement membrane and metastasize to the surrounding tissue. Specifically, it was noted that vimentin was required for the elongation, not the formation of invadopodia¹¹⁷. In another study investigating the role of leader cells however, vimentin was not shown to be a critical component of the leader cell⁸⁹. These conflicting results show that the role of vimentin in leader cell migration and protrusion is not well understood. Here, we have isolated the investigation of cell protrusion from cell migration by using fibers of different diameters. Specifically, glioma and breast cancer cells were seeded on criss cross fibers of a micron size fiber (base fiber) and a smaller diameter (protrusion fiber) (Fig. 3.9A). The presence of a relatively large diameter base fiber limited the migration of the cells to the base fiber allowing us to solely investigate the influence of fiber properties on protrusions extended by DBTRG-05MG glioma and MDA-MB-231 breast cancer cells. In order to investigate the

role of curvature in protrusion extension, circular fibers (fabricated by Brian Koons), and flat fibers (fabricated by Zhou Ye) were used (Fig. 3.9B). In order to capture the shape of the protrusion, an eccentricity parameter was introduced (Fig. 3.9C). It was observed that glioma and breast cancer cells extended triangular protrusions (with more eccentricity) quickly on flat fibers when compared to protrusion dynamics in circular fibers where protrusions were mostly rod like and slowly extended to triangular protrusions. These results indicate that the shape of the protrusion could be time and substrate dependent as cells were fanning out much quickly in fibers of flat dimensions.

We further investigated the role of vimentin in a protrusion through live vimentin imaging and shVim DBTRG-05MG and MDA-MB-231 cells on regular cylindrical fibers. We observed the following chain of events during a protrusion: first, cells send out rod like protrusive structures that are less than 10 μm in length, then these protrusive structures start fanning out as the length of the protrusion increased, then vimentin enters the protrusion when the length of the protrusion is about 15 μm and its eccentricity is almost 0.8 (triangular shaped protrusions), then vimentin extensions and retractions essentially shadows the extension and retractions of the

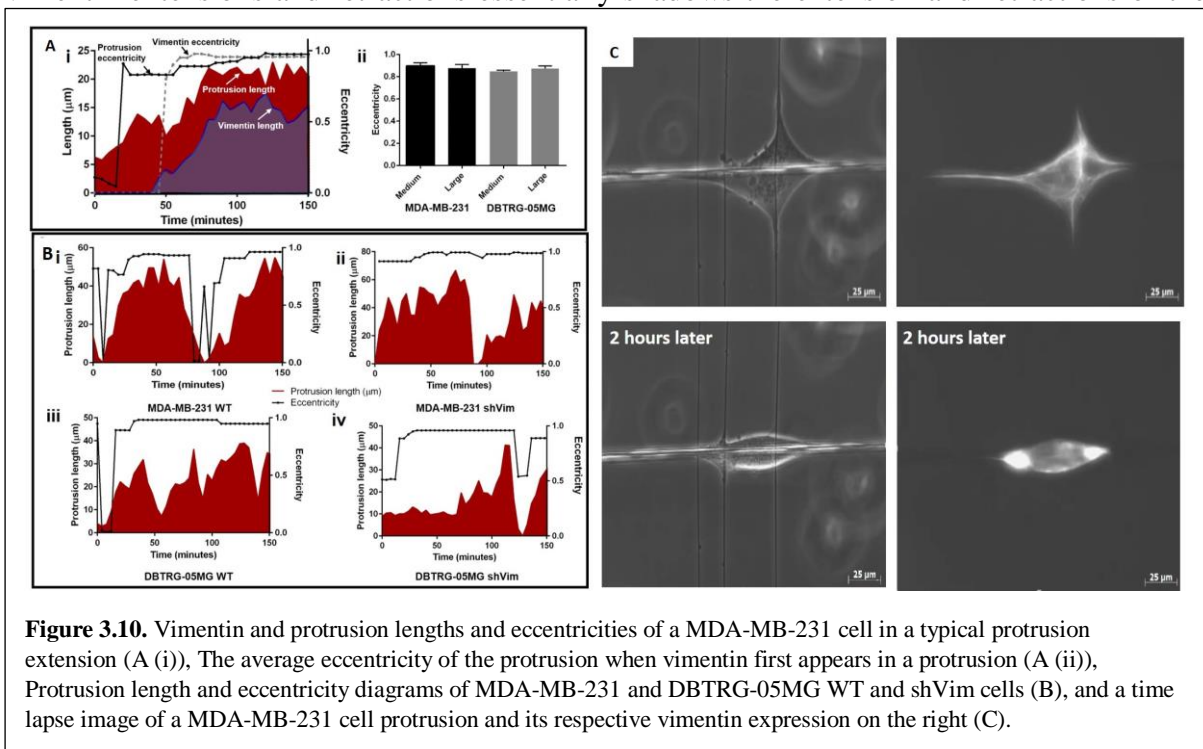
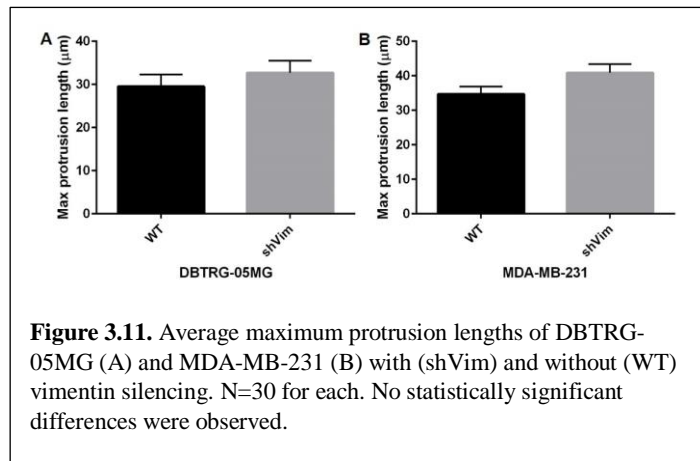
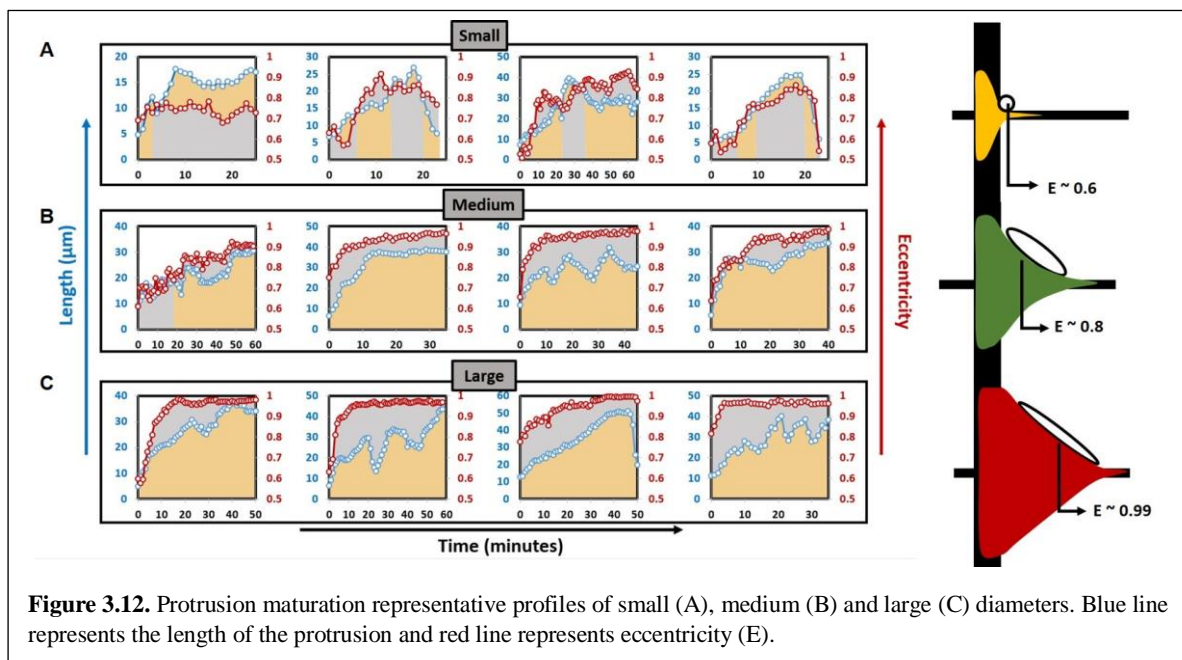


Figure 3.10. Vimentin and protrusion lengths and eccentricities of a MDA-MB-231 cell in a typical protrusion extension (A (i)), The average eccentricity of the protrusion when vimentin first appears in a protrusion (A (ii)), Protrusion length and eccentricity diagrams of MDA-MB-231 and DBTRG-05MG WT and shVim cells (B), and a time lapse image of a MDA-MB-231 cell protrusion and its respective vimentin expression on the right (C).

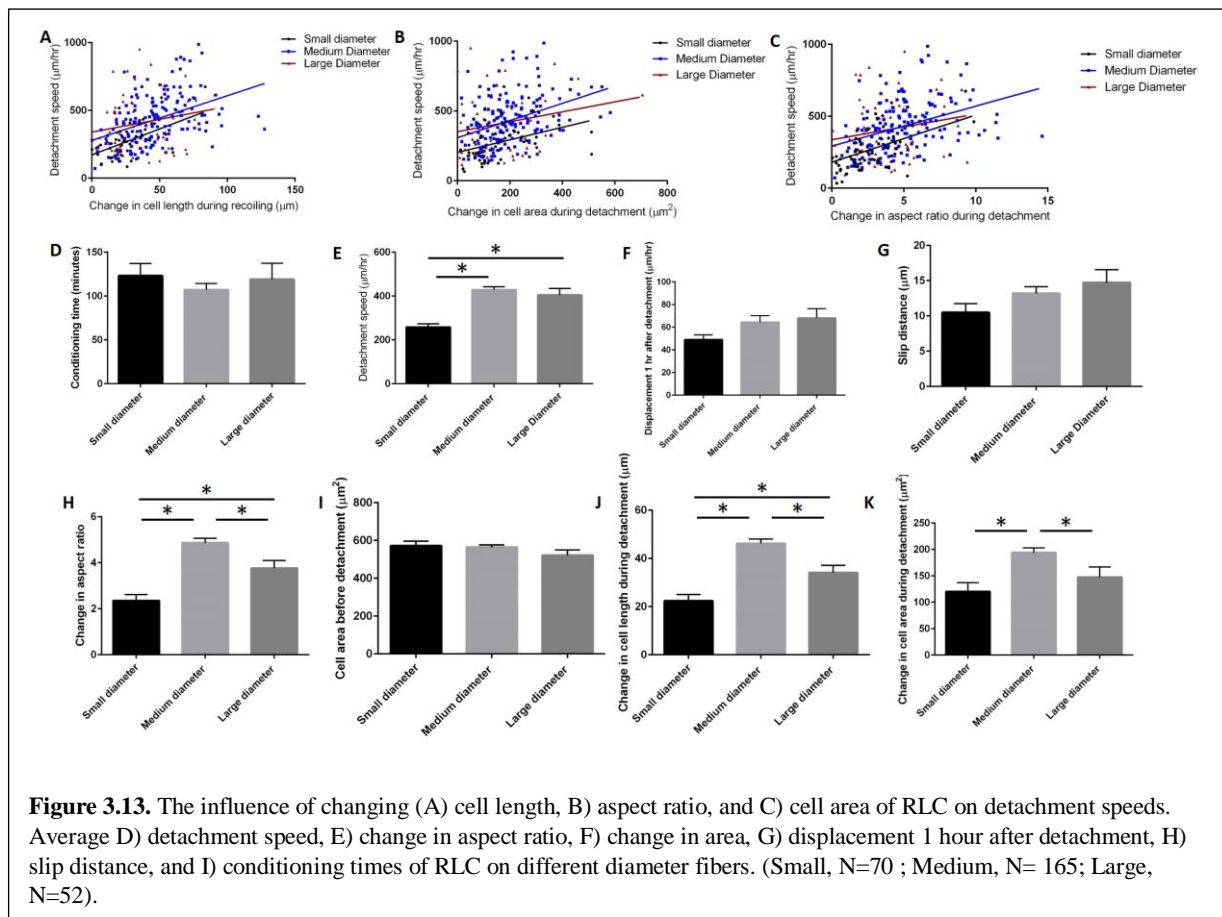
protrusion (Fig. 3.10A). Interestingly, when vimentin was silenced in DBTRG-05MG and MDA-MB-231 cells, cells were still able to protrude onto the protrusion fibers. The lengths of these vimentin deprived protrusions were almost as high as those with



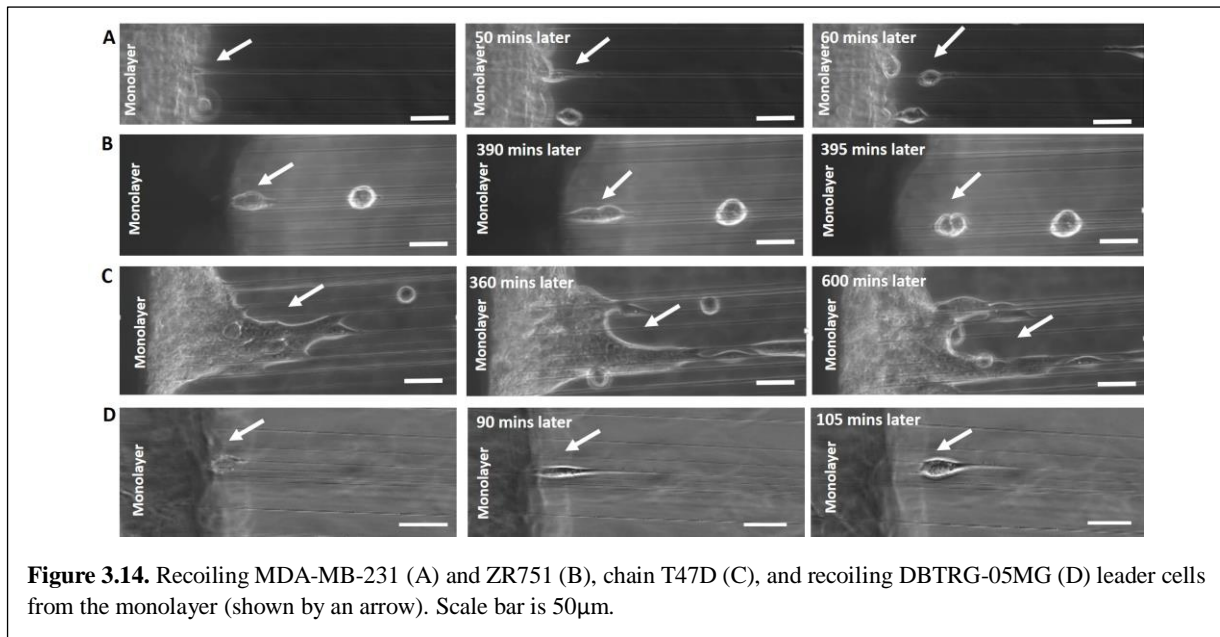
vimentin (Fig. 3.10B). A representative time lapse video image of the live vimentin is shown in Fig. 3.10C. Our results suggest that although vimentin appears in well-developed protrusions that are longer than 15μm and triangular, glioma and breast cancer cells are still able to extend long mature protrusions without the presence of vimentin in the cell. Figure 3.11 illustrates the maximum protrusion length with and without vimentin silencing for glioma (DBTRG-05MG) and breast (MDA-MB-231) cells. On average, maximum protrusion lengths for cells were 30-40μm regardless of the presence or absence of vimentin, and there was no statistically significant differences between protrusion lengths with and without vimentin. This result while is contrary to the fact that vimentin is an important EMT marker¹⁰³, it is consistent with the observation by Cheung et al that demonstrates that vimentin may not be necessary during leader cell formation⁸⁹. Given the presence of other cytoskeletal proteins like cyokeratin and microtubules, it could be such that the cells effectively compensate the absence of vimentin with other cytoskeletal proteins. Hence, in future, serial knockouts of each and a combination of cytoskeletal proteins could help us determine the role of each protein and the ability of the cell to compensate their absence.



Influence of fiber diameter: Mechanical properties of the ECM have been well known to instigate changes in cytoskeletal and focal adhesion proteins. In particular, studies have shown that the stiffness of the environment can contribute to recruitment of actin and enhance the traction forces exerted by cells^{24,118}. Using polystyrene fibers of varying diameters allows us to probe the influence of structural stiffness and curvature on detachment dynamics of leader cells. The results obtained can not only help in the design of fibrous scaffolds that better facilitate the detachment of leader cells to help close wounds faster, but also aid in a better understanding of cancer metastasis in tumor associated collagen signatures (TACS) than comprise of highly aligned collagen bundles of varying diameters^{42,44}. Here, we investigated the influence of small (~300nm), medium (~500nm) and large (~1μm) diameter fibers on the detachment dynamics of leader cells. We observed that cancer cells (DBTRG-05MG and MDA-MB-231) extended rod like protrusions with lower eccentricities on small diameter fibers (Fig. 3.12A), triangular protrusions with slightly higher eccentricities on medium diameter (Fig. 3.12B), and triangular protrusions with very high eccentricities in a shorter time interval on large diameter (Fig. 3.12C) fibers. In addition to protrusion dynamics, the fiber diameters also influenced the detachment dynamics of leader cells.



Similar to our previous observations, the cells exhibited higher detachment speeds when changes in cell length, aspect ratio and areas were higher. Hence, regardless of the size of the diameter tested, the cells still showed an almost elastic behavior where the energy stored by virtue of their length was converted into detachment speed of the leader cells. However, for the same change in cell length and aspect ratio, leader cells detached faster when on large diameter fibers (Fig. 3.13 A-C). On average, the detachment speed was significantly higher for leader cells on large diameter fibers (Fig. 3.13E). Also, the average slip distance of leader cells on large diameter was higher than on small diameter fibers (Fig. 3.13G). While changes in aspect ratio, cell area and length during detachment was significantly higher for leader cells (Fig. 3.13H, J and K) on medium diameter fibers, the conditioning time, cell area before detachment, and displacement 1 hour after detachment did not vary significantly among the fibers diameters (Fig. 3.13D, I and F).



Similar to the observation of higher traction forces exerted by cells on stiffer substrates¹¹⁹, our results show that leader cells on large diameter fibers could be acting as a spring with a higher spring constant than those on small diameter fibers. Hence, for the same change in cell length, they exhibit higher potential energy, ultimately increasing the detachment speed of the leaders despite comparable conditioning times during leader cell formation. However, once the cells detach from the monolayer, their displacement in the immediate hour following detachment were comparable to each other. The results suggest that ECM fiber diameter can potentially dictate the detachment behavior of leaders with large diameters ($\sim 1\mu\text{m}$) facilitating increased leader cell speed and detachment occurrence.

Leader cell behavior in cancer cells using the STEP platform: Understanding the protrusion and emergence behavior of leader cells is not just important for wound healing models. Using the same platform cancer cells including MDA-MB-231, DBTRG-05MG, T47D, and ZR751 (Fig. 3.14) have also been observed to emerge as recoiling leaders. The recoiling and chain behavior of these cells can be investigated in future in order to better understand how the cell environment influences its ability to come out as leaders.

3.4 Conclusion

Investigating leader cell migration dynamics on monolayer-fiber interface demonstrated that the leader cells can be categorized into distinct recoiling leaders which migrate in sling shot fashion and chain leaders which pull a series of follower cells along. We have shown that fiber spacing dictates the ability of the cells to come out as recoiling or chain leaders. Also, the results show that the leader cells spend about 2 hours protruding and investigating its surrounding before it recoils onto a fiber away from the monolayer. Recoiling dynamics of leader cells showed that changes in cell length and area and the conditioning time were the most influential factors that directly increased the recoiling speed of leader cells. This suggests that the leader cells are acting as spring that store energy by the virtue of their length, and convert that energy into kinetic energy as it is detaching from the monolayer. Furthermore, the severely compromised speed of the leader cells and their inability to recoil and detach from the monolayer upon exposure to 10 and 20 μ M γ -27632 demonstrates that actin-myosin contraction is a major driving force behind the ability of these cells to detach. Also, we observed that fiber curvature influences the ability of leader cells to protrude onto the fibers. Similarly, we observed that cancer cell protrusions while contain vimentin in long and triangular protrusions, the lack of vimentin does not compromise the ability of the cells to form or elongate the protrusions. It was also observed that detachment speed of the leader cells is influenced by the diameter of the fiber. As the diameter of the fiber increases, leader cells are observed to exhibit higher detachment speeds, speed after detachment, and slip distance.

Overall, these results suggest that individual leader cells take time to protrude and explore its fibrous environment. Their protrusion dynamics is dependent on their immediate environment, and depending on the biophysical properties of the fibers, they either migrate out as individuals or pull a collective stream of cells with intact cell-cell adhesions. Also, depending on the biophysical properties of the fibers, their detachment ability and migration changes. Such

findings can be directly applied to metastatic models where breast cancer cells can be interfaced with fibers of varying mechanical properties and the detachment and migration dynamics can be investigated.

Chapter 4:

Spheroid dynamics on STEP nanofibers

4.1 Introduction

Since the introduction of cell culture in the 1950s, cell cultures have been used to test potential drugs in an *in vitro* setting¹²⁰. Later in the 1970s, colony forming assay that allowed the culturing of patient derived material was introduced¹²¹. Today, a variety of *in vitro* platforms including 2D mono and co-cultures, 3D spheroids and matrix embedded 3D cell structures are used to test potential anticancer drugs. Despite rigorous testing of potential anticancer drugs performed in various *in vitro* platforms, about 95% of the anticancer drugs are shown to be ineffective during clinical trials¹²⁰.

Some of the popular mechanisms of 3D spheroid formation include the ‘hanging drop’ method, coating of the underlying well plate with cell adhesion repelling substance like poly-HEMA in order to facilitate the formation of 3D spheroid structures, adding ECM proteins to facilitate the formation of a sphere, bioreactor controlled culture systems including rotary cell culture system, stirred culture vessels and microfluidic devices¹²⁰. These models are sometime categorized into four major categories: tumorspheres, organotypic multicellular spheroids, multicellular tumor spheroids, and tissue derived tumor spheres. They take anywhere from one to a couple of months to form¹²¹.

Moving from traditional 2D cultures to native tissue mimicking 3D cultures in order to test for drugs makes sense as it has been shown that cells behave very differently in these two systems. Because 3D systems more closely resemble the native tumor setting, anticancer drugs that are more effective in these settings could have a higher potential to succeed as an anticancer agent. One of the underlying differences between these systems include the fact that 3D spheroids contain a necrotic core, a middle layer of quiescent cells and an outer proliferating cell layer¹²¹.

Several irregularities including inconsistent distribution of anticancer agents, permeability of nutritional agents, alteration in chromatin structure, oxygen permeability, and drug resistance have been reported¹²². Also, drugs that have been shown to be more effective in 3D systems compared to traditional 2D systems have been observed. Some of these differences could be attributed to how single and inter cell communication differs in a spheroid. For instance, expressions of E-cadherin and stem cell marker CD44 have been shown to be upregulated whereas proteins like integrin $\beta 1$, $\beta 4$ and $\alpha 6$ have been shown to be downregulated in cells in a spheroid^{121,123,124}.

Some of the desired attributes of a 3D spheroid include the ability to culture the spheroids long term, the ability to produce repeatable spheroids of user defined parameters, the lack of spheroid disintegration especially during transfer of the spheroid during handling, the ability to be able to form a large number of spheroid at once, the incorporation of the tumor environment and it's *in vivo* resemblance^{121,122,125,126}.

Here we present a method for the formation of spheroids on STEP nanofibers. Our preliminary studies have shown that spheroid of fibroblast form upon the retraction of cell streams and maintain their shapes for several months. These spheroids could be utilized to investigate fibroblast-cancer cell communication *in vitro* in co-cultures. Also, using similar strategies, tumor spheroids could be engineered and the influence of anticancer agents could be investigated.

4.2 Materials and Methods

Scaffold preparation

Incisions were made into 300 μm thick plastic cover slips (Fischer Scientific, Pittsburgh, PA) to create gaps. Polystyrene (PS, Scientific Polymer Products, Ontario, NY, M_w : 2×10^6 g mol⁻¹) was dissolved in xylene (Fischer Scientific, Pittsburgh, PA) at 7% (w/w) to prepare a

polymeric solution for fiber spinning. After at least 48 hours of solution preparation, the solution was extruded through a micropipette to deposit 500 nm diameter parallel and suspended fibers using the previously described non-electrospinning STEP technique^{86,87,127,128}. These scaffolds were tacked down in glass bottom six-well dishes (MatTek Corp., Ashland, MA) using high vacuum grease (Dow Corning, Midland, MI). The scaffolds were sterilized with ultraviolet rays in a sterile biosafety cabinet (1300 Series A2, Thermo Scientific, Waltham, MA) for twenty minutes before cell seeding.

Cell culture and seeding

NIH 3T3 mouse embryo fibroblasts were obtained from American Type Cell Culture (ATCC). As recommended, these cells were grown with Dulbecco's Modified Eagle's Medium (DMEM, HyClone, Logan, UT) and 10% bovine calf serum (ATCC, Manassas, VA). The cell culture was maintained at 37°C and 5% CO₂. Cells were trypsinized and seeded on STEP nanofibers as explained in previous chapters. Precisely, a concentrated solution of fibroblasts was placed on two adjacent plastic platforms, and the well plates were flooded with 2ml of media with 1% penicillin/streptomycin (HyClone, Logan, UT) after cells attached onto the platforms. The cell culture media was changed 3 times a week after rinsing the substrates with PBS.

Imaging

The scaffolds were imaged using a Zeiss microscope (Zeiss AxioObserver Z1, Jena, Germany) with incubating capacity (maintained at 37°C and 5% CO₂). Time lapse phase contrast images were obtained using to investigate spheroid dynamics on STEP nanofibers.

Data analysis

The time lapse images were Zeiss Axiovision software.

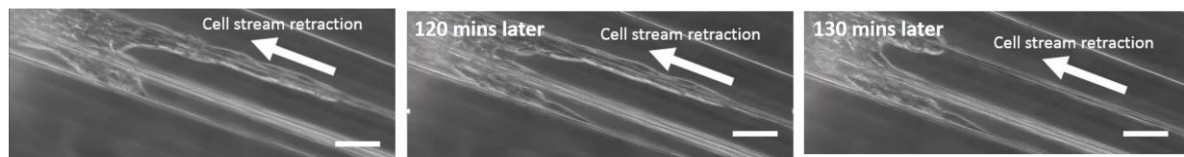


Figure 4.1 Time lapse images showing retraction of a cell stream (shown by arrow). Scale bar is 50μm.

4.3 Results and Discussion

Formation of spheroids: Fibroblast cells sensed the fibers and started migrating onto the fibers. Over several days, the migration of single cells was followed by migration of cell streams where cells were maintaining cell-cell contacts as they progressed onto the fibers from the monolayer. These cell streams increased in density as more cells started coming off of the monolayer. In certain cases, these cell streams retracted (Fig. 4.1), and formed spherical structures that were able to maintain their shape over long periods of time. The average diameter of these spheroids was $72 \pm 5 \mu\text{m}$. However, spheroids with diameters from 20 to $210 \mu\text{m}$ were observed. We were able to culture these spheroids in well plates for approximately nine months.

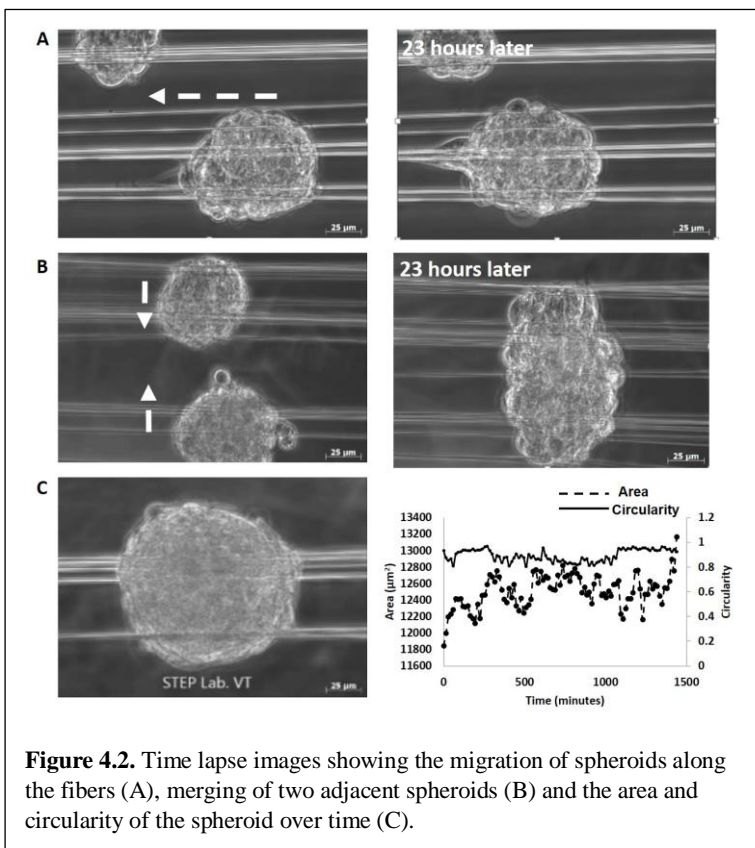


Figure 4.2. Time lapse images showing the migration of spheroids along the fibers (A), merging of two adjacent spheroids (B) and the area and circularity of the spheroid over time (C).

Spheroid behavior: Spheroids were constantly interacting with their immediate environment. Precisely, migration or sliding of the spheroids (Fig. 4.1A), and merging of the spheroids (Fig. 4.1B) was also observed. These spheroids were able to maintain their shape and size over a long period of time. Fig. 4.1C demonstrates the area and

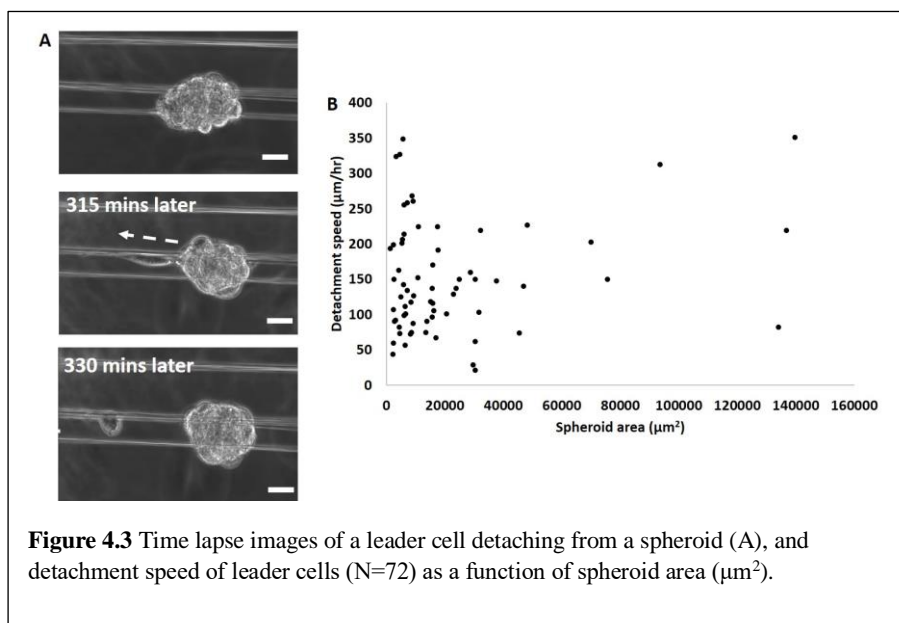


Figure 4.3 Time lapse images of a leader cell detaching from a spheroid (A), and detachment speed of leader cells (N=72) as a function of spheroid area (μm^2).

circularity measures of a spheroid over a 25 hour period. We observe that the area of the spheroid remained relatively constant (from 120,000 to 130,000 μm^2) while

the circularity of the spheroid remained close to 1 the entire time.

Leader cell migration from the spheroids: The cells from the spheroids were constantly probing on the fibers. In several instances, recoiling leader detachment from the spheroid was also observed (Fig. 4.3). We observed that these recoiling leader detached at an average speed of $151 \pm 10 \mu\text{m/hr}$. However, detachment speeds from 21-350 $\mu\text{m/hr}$ were observed. These detachment speeds were observed to be lower than the detachment speed of recoiling leader cells that detached from a 2D monolayer. Hence, we wanted to investigate if the size of the spheroid influenced the detachment speed of the recoiling leader cells. We observed no specific patterns of detachment speed with spheroid area (Fig. 4.3B) suggesting that the magnitude of leader cell recoil could be independent of the size of the spheroid.

4.4 Conclusion

These preliminary results demonstrate a novel method of spheroid generation that has not been presented before. Although the size of the spheroids formed on the STEP fibers (diameters: 20-210 μm) are much smaller compared to those used *in vitro* to screen for potential anticancer agents (diameters: 500 to >1,000 μm)¹²², there could be several advantages of this particular

method of spheroid generation. For instance, these spheroids are already embedded onto an array of nanofibers which could allow investigations of leader cell detachment and the influence of various drugs on leader cell detachment from the spheroids. Similarly, use of fibroblast spheroids have been deemed important in a phenomenon called necrosis where fibroblast clusters have been reported to enhance invasiveness of tumors¹²⁹. Hence, these spheroids could potentially be co-cultured with cancer cells in order to investigate this phenomenon further.

Chapter 5:

Migration and blebbing dynamics of single glioma cells

5.1 Introduction

Cancer is the second leading cause of death in the U.S., with an overall loss of \$263.8 billion in medical and morbidity costs¹³⁰. Glioblastoma multiforme (GBM) originates from the glia or its precursors in the central nervous system¹³¹. Characterized as a grade IV tumor by the World Health Organization, GBM is the most aggressive and also the most common glioma in humans¹³². Approximately 15,000 people die of GBM every year¹³³. It can be described as a complex organ lesion with diverse anatomy, genetic mutations, and genetic variability within the tumors^{93,96}. Lack of understanding of causative agents, tumor progression, invasiveness and the location of tumors in vital areas of the brain have limited treatment protocols to surgery, chemotherapy, and radiation therapy, making GBM one of the most difficult conditions to treat. Even with extensive therapy, the median survival rate is only 15 months^{131,135}.

Described as one of the hallmarks of cancer, the ability of tumors to invade surrounding tissues and metastasize to other parts of the body causes 90% of cancer deaths in humans^{98,99}. One of the major challenges in treating GBM arises from its highly invasive behavior, which allows tumors to progress despite surgery, chemo and radiation therapy. About 15-25% of the central nervous system volume is occupied by the extra cellular space, which contains metabolites, hormones, proteins, and extra cellular matrix (ECM) molecules that the glia and neurons produce. It is composed of proteins such as glycosaminoglycans (GAG), hyaluronan (HA), fibronectin, laminin, proteoglycans, and nanofibrous collagen structures¹³⁸. Cells typically attach to and utilize their immediate ECM to migrate. Probing the mechanical components of the extra cellular environment has shown that it directly affects cellular migration,

proliferation, and cytoskeletal organization; thus establishing mechanical stimuli as a necessary factor that influences cellular behavior^{139–141}. It is well known that elasticity (N/m^2) of the environment affects migration¹⁹. The rigidity of the substrate has also been known to alter the cytoskeletal organization of glioma cells¹³⁵ with stiffer constructs enhancing integrin expression and progression¹⁴²s. However, the influence of structural stiffness (N/m) on cell migration has not been investigated. Also, a recent study has suggested that the local mechanical property of the substrate may have a stronger influence on cell behavior than the bulk mechanical property of the substrate⁵⁰. Therefore, it is important to understand the influence of structural stiffness on glioma cell migration to get a better picture of how the biophysical environment influences glioma metastasis.

The normal brain ECM differs significantly from that of patients with GBM. Glioma cells modify their microenvironment as they migrate by rearranging the normal brain ECM (approximate modulus of 500 Pa) to create an ECM that is more rigid to facilitate proliferation^{31,135}. In particular, glioma cells have been known to migrate via normal brain parenchyma, collect below the pial margin, border around blood vessels and neurons and directionally migrate along highly aligned white matter tracts^{54,131,143,144}. Studies on dimensions of white matter tracts show considerable variations suggesting that they can even be characterized into small and larger tracts⁵⁵. Consequently, the range of diameters of these aligned anatomical white matter tracts have been shown to be anywhere from less than 500 nm to 7 μm range^{54–56}. Therefore, suspended, aligned and multilayer nanofibers of varying diameters and lengths serve as an excellent platform to study individual glioblastoma cell behavior *in vitro*. In this study, a constant starting diameter of 400nm is selected to resemble glioma migration in smaller white matter tracts. There are two reasons for starting at a lower diameter: a) in future, we aim to extend the study by progressively exploring glioma migration

in fibers with larger diameters to understand mechanisms by which fiber curvature influences migration, and b) the STEP technique allows high spinnability of polystyrene in 400-900nm fiber diameter range.

In addition to metastasizing and migrating to secondary locations, the ability of cancer cells to resist apoptosis is also described as a hallmark of cancer¹³⁷. A phenomenon that interlinks cytoskeleton organization, migration, and apoptosis is *blebbing*. Observed in the 1900s, blebs were described as blisters that are now characterized as short lived (<1 minute) circular extensions (about 2-15 μ m in diameter) that expand off the cytoplasm and retract to the initial site of origin⁶⁹. While blebs have been associated with apoptosis, migration, cytokinesis, cell spreading, virus infection, cellular protection against injury and migration, it is still a largely unknown phenomenon whose complete functions are yet to be recognized^{72,107-110}. The dynamics of blebbing in cancerous cells requires more attention as it has been associated with invasiveness, ability to escape apoptosis, and motility^{69,145,146}. In 1970, Blaser *et al.* demonstrated how blebbing was used for cellular motility in zebra fish germ cell^{149,150}. Similarly, Babychuk *et al.* showed that human embryonic kidney cells utilize blebs to trap detrimental constituents of the cytosol to enhance survival of injured cells¹⁴⁵. Blebbing has also been associated with changes in nuclear shapes, mitotic disturbances causing genetic instability, and multidrug resistance in tumor cells¹⁵¹⁻¹⁵³. A study by Caspani *et al.* has shown that glioma cells exhibit reversible blebbing and non blebbing phenotypes both *in vivo* and *in vitro*, and that the blebs do not contribute significantly in glioma migration¹⁴⁴. This makes the study of blebs a crucial component in the understanding of glioma migration as blebs are being increasingly associated with tumor cell behaviors.

Using suspended and highly aligned nanofibers in single and multiple layers to represent the

aligned physiologic pathways used by glioma for migration can help us better understand how individual cells are influenced by changes in their microenvironment⁵⁴. In this study, the migratory behavior in response to single nanofiber structural stiffness (N/m), associated cell shape, and blebbing dynamics of malignant glioma cells are investigated^{128,154}.

5.2 Materials and Methods

Cell culture: Passage 18 DBTRG-05MG (Denver Brain Tumor Research Group-05MG) cell line was purchased from ATCC (American Type Culture Collection, Manassas, VA). The cells were maintained in RPMI-1640 media (ATCC), supplemented with 10% FBS (HyClone, Canada), 1% Penicillin/Streptomycin (HyClone, Logan, UT), additional 30mg/L L-proline, 35mg/L L-cystine, 3.57g/L HEPES (4-(2-Hydroxyethyl)piperazine-1-ethanesulfonic acid), 15mg/L hypoxanthine, 1mg/L adenosine triphosphate, 10mg/L adenine, and 1mg/L thymidine (Sigma Aldrich, St. Louis, MO) as recommended by ATCC. Both T75 and T25 cell culture flasks (Corning Inc., Corning, NY) were used to culture the cells at 5% CO₂ and 37 °C in the incubator (Thermo Scientific, Barrington, IL). DBTRG-05MG passage numbers 19-30 were used for data collection. Media was renewed 2 times a week. In order to suspend the cells, media was removed, and the cells were rinsed with PBS twice. They were then dispersed with 0.25% trypsin (HyClone, Logan, UT) for one minute and the cells were resuspended in fresh medium.

STEP fibrous substrate: Substrates of suspended, parallel, and intersecting polystyrene (PS) nanofibers (lengths: 4, 6 and 10mm; diameters: approximately 400nm) were manufactured using STEP platform^{84,128,155,156}. The diameters of the fibers were confirmed using scanning electron micrographs. Square Thermanox® plastic cover slips (NUNC Brand Products, Rochester, NY) were used as frames for the substrates. Subsequently, they were cut out (4, 6,

and 10mm) to form hollow substrates upon which suspended fibers were deposited. The substrates were mounted on glass bottom 6-well plates (MatTek Corp., Ashland, MA), sterilized with 70% ethanol for 5 minutes, rinsed with PBS twice and coated with fibronectin (2 μ g/ml) overnight before seeding the cells. The structural stiffness (N/m) in the middle of suspended fiber (750 μ m on either sides from the center of the fiber span length) was calculated for 4, 6 and 10mm polystyrene fibers by Atomic Force Microscopy (AFM, Veeco BioScope II, Plainview, NY; using tip less cantilevers of stiffness 0.2 N/m from AppNano, Santa Clara, CA). A three-point bending test^{155,157} was used to determine fiber structural stiffness within 750 μ m on either sides from the center of the fiber, and the average values were calculated.

Cell Seeding: The cells were resuspended to obtain a concentration of 400, 000 cells/ml. While 30 μ l of this suspension was placed on the 4x4 and 6x6 mm² fibronectin coated substrates, 60 μ l of the suspension was placed on 10x10 mm² fibronectin coated substrates. The seeded substrates were placed and maintained at 5% CO₂ and 37°C in the incubator until the cells attached onto the nanofibers (2-6 hours). About 1 hour after seeding, 2ml of media was added to each well. Once cells attached, time-lapse video micrographs of the substrates were taken continuously for 10 hours (every 10 or 15 minutes) using Zeiss microscope with incubating capacity (Zeiss AxioObserver Z1, Jena, Germany).

Cell Tracking/Blebbing analysis: Time lapse videos were performed at 10x or 20x magnification and were analyzed using AxioVision software (Zeiss, Germany). Approximately 30 cells were sampled per substrate. Cell displacements were measured every hour from the center of the cell for the entire time-lapse period (10 hours). The highest displacement in the entire 10 hour period was recorded. Cells that migrated less than 10 μ m/hr (about 30%, N=157) were considered, 'non-moving' cells and were not considered further. Cellular migration was

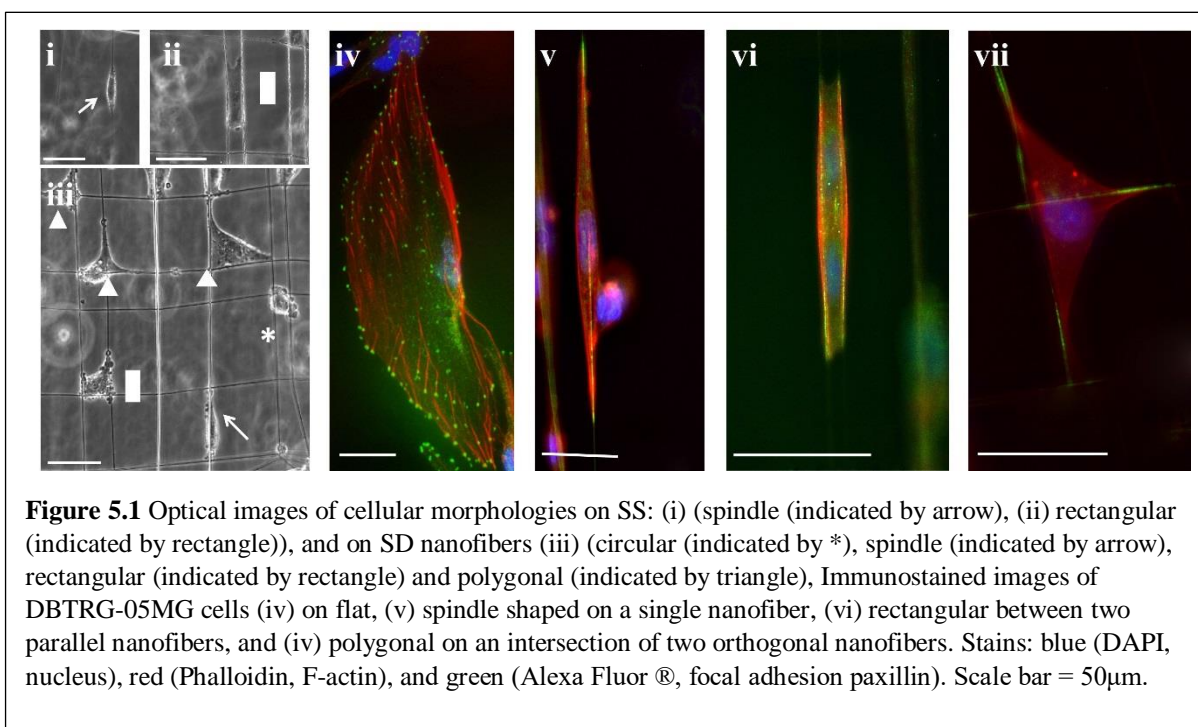
recorded at the middle of the span length of suspended nanofibers (about 750 μ m on either sides from the center of the nanofiber).

Time-lapse video micrographs obtained at 20x were used to analyze the blebbing dynamics of the DBTRG-05MG cells. Using AxioVision software, cell spread area, bleb count, and bleb sizes were measured. Bleb size and count were compared as a function of cell spread geometry or cell size.

Cell cytoskeleton staining: DBTRG-05MG cells on flat and suspended nanofibers were stained for F-actin stress fibers, focal adhesions and the nucleus. The cells were fixed using 4% paraformaldehyde in phosphate buffered saline (PBS) solution for 15 minutes, and washed two times with PBS. The cells were exposed to permeabilization solution (PBS+ 0.1% Triton-X 100 solution) for 15 minutes, PBS washed twice, soaked in anti-goat blocking buffer (Invitrogen, Grand Island, NY) for 30 minutes, and PBS washed twice. Diluted primary paxillin (pY31, Invitrogen, Grand Island, NY) was used (PBS with 1% Bovine Serum Albumin and Triton-X 100, 1:100 dilution ratio), and the substrates were refrigerated (2-8 $^{\circ}$ C) for 1 hour. After washing it with PBS three times, the secondary stain (anti-goat, anti-rabbit, Alexa Fluor 488 or 647, Grand Island, NY) and Phalloidin (Santa Cruz Biotechnology, Santa Cruz, CA) were used at 1:200 dilutions. The substrates were placed in room temperature for 1 hour, away from light. After washing with PBS three times, DAPI (4',6-diamidimo-2-phenylindole) was used to stain the nucleus for 5 minutes. The substrates were then rinsed with PBS two times, and observed using Zeiss $^{\circ}$ microscope.

Statistical Analysis: JMP software was used to analyze the data for statistical significance. ANOVA and Student's t-tests were used to test for significant differences between variables when required.

5.3 Results



Our previously reported non-electrospinning *pseudo dry-spinning* method called the STEP technique is able to deposit highly aligned polymeric micro/nanofibers in single and multiple layers. The fiber networks have uniform diameters and can be manufactured at user defined geometrical spacing (Chapter 11, Fig. 11.1)^{80,128}. Specifically, high aspect ratio (length/diameter) fibers can be precisely deposited with control on fiber dimensions (diameter: sub 100 nm-micron, length: mm-cm, parallelism: ≤ 2.5 degrees, spacing: sub-micron to microns) in single and multiple layers. In this study, both highly aligned parallel single suspended (SS) and orthogonally arranged double suspended (SD) fibers were deposited on hollow square plastic frames, and used for migration and blebbing dynamics study. For this study, fiber diameter was kept constant at ~ 400 nm.

DBTRG-05MG cells on flat and STEP fibers:

DBTRG-05MG cells mainly adopted 3 major morphologies on STEP fibers: spindle shape on

single fibers, rectangular shape on parallel fibers and polygonal shape at orthogonal fiber intersections (Fig. 5.1). In spindle shaped cells (Fig. 5.1 (i) and (v)), the nucleus was predominately located at the cell center. The stress fibers were around the nucleus connecting the poles of the spindle, and focal adhesions were concentrated near the poles of the spindles with occasional expressions along the cell-fiber interface. Cells between two parallel nanofibers formed (Fig. 5.1 (ii) and (vi)) rectangular cell structures with nucleus at the center and stress fibers mostly around the perimeter. Focal adhesions were mostly concentrated in the corners of the rectangular morphologies, with some along the cell-nanofiber interface. On orthogonal fibers, cells formed polygonal (kite like) structures (Fig. 5.1 (iii) and (vii)) with nucleus at the center. Focal adhesions were pronounced in the corners of the cell with occasional expressions along the cell-nanofiber interface.

On flat control substrates however, DBTRG-05MG cells mostly showed spread configurations with pronounced focal adhesions around the circumference of the cells (Fig. 5.1 (iv)). Stress fibers were visibly seen to be connecting the focal adhesions forming netlike structures of the cytoskeleton. Cells were observed to migrate at about $30\mu\text{m}/\text{hour}$ on average on flat, and were

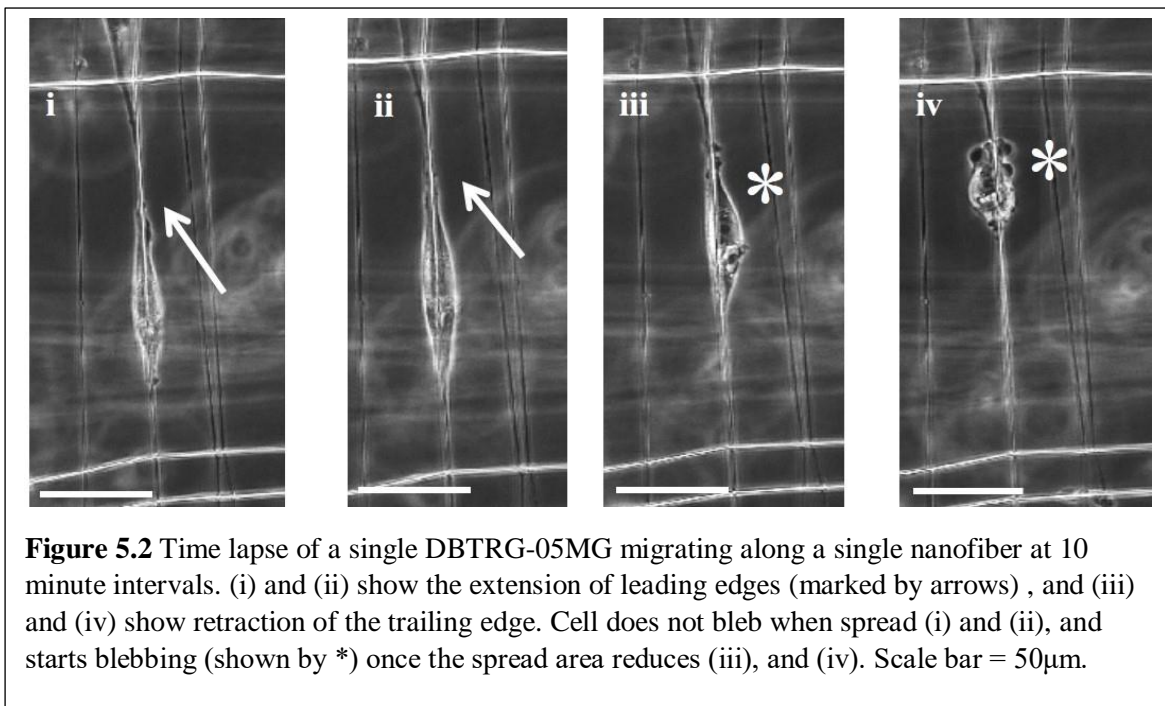


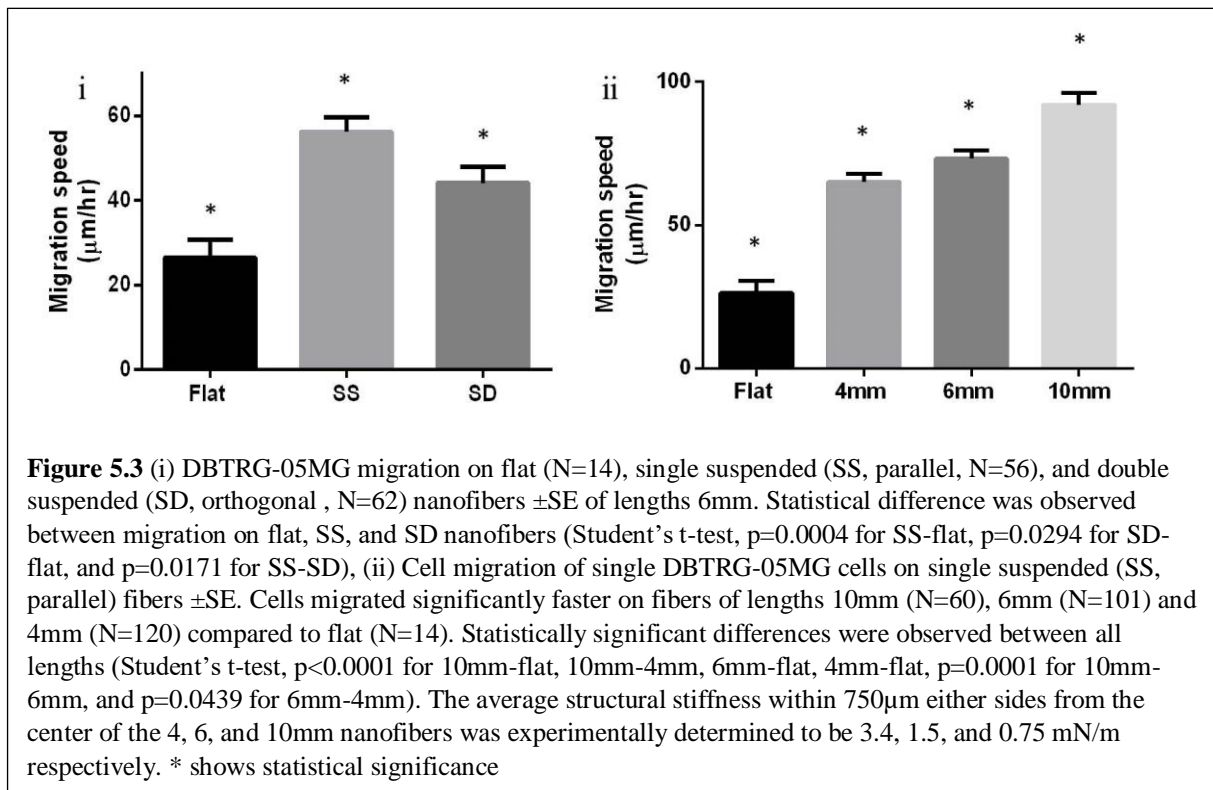
Figure 5.2 Time lapse of a single DBTRG-05MG migrating along a single nanofiber at 10 minute intervals. (i) and (ii) show the extension of leading edges (marked by arrows) , and (iii) and (iv) show retraction of the trailing edge. Cell does not bleb when spread (i) and (ii), and starts blebbing (shown by *) once the spread area reduces (iii), and (iv). Scale bar = $50\mu\text{m}$.

found to have no obvious directional bias.

DBTRG-05MG migration on STEP nanofibers:

Cell migration has been described as a multi-step process involving polarization of the cell, extension of protrusion at the leading edge, contraction of the actomyosin complex, proteolytic degradation of ECM and retraction of the trailing edge⁸⁶. Using STEP platform, the polarization, extension of protrusions at the leading edge, and retraction of the trailing edge of a single cell on a single nanofiber were captured using time lapse images (Fig. 5.2). Cells polarized, extended their leading edge, and retracted their trailing edge like a ‘sling shot’ on single nanofibers.

As tumor cells start remodeling their environment through increased cross linking, the associated increase in ECM stiffening has been observed to affect focal adhesion expression and metastasis^{17,142}. Prior studies have observed that tumor environments are stiffer than



normal ECM, and the stiffness of ECM influences cancer cells^{17,31,48,142}. Therefore, we investigated the difference in migration speeds of DBTRG-05MG on SD (2 layers of orthogonally arranged fibers, Chapter 11, Fig. 11.1) versus SS (a single parallel layer of fibers) and the role of structural stiffness within SS. It was observed that glioma cells spread more and migrated significantly slower on double suspended (SD) fibers when compared to cells on parallel single suspended (SS) fibers and on flat (Fig. 5.3 (i)).

Furthermore, single suspended (SS) nanofibers of lengths 4, 6 and 10mm were used to study DBTRG-05MG migration behavior on single fibers. Migration data was generated from cells attached at the middle of the span lengths (about 750 μ m either side from the center of the nanofiber). Nanofiber length significantly increased cell migration and cells migrated the fastest on 10mm nanofibers among the three lengths tested (Fig. 5.3 (ii)). The cells migrated significantly faster on all three lengths tested when compared to flat. Compared to currently reported values in literature for glioma migration (0.4 to 100 μ m/hr)¹⁵⁸, in this study, cells were observed to migrate at higher end of this range. Glioma migration speeds from 13-196 μ m/hr were recorded on STEP fibers.

Blebbing dynamics:

DBTRG-05MG cells demonstrated relatively continuous blebbing on flat surfaces (Fig. 5.4 (I)) and exhibited an interesting reversible blebbing-non blebbing phenomenon on suspended fibers (Fig. 5.4 ((II-IV))). As blebbing has been associated with migration, resistance to cell death and multi drug resistance^{145,153}, it is important to study the blebbing behavior of glioma cells as they migrate. In particular, we investigated the relationship of blebbing as a function of cell migration and spreading on our STEP fibers. Not all the cells demonstrated plasma membrane blebbing (percentage of blebbing cells: 65% (N=349) on flat, and 36% (N=248) on STEP

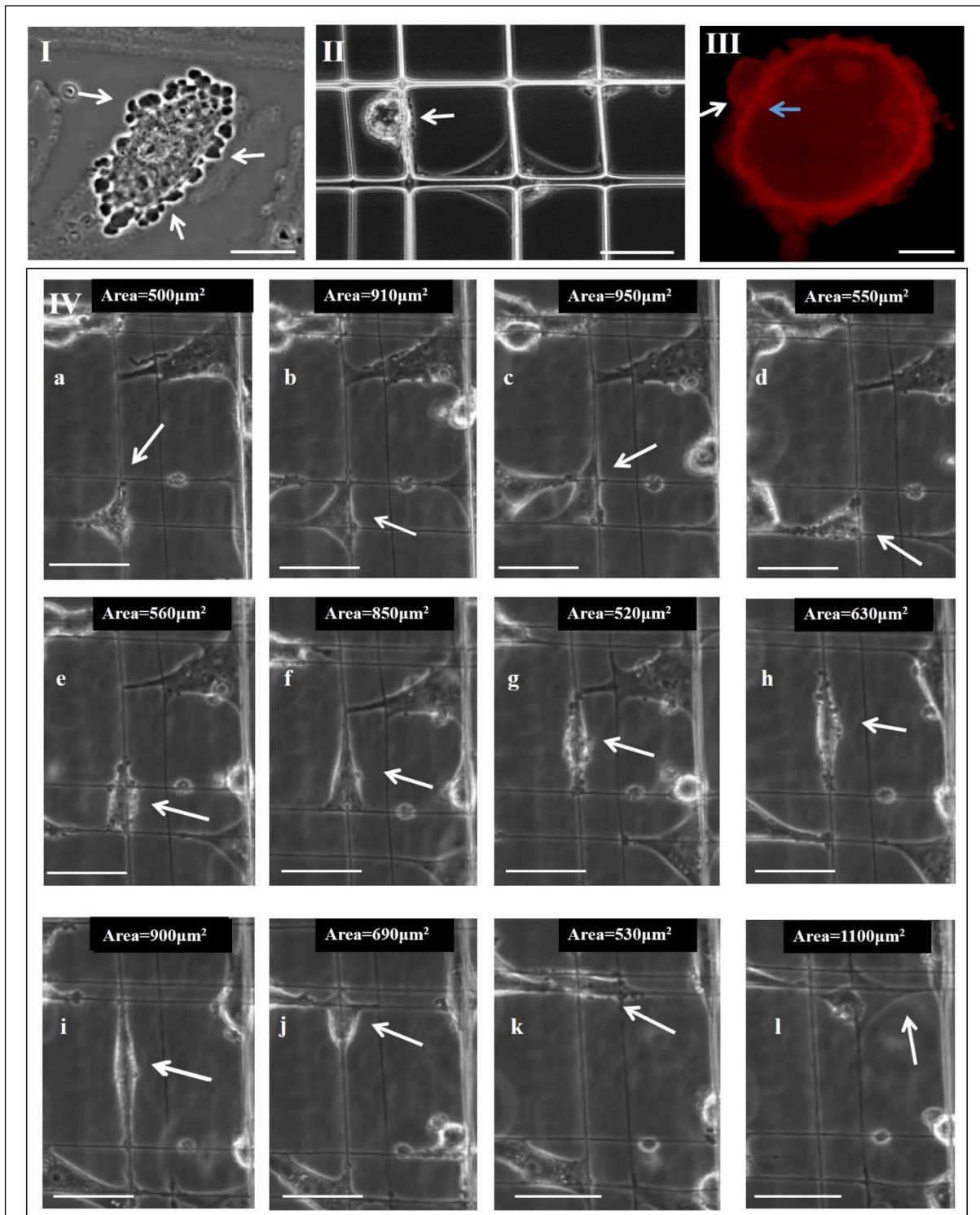
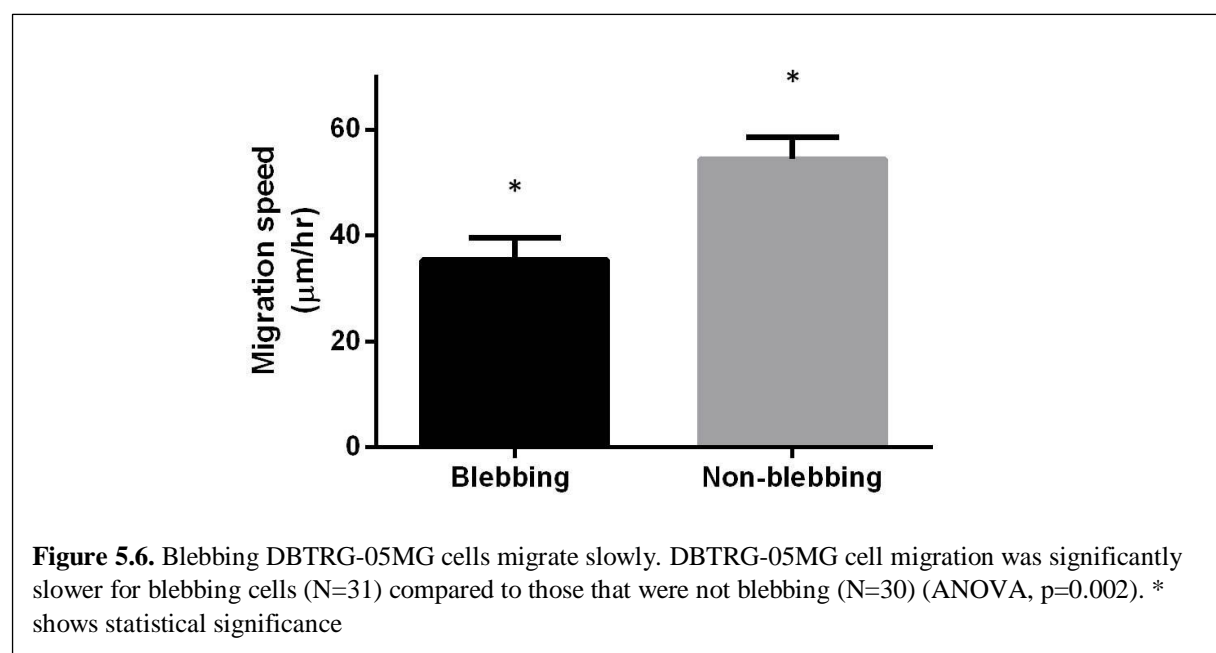
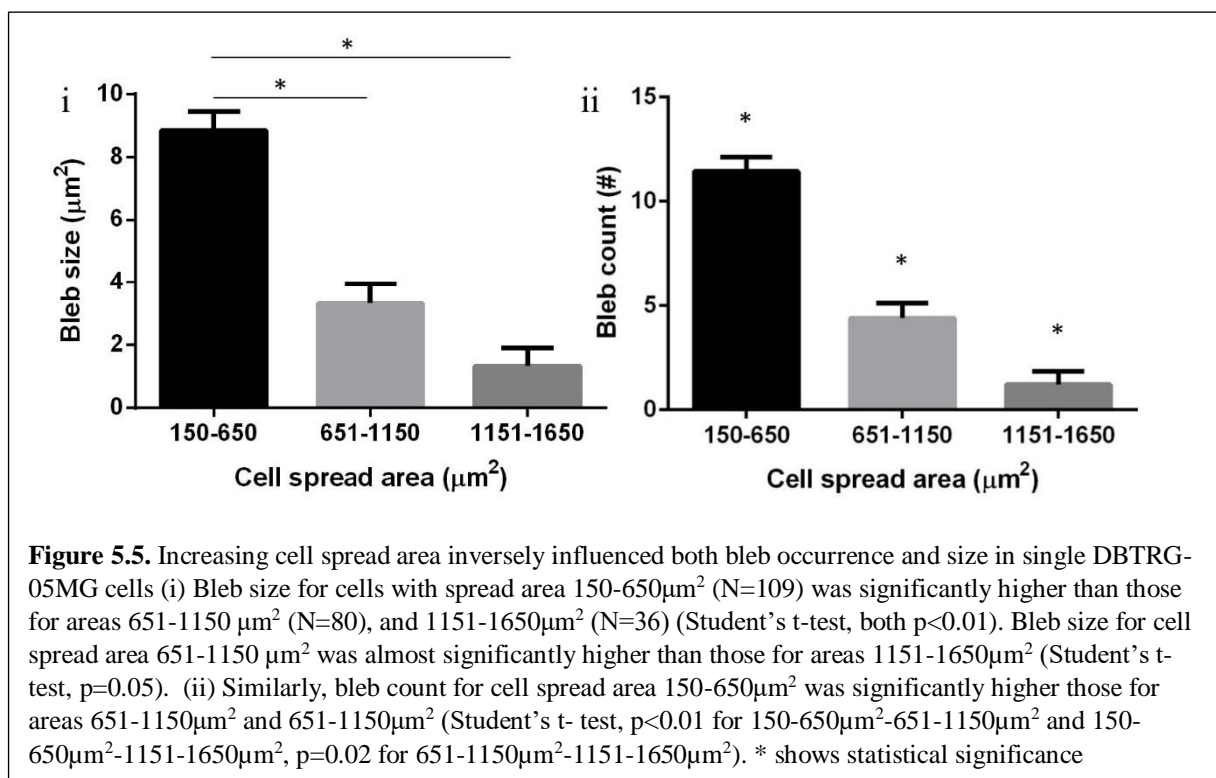


Figure 5.4. DBTRG-05MG cell blebbing dynamics. (I) Continuous plasma membrane blebbing of DBTRG-05MG on flat, (II) While the spread cell has no blebs, the circular cell (shown with an arrow) is blebbing on suspended fiber networks, (III) Actin (Phalloidin) immunofluorescent stain of a blebbing DBTRG-05MG. The bleb actin cytoskeleton (white arrow) of the bleb is separated from the actin cortex (blue arrow). Scale bars are 20 μm , 50 μm and 5 μm for (I), (II), and (III) respectively, (IV) Time lapse images at 20 minute intervals of DBTRG-05MG cell blebbing dynamics on STEP fibers (shown using arrow). Blebbing decreases or disappears as cell spreads along the nanofibers (b, c, f, i, j, l), and increases or reappears as cells reduce their spreading area (a, d, e, g, h, k). Scale bar is 50 μm . Respective cell spread areas are shown on top right corners.

fibers), and those cells that exhibited this phenomenon were considered for blebbing dynamics



study. We observed that blebs on a single cell were more in number (count) and larger in size when cells were in smaller, spherical morphologies. As cells spread along the STEP nanofibers (both SS and SD) and increased in spread area, both bleb size and their occurrence count decreased (Fig. 5.4 (II-IV), and Fig. 5.5). Furthermore, it was observed that blebbing cells had significantly lower migration than cells that were not blebbing (Fig. 5.6). Both bleb size and count showed a decrease in blebbing as the cells spread in area, and a near elimination of

blebbing at a cell spread area of about $1400\mu\text{m}^2$ and beyond. However, as highly spread cells retracted to smaller areas, re-occurrence of blebbing was observed (Fig 5.4 (IV)). This reversible blebbing non-blebbing phenomenon based on cell spreading, to the best of authors' knowledge, has not been reported before. Characterizing the occurrence of blebbing with respect to glioma cell migration can add to our understanding of cell migration specific apoptotic and drug resistance behaviors.

5.4 Discussion and Conclusion

Glioma is an integral system that nurtures itself by conditioning its microenvironment and vice versa. In order to understand the comprehensive migratory and invasive behavior of glioma cells, a thorough understanding of cell-microenvironment interaction is necessary. It is thus essential for *in vitro* platforms to recapture the *in vivo* glioma migration environment. Current methods of simulating the ECM environment involve both 2-D and 3-D substrates. As glioma metastasis is known to be favoured by aligned physiological structures such as white matter tracts, suspended and aligned fibers like the STEP fibers serve as an improvement over the conventionally used 2D and 3D platforms to study glioma migration. While studies have reported the material stiffness (N/m^2) of white matter tracts in the range of 2.5-10kPa.^{159,160}, reference to their structural stiffness is not available. Using the STEP platform, the structural stiffness of the fibers were altered by choice of fiber length. As structural stiffness decreased with fiber length, cell migration increased. This effect of structural stiffness on cell migration is a new finding and we hope that this will encourage the community to investigate this in detail.

Cytoskeletal staining and time-lapse images of DBTRG-05MG suggested that cellular shape and migration are different on conventionally used flat and suspended STEP fibers. Caspani *et*

al. has observed that actin fibers align along the white matter tracts in migratory glioma cells *in vivo*, similar to what we observed when DBTRG-05MG aligned along the STEP fibers¹⁴⁴. DBTRG-05MG cells acquired 3 major morphologies while interacting with the nanofibers, and most focal adhesions were observed in the poles of the cells (Fig. 5.3). Although the relationship between focal adhesion and cell migration is not understood well, focal adhesion size has been associated with cell migration¹⁶¹. We observed that the DBTRG-05MG cells expressed different focal adhesion patterns on STEP fibers when compared to cells on flat substrates which could suggest why they migrated at different speeds on flat and on the fibers. However, this relationship needs further investigation.

Blebbing and its influence in cancer requires more investigation as the study shows that cell spreading can significantly reduce blebbing. One of the causes of blebbing is explained as the rupturing of this actin cortex, and the propulsion of cytoplasmic contents out of the ruptured site⁶⁹. As the cell re-establishes its ruptured actin, blebs retract back to the initial site of propulsion. Actin structures in spherical and spread cells could possibly explain this inverse relation of blebbing and cell spreading. In spherical cells, actin is mostly present in the circumference as actin cortex²³ which acts as a single barrier. Once this barrier ruptures, cytoplasmic contents freely expel out from the ruptured region. In spread cells however, actin stress fibers form net like structures¹⁶² and organize along the perimeter, thus acting as a series of multiple barriers that can possibly decrease the likelihood of bleb formation.

This phenomenon is particularly interesting as blebbing is characteristic of amoeboid migration in cancerous cells¹⁴⁶. Described as one of the modes of cancer migration, amoeboid migration is adopted by cancerous cells in their circular configurations which allow the cells to squeeze through pores in the ECM and migrate without degrading the ECM⁸⁶. Linear regression

analysis suggests that the DBTRG-05MG cells form little or no blebs when they are spread beyond an area of about $1400 \mu\text{m}^2$. It was also observed that blebbing decreased cellular migration. This suggests that amoeboid mode of migration is slower, and is least likely to occur when the cell spreads beyond this threshold. Blebs have also been associated with resistance to cell lysis, drug resistance, and cell survival¹⁶³. Therefore, for better prognosis of cancer, a better understanding of migration and blebbing dynamics is necessary.

Cancer is a system that is influenced by both the biophysical and the biochemical aspects of the tumor microenvironment. Studying cancer cell behavior in environments that resemble glioma migration pathways is therefore critical. This study utilizes a non-electrospinning platform to study cytoskeletal, migration and blebbing dynamics of glioblastoma cells and suggests that glioma cells behave differently on conventionally used flat and suspended STEP nanofiber platforms. Hence, it can be expected that the presented glioma cell behavior might represent a closer resemblance to *in vivo* glioma migration.

While biochemical components may be equally important, we show for the first time that changes in structural stiffness and organization of individual fibers in the microenvironment can significantly alter cell behavior. The change in migratory and blebbing behavior as a function of cellular spreading could also have clinical implications associated with metastasis and resistance against anticancer drugs. Cellular spreading has been related to reduced blebbing. However, the nature of reversible blebbing and non-blebbing behavior of glioma cells warrant further investigation. The unique strategy of investigating cancer cell behavior and dynamics in a fibrous environment can also be coupled with studies of biochemical cues to advance our current understanding of cancer. Our future works will focus on determining the effect of fiber diameter, curvature and tension on migration dynamics and vulnerability of cells to anticancer agents or lysis under spread configuration.

Chapter 6:

Single glioma cell forces

6.1 Introduction

To obtain a better prognosis of diseases, a comprehensive understanding of genomic, phenotypic, biophysical and biochemical signatures at the single and population level is necessary. Such a holistic scientific knowledge is especially critical for understanding a heterogeneous and complex disease like cancer which is one of the leading causes of death in the United States¹³⁶. Extensive genetic, cellular and biomolecular research in the last century has led to the development of novel anticancer treatment options such as gene and hormonal therapy and identified critical genetic mutations^{164–166}. However, scientific investigations underscoring the importance of single cancer cell biophysics have been recognized only in the last few decades¹⁶⁷. While it is well accepted that forces are ubiquitous in the body, their exact role in causing cells to go rogue in disease models is poorly understood.

Studies have shown that cancer cells pull onto and remodel their fibrous ECM to facilitate invasion. Furthermore, highly aligned tumor associated collagen signatures (TACS) associated with invasive breast cancers underscore the importance of aligned structures facilitating invasion in cancer and also put forward the need to investigate the two way force communication between single cancer cells and their surrounding environment. In this regard, the biological and mechanistic causal relationships during disease onset and progression need to be studied both at the single and population levels^{10,17}. These biophysical interactions can be primarily divided into “outside-in” or external force application onto a cell, and “inside-out” or internal force generation¹⁶⁸. Tools and techniques like atomic force microscopy (AFM)¹⁶⁹, glass micro-cantilevers¹⁷⁰, optical traps¹⁷¹, magnetic tweezers¹³⁹, micropipette aspiration¹⁷², cell compression⁹⁰, fluid flow¹⁷³, and acoustic waves¹⁷⁴ have been used to probe the influence

of ‘outside-in’ forces on cancer cells. Similarly, micropillars¹⁷⁵, traction force microscopy¹⁷⁶, and wrinkling membranes¹⁷⁷ have been used to study the ‘inside-out’ biophysical interactions of cells^{178,179}. While these platforms have indeed provided a deeper understanding of mechanotransduction and cell-substrate interactions, interpretation of data from a cell-ECM perspective is still challenging since the platforms do not closely represent the native ECM.

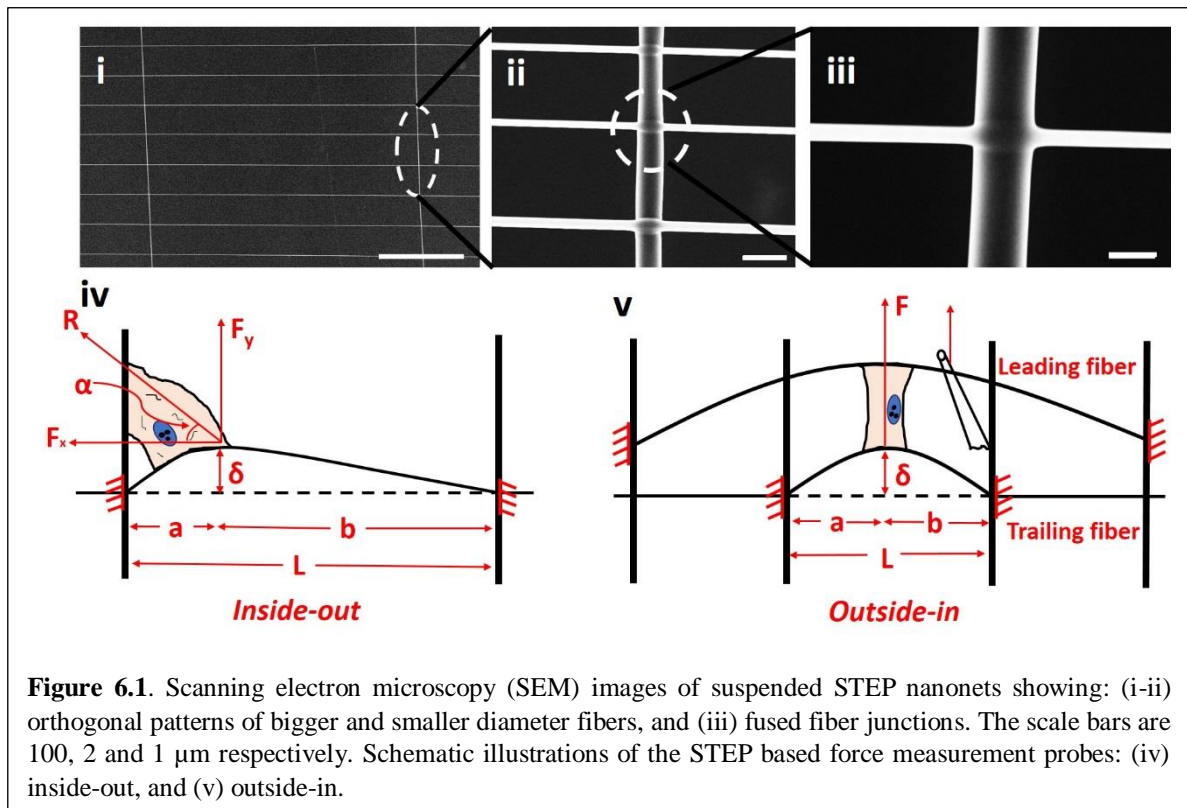
ECM consists of protein fibrils (30–70 nm in diameter), which can bundle into 200 nm–1 μ m fibers. ECM serves as a scaffold upon which most cells in the body attach and receive mechanical and chemical cues. Newer technologies are making it increasingly possible to study cellular interactions at the submicron and nano length scales. Of these, the most abundantly used cell culture systems include 2D flat substrates which are coated with native ECM proteins and 3D gel systems. These systems are engineered to provide cells with gradients of elasticity (elastic modulus, N/m²) and have shown remarkable changes in cell behavior including differentiation and migration^{16,180–182}. In contrast to these cell culture systems, we have demonstrated that *suspended* and *aligned* nanofibers with diameters in the range of ECM proteins and white matter tracts can cause cells to react to structural features, such as curvature, topography, and structural stiffness (N/m)^{87,183}. Therefore, changes in individual fiber properties have the potential to produce large changes in individual cell response, as measured by any number of metrics including cytoskeletal arrangement, nucleus shape index, focal adhesion distribution, and migration speed^{82,87,183}. The mechanical properties of stiffness (modulus: N/m² and structural: N/m) and curvature of the fibers present the cell with 1, 2 and 3D modes of interaction. Cells are aligned along the fiber axis (1D), stretch between two fibers (2D) and are able to sense the curvature of fibers (3D). Thus, suspended and aligned fiber networks provide a new class of mechanistically tunable biological assay which morphologically begin to represent the diameters of the aligned white matter tracts of the glioma environment.

Here, we utilize our previously reported non-electrospinning Spinneret based Tunable Engineered (STEP) technique^{82,85-87} to manufacture suspended and aligned nanonets to investigate single cell behavior (*inside-out* and *outside-in* force modulation) of a glioblastoma cell line (Denver Based Tumor Research Group-05MG, DBTRG-05MG). In a previous study, we showed that DBTRG-05MG cells migrated up to three times faster on suspended fibers, with migration speed inversely related to the structural stiffness (N/m)⁸⁷. This highlights the fact that cells behave differently when presented with different substrates. Hence, it is critical to develop *in vitro* platforms that closely represent the tumor microenvironment of the white matter tracts which have been shown to range from less than 500 nm to about 3 μ m in diameter⁵⁴⁻⁵⁶. The STEP technique allows for the deposition of suspended and aligned polymeric fibers whose diameters are in the range of the white matter tracts thus creating an *in vitro* platform that topographically represent the aligned glioma microenvironment. Using this platform, in the first part, the contractile forces of DBTRG-05MG cells attached to suspended fibers (*inside-out*) are investigated with and without the presence of the cytoskeletal compromising drug, cytochalasin D. In the second part, single cells attached to two parallel and suspended fibers were perturbed using a micromanipulated glass micropipette to investigate the '*outside-in*' response of the cells to external forces with the presence of cytochalasin D in varying concentrations. This drug was selected due to its ability to severely disrupt actin cytoskeleton and form actin aggregates in the cells^{184,185}. Actin is one of the key proteins that is responsible for force exertion and mechanical transduction^{186,187}. Therefore, by gradually compromising the actin cytoskeleton of the cells, this single cell glioma model describes a systematic spatio-temporal investigation of the influence of cytochalasin D concentration on the ability of single DBTRG-05MG cells to exert forces and their capability to withstand external forces.

6.2 Materials and Methods

STEP nanonet manufacturing: Polymeric solutions of polystyrene (Scientific Polymer Products Inc., Ontario, NY, M_w : 2×10^6 g.mol⁻¹) dissolved in xylene (Fisher Scientific, Pittsburgh, PA) at 14% and 5% (w/w) were prepared. Plastic coverslips (Fisher Scientific, Pittsburgh, PA) were cut to 2 mm×2 mm hollow frames and used as substrates. Suspended and aligned polystyrene (PS) nanofibers of diameters 1 μ m and 200-300 nm were deposited onto a rotating plastic hollow frame (3 rotations per minute) in crisscross patterns using the STEP platform at room temperature and 15% relative humidity (Fig. 6.1(i)). Using a custom solvent evaporation-based fusing method, the nodes of the crisscross patterned nanofibers were fused to form STEP nanonets with clamped boundary conditions (Fig 6.1 (ii-iii)). Using high vacuum grease (Dow Corning, Midland, MI), the substrates were mounted on glass bottom 6-well plates (MatTek Corp., Ashland, MA) and sterilized with 70% ethanol and ultraviolet rays in a sterile hood for 20 minutes. The ethanol was aspirated, the substrates were rinsed with phosphate buffered saline (PBS, Fisher Scientific, Pittsburgh, PA) twice, and the fibers were coated with fibronectin from bovine plasma (8 μ g/ml, Sigma- Aldrich, St. Louis, MO) for at least an hour at 37°C before seeding the cells.

AFM based stiffness measurement: The nanonets were modeled as a tie rod and the stiffness values were obtained using the deflection equation for a rod¹⁸⁸ and the tensile forces obtained from AFM (Veeco NanoScope IIIa, New York); using DNP S-10 cantilevers of stiffness 0.175-0.7N/m from Bruker, California. The measurements were made in contact mode, and the stiffness of the cantilever was measured every time before use (Chapter 11, Table 1).



Cell culturing: Denver Brain Tumor Research Group-05MG (DBTRG-05MG, ATCC CRL-2020) were purchased from American Type Culture Collection (ATCC, Manassas, VA) at passage 18. As recommended by the ATCC, the cells were maintained in RPMI-1640 media (ATCC, Manassas VA), supplemented with 1% penicillin/streptomycin, 10% fetal bovine serum (FBS, Fisher Scientific, Pittsburgh PA), 30mg/L L-proline, 35mg/L L-cystine, 3.57g/L HEPES (4-(2-hydroxyethyl)piperazine-1-ethanesulfonic acid), 15mg/L hypoxanthine, 1mg/L adenosine triphosphate, 10mg/L adenine, and 1mg/L thymidine (all purchased from Sigma-Aldrich, St. Louis, MO) at 5% CO_2 , and 37°C incubator in T25 cell culture flasks (Corning Inc., USA). In order to seed the cells on STEP nanonet scaffolds, the media was aspirated out of the culturing flasks, the cells were rinsed with PBS twice, incubated with 500 μl of 0.25% trypsin (HyClone, USA) at 37°C for 5 minutes, and resuspended in fresh RPMI-1640 media. The cell suspension was then placed on top of the fibronectin coated nanonet scaffolds. After seeding the DBTRG-05MG cells on the scaffolds, the well plates were incubated at 37°C and

5% CO₂. An hour after cell seeding, 2ml of fresh media with 3% penicillin/streptomycin (Fisher Scientific, Pittsburgh, PA) was added to the wells.

Inside-out force measurement: As DBTRG-05MG cells stretched along the STEP nanonets, the smaller diameter fibers (diameter ~200 nm) of the STEP nanonets deflected (Fig. 6.1 (iv)). Using AxioVision software, the point of maximum deflection of the smaller diameter 'a', fiber deflection 'δ', and the respective angle of deflection 'α' (line drawn along the cell boundary signifying high concentration of F-actin stress fibers) were measured. Using the structural stiffness values obtained from AFM and equation (Chapter 11, Table 1) the resultant inside-out force, 'R' was calculated for 0.0, 0.05, 0.1, 0.2, and 0.5 μM cytochalasin D concentrations.

Outside-in measurement: DBTRG-05MG cells that were attached to two parallel small diameter fibers (diameter ~300nm) in the STEP nanonets forming rectangular shapes were chosen for *outside-in* measurements (Fig. 6.1(v)). Using a glass micropipette attached to 3D automated stage (Sutter Micromanipulator, Novato, CA), the probe was moved at 2 μm/s. An average 25% strain was applied to the cell followed by immediate retraction of the micropipette and return of the nanofiber to its original state. A total of 5 cycles for each data point were recorded. For each drug exposure, force experiments were conducted at t=0, 3, 6, 12, 18, 24 and 30 minute time intervals. Using AxioVision software, the deflection of the trailing fiber was measured and used for calculating the 'outside-in' force exerted by the cells without and with 0.05, 0.2, and 2 μM drug exposure. The equations used to calculate the outside-in forces have been included in Chapter 11, Table 1.

Drug studies: Cytochalasin D (Enzo Life Sciences, Farmingdale, NY) known to prevent actin polymerization was used in this study. For 'inside-out' and 'outside-in' experiments,

cytochalasin D was diluted using RPMI-1640 media. Before the start of the experiment, the diluted solutions were used to produce 0.05, 0.1, 0.2, 0.5, 1.0, 2.0, and 3.0 μM cytochalasin D solutions for 2 ml of RPMI-1640 media in the following manner: The amount of drug required to produce the required concentration was mixed with 0.5 ml RPMI-1640 media. The scaffolds were cultured in 1.5ml of drug free media. Just before start of force experiments, 0.5 ml of media with respective drug concentrations was added to the well plates.

Imaging: Once the cells attached onto the STEP nanonets, time lapse-videos of the scaffolds were taken using a microscope with incubating capacity (Zeiss AxioObserver Z1, Thornwood, NY). Time-lapse videos were taken at 10 frames per hour for 6 hours (*inside-out*) and 0.7 seconds for 1 minute (*outside-in*) using $20\times$ phase objectives and an AxioCam mRm camera. Images were analyzed for cell spread area, and fiber deflections using the AxioVision software (Zeiss, Thornwood, NY).

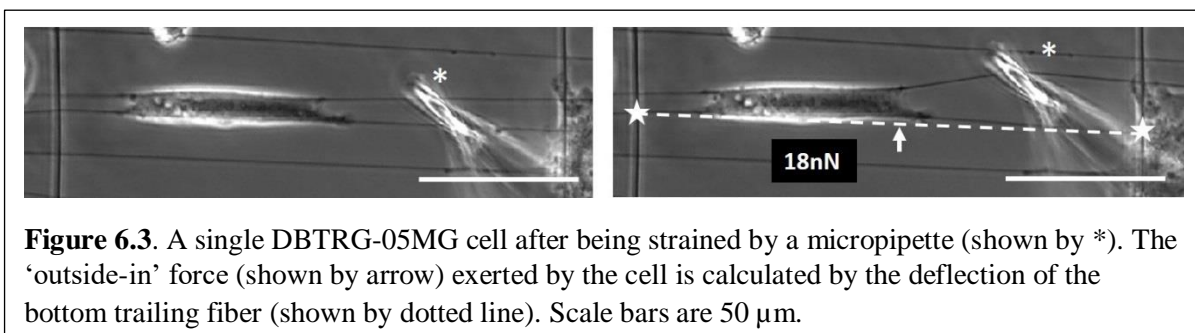
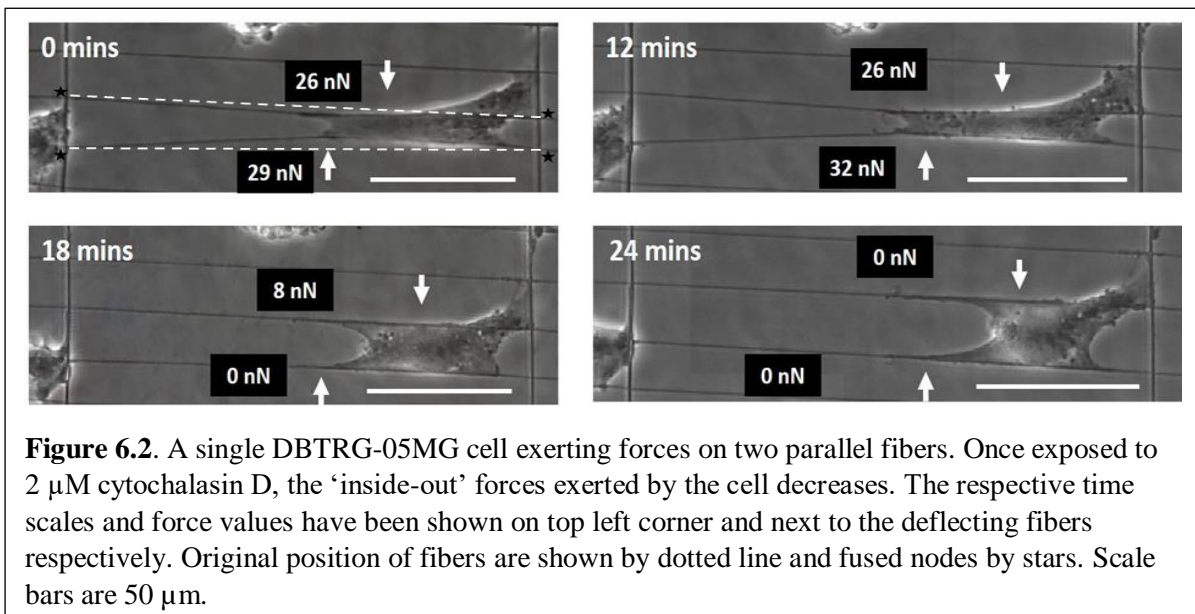
Statistical analysis: GraphPad Prism software (GraphPad Software, Inc., La Jolla, CA) was used to conduct statistical analysis of the data. D'Agostino & Pearson omnibus normality test was used to determine if the data was normally distributed. Depending on the normality of the data, non-parametric Kruskal-Wallis test or ANOVA was used to determine statistical significance. A p-value of 0.05 was used. Standard error was calculated and plotted as error bars for figures.

6.3 Results and Discussion

STEP nanonets:

Using previously reported STEP technique, suspended and aligned bigger (800 nm-1 μm) and smaller (200-300 nm) diameter nanofibers were deposited in orthogonal patterns (Fig. 6.1 (i,

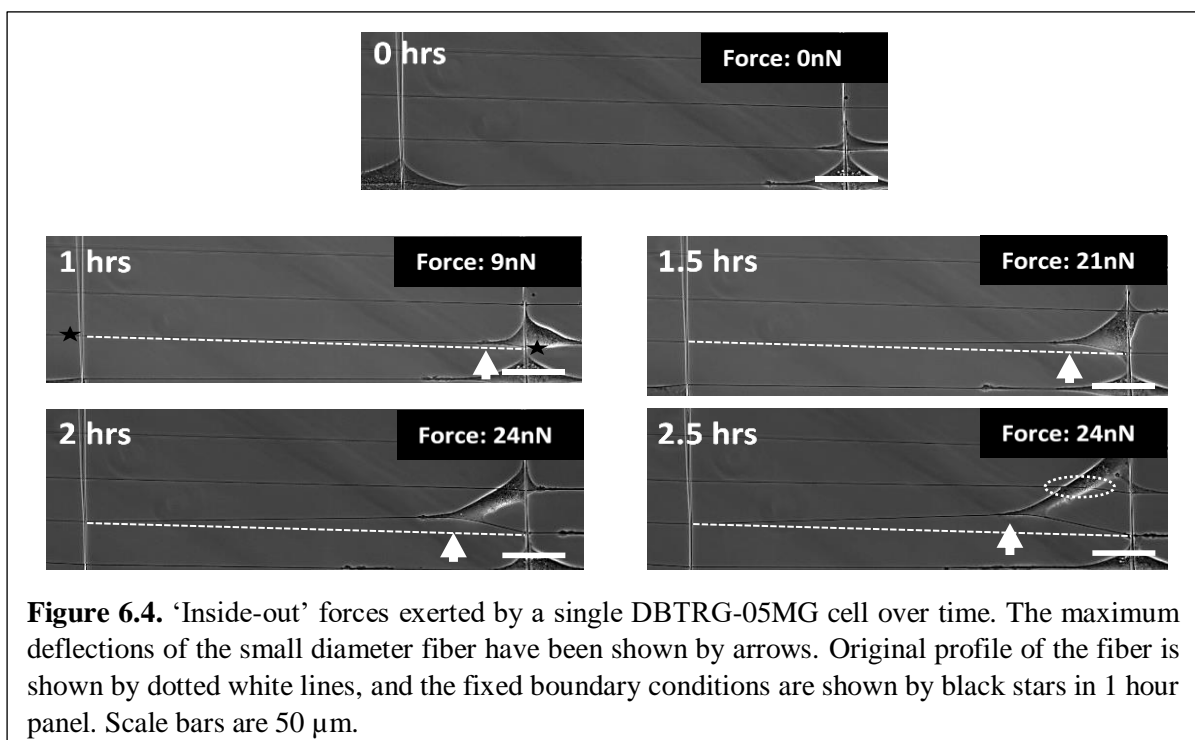
ii)). These high aspect ratio fibers were deposited precisely to control the spacing between the bigger diameter fibers at about 300 μm to observe measurable fiber deflections, and those between the smaller diameter fibers at 30 μm to facilitate single fiber deflections, and 10 μm to facilitate rectangular cell morphologies for ‘inside-out’ and ‘outside-in’ force perturbation experiments, respectively. SEM images of the nanonets showed fiber fusions at intersections (Fig. 6.1 (iii)). Similarly, the fiber junctions maintained their boundary conditions (Chapter 11, Fig. 11.2) and remained fused during DBTRG-05MG-nanonet interactions. Smaller diameter fibers exhibited an average deflection of 3.1% and 4.2% of the lengths of fibers during inside-out and outside-in experiments respectively. Due to the maintenance of fixed boundary conditions and low fiber deflections, the fibers were modeled as elastic beams with fixed boundary conditions (Chapter 11, Table 1) ^{81,189–191}. During the fiber manufacturing process, solvent evaporation causes tension in the fibers, thus making them structurally stiffer. In order



to obtain the structural stiffness (N/m) along the length of the fiber, AFM three point bending tests were conducted^{83,157,192}.

STEP nanonet based Inside-out and Outside-In Force Platforms:

Using STEP nanonets, the biophysical interactions of single DBTRG-05MG cells with suspended fibers provide us with new insights in cell shape and motility, which can now be coupled with a force response. In particular, the platform provides the ability to measure the forces exerted by single DBTRG-05MG cells at different cell spread morphologies. Fig. 6.2 demonstrates a single DBTRG-05MG cell exerting contractile ‘inside-out’ force on two parallel fibers. This cell has been exposed to 2 μM cytochalasin D, and over time decreases its ‘inside-out’ force as observed by the decrease in fiber deflection of both the top and bottom parallel fibers. Drug induced force response of the cell can also be evaluated by applying a stretch to the cell and measuring the resultant force (adhesion strength or cyclic response). In this approach, a micromanipulator is used to stretch the leading fiber, while the force response of the cell is measured from the deflection of the trailing fiber (Fig. 6.1(v)). For instance, Fig.



6.3 demonstrates a single DBTRG-05MG cell being stretched by a glass micropipette (shown by star). Using the outside-in platform, the force response of single cells can be studied for a unit constant strain stretch or variable stretch at constant or varying strain rates. Furthermore, these perturbations can be exerted as single excitations or in a cyclic manner. For this study, we have chosen to study the temporal force response of single cells subjected to a constant strain (~25%) using cyclic perturbation (5 cycles) at each interval of time of 0, 3, 6, 12, 18, 24 and 30 minutes following drug administration. In all these cases, the probe was moved at a constant strain rate of 2 $\mu\text{m/s}$ to a fixed cell stretch distance and then retracted. This was performed sequentially five times in a row for each time point and the force values obtained from deflection of the trailing fiber were averaged.

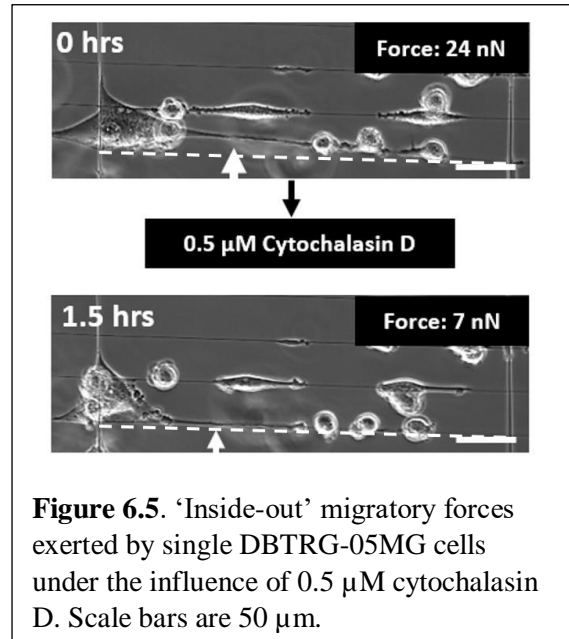


Figure 6.5. ‘Inside-out’ migratory forces exerted by single DBTRG-05MG cells under the influence of 0.5 μM cytochalasin D. Scale bars are 50 μm .

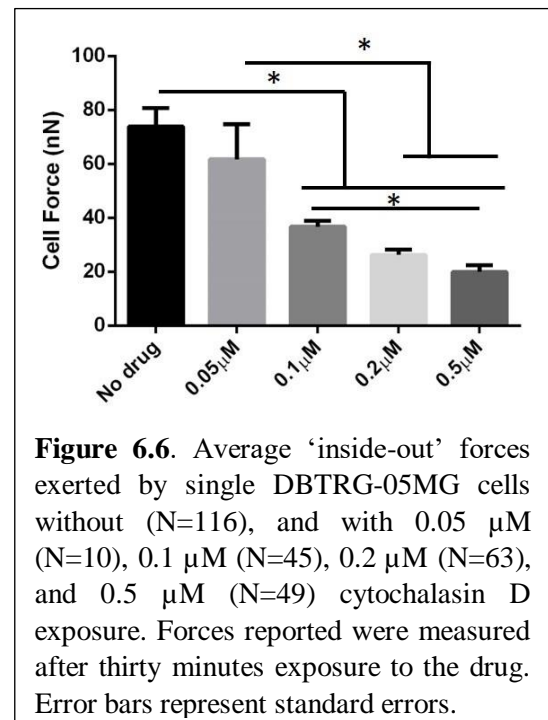


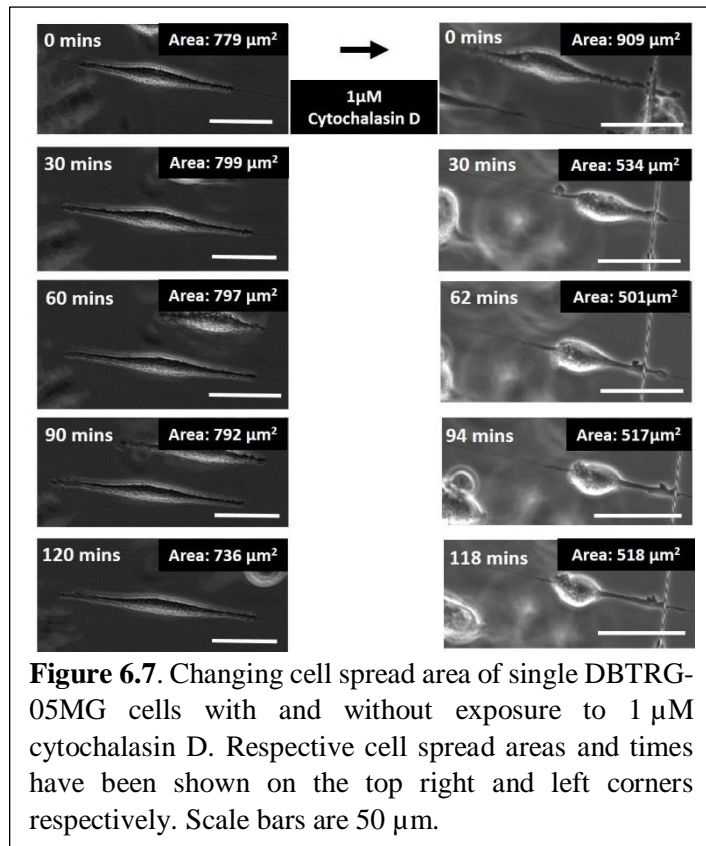
Figure 6.6. Average ‘inside-out’ forces exerted by single DBTRG-05MG cells without (N=116), and with 0.05 μM (N=10), 0.1 μM (N=45), 0.2 μM (N=63), and 0.5 μM (N=49) cytochalasin D exposure. Forces reported were measured after thirty minutes exposure to the drug. Error bars represent standard errors.

Drug Studies:

The ability of cytochalasin D in severely disrupting the organization of actin is well known^{184,185}. However, the influence of this drug on single glioma cell forces and their interaction with suspended nanofibers have not been studied before.

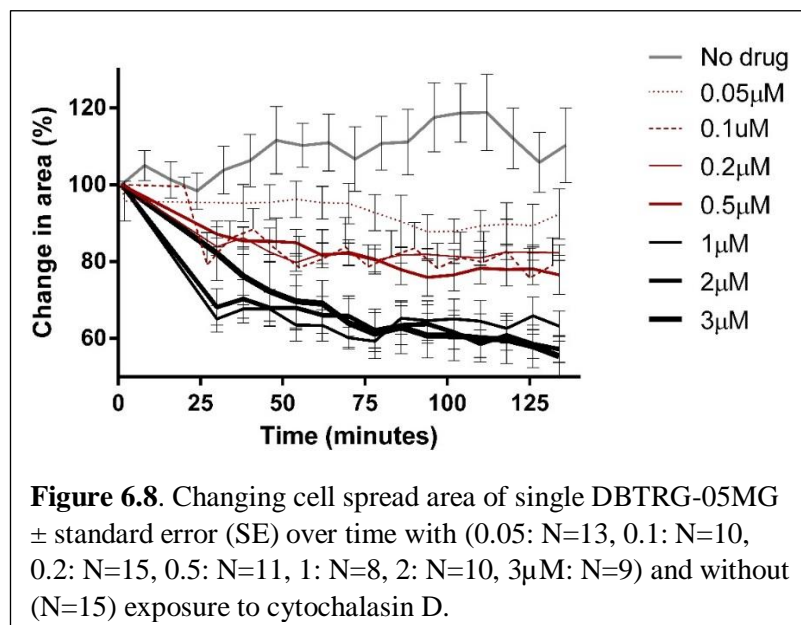
Inside-out: Forces exerted by single cells during stretching caused measurable deflections as illustrated in Fig. 6.4. The measurable ‘inside-out’ migratory forces exerted by single DBTRG-05MG cells ranged from 5-160nN when the cells were exposed to 0.0, 0.05, 0.1, 0.2 and 0.5 μ M cytochalasin D. Cells also interacted with other fibers and the associated forces from these interactions were discarded in the present study (Fig. 6.4, panel 2.5 hours, shown by dashed oval). After the addition of cytochalasin D, ‘inside-out’ forces exerted by single DBTRG-05MG cells decreased immediately. Time lapse images in Fig. 6.5 show the decreased ‘inside-out’ force exerted by a single DBTRG-05MG cell after exposure to 0.5 μ M cytochalasin D. These single cell forces were measured for 0.05, 0.1, 0.2, and 0.5 μ M cytochalasin D exposures. After exposure to 1, 2 and 3 μ M cytochalasin D, the cells almost immediately decreased in size and were unable to exert any measurable ‘inside-out’ forces after 30 minutes on the nanonets. However, force values for 0.05, 0.1, 0.2, and 0.5 μ M were measurable. As these values were not normally distributed (D’Agostino & Pearson omnibus normality test; p-values: no drug: $p < 0.0001$, 0.05 μ M: $p = 0.0107$, 0.1 μ M: $p = 0.2622$, 0.2 μ M: $p = 0.0002$, and 0.5 μ M: $p < 0.0001$), a non-parametric Kruskal-Wallis test was used to test for statistically significant differences. Using a p-value of < 0.05 to determine statistical significance, it was observed that the addition of cytochalasin D significantly decreased the ‘inside-out’ forces exerted by single DBTRG-05MG cells (p-value < 0.0001). The ‘inside-out’ forces with and without the addition of 0.05 μ M, with the addition of 0.05 and 0.1 μ M, 0.2 and 0.5 μ M, and 0.1 and 0.2 μ M, and cytochalasin D were not statistically different from each other (Dunn’s multiple comparison test). However, the inside-out forces without the addition of drugs and with 0.1, 0.2 and 0.5 μ M were significantly different from each other. Also, the inside-out forces between 0.05-(0.2 & 0.5 μ M) and 0.1-0.5 μ M were significantly different (Fig. 6.6). Contractile or ‘inside-out’ forces exerted by cells are dependent on actin and myosin interactions. The disruption of either of these proteins would compromise the ability of cells to exert forces on their environment

117,193,194. While the cells exposed to 1-3 μM drug concentration did not exert measurable forces, despite the influence on cell spread area, cells that were exposed to 0.1-0.5 μM concentration of the drug were able to exert measurable nanoNewton range forces. On the other hand, cells exposed to 0.05 μM drug concentration exerted comparable ‘inside-out’ forces to those cells that were not exposed to any drugs. Our



results suggest that the time and concentration of drug exposure are two vital components in predicting single glioma cell behaviors.

Wakatsuki *et al.* have shown that exposure to minimal concentration of cytochalasin D (~20 nM)



can significantly influence the actin cytoskeleton¹⁸⁴. To examine the effect of drug concentration on cell area reduction, we selected spindle cells (cells attached to single fibers and not interacting with other fibers or cells) and measured their changing area with time for different concentrations. While spindle cells that were not exposed to cytochalasin D

maintained a relatively constant cell spread area (Fig. 6.7), those exposed to the drug shrunk, and formed spherical structures with very thin cellular projections along the nanofibers. Analysis of the change in area indicated that the addition of cytochalasin D significantly compromised the ability of DBTRG-05MG cells to spread along the nanofibers (Fig. 6.8). While the influence of 0.05 μM cytochalasin D did not show significant difference in cell spread area percentage compared to that without the drug (0 μM), the remaining concentrations tested significantly decreased cell spread area. The influence of 0.1, 0.2, and 0.5 μM cytochalasin D on cell spread area were comparable to each other, and so were those of 1, 2 and 3 μM cytochalasin D (Multiple t tests). These influences can be observed as 3 tiers of influences showing almost no influence (0.05 μM), slight influence (0.1, 0.2, and 0.5 μM), and significant influence (1, 2 and 3 μM) on decreasing cell spread area.

Cytochalasin D prevents the polymerization of actin, hence a progressive decrease in both cell spread area and force generation can be expected. Unlike in the absence of the drug, the cells under the influence of cytochalasin D were not able to return to their initial spreading area due to their inability to polymerize actin. The results however underscore that the cells on

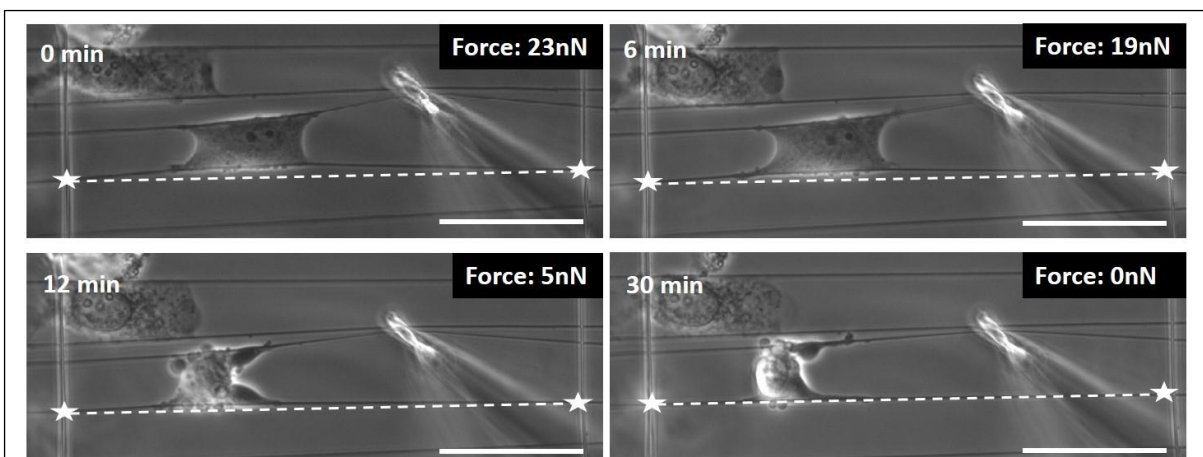


Figure 6.9. A series of time lapse images showing a single DBTRG-05MG cell exposed to 2 μM cytochalasin D being stretched by a probe. As the drug exposure time increases, the ‘outside-in’ force (shown by decreasing fiber deflection) decreases. The position of the undeflected fiber has been shown by dotted lines, the fixed points of the fiber by stars, and the respective times and forces on top left and right corners. Scale bars are 50 μm each.

suspended fibers must be exposed to concentrations comparable to 1-3 μM in order to observe significant changes in single glioma cell spreading and an absence of force generation.

Outside-in: Single DBTRG-05MG cells exposed to 0.05, 0.2 and 2 μM cytochalasin D exerted 2-57 nN ‘outside-in’ forces when subjected to cyclic strains using a micropipette manipulator (Fig. 6.9). Immediately following exposure to cytochalasin D, the spread area of the cells decreased, severely compromising the ability of cells to exert forces. Fig. 6.9 shows a progressive change in ‘outside-in’ force exerted by a single DBTRG-05MG cell as it was exposed to 2 μM cytochalasin D. This decrease in force can be observed through the decreasing deflection of the trailing fiber. Analyzing the deflection of trailing fibers, it was observed that the amount of force exerted by the cells were significantly different for the concentrations of cytochalasin D tested (Fig. 6.10, Analysis of Variance (ANOVA); p-value: 0.0005). While the outside-in forces for cells exposed to 0.05 and 0.2 μM were not significantly different from each other, those for 0.05-2 μM and 0.2-2 μM were significantly different (Tukey’s multiple comparison test). Cells exposed to 2 μM exhibited a more dramatic decrease in ‘outside-in’ forces than those exposed to 0.05 and 0.2 μM cytochalasin D (Fig. 6.10). Also, decreasing ‘outside-in’ force was more prominent when the cells were exposed to drugs for longer periods of time.

6.4 Conclusion

Cancer cells are constantly exerting and responding to mechanical forces present in their

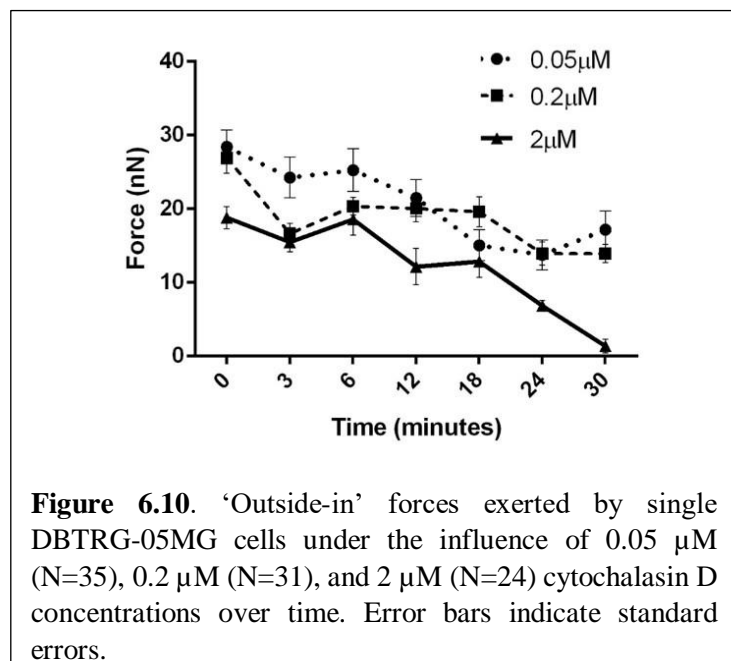


Figure 6.10. ‘Outside-in’ forces exerted by single DBTRG-05MG cells under the influence of 0.05 μM (N=35), 0.2 μM (N=31), and 2 μM (N=24) cytochalasin D concentrations over time. Error bars indicate standard errors.

immediate microenvironment. These forces have been known to influence a myriad of biochemical transduction pathways inside the cell eventually influencing the metastatic and invasive behavior of cancer cells^{168,195–197}. A better understanding of this complex two way mechanical transduction between single cancer cells and their environment can potentially contribute to our understanding of remodeling of the tumor ECM and invasion pathways.

In this study, the contribution of actin on ‘inside-out’ and ‘outside-in’ forces exerted by single DBTRG-05MG cells were assessed using suspended and aligned nanofibers that have dimensions comparable to those of the white matter tracts in the central nervous system. Our results show that when single DBTRG-05MG cells are exposed to 0.05 μM cytochalasin D, their ability to spread, exert and resist forces are comparable to those cells that have not been exposed to any drugs. Similarly, single cells exposed to 0.1-0.5 μM showed greater influences in force and spread area reduction, and those exposed to 1-3 μM concentrations exhibited the greatest influence in both spread area and force reduction. Due to severe limitations in actin polymerization, the cells exposed to 1-3 μM did not exert any forces on the nanonets after 30 minutes suggesting that cells exposed to these drug concentrations would have very limited or no ability to exert forces on their immediate ECM. Thus, the highlights of this study are fourfold: a) single cell forces were measured using a non-invasive ‘inside-out’ STEP-based platform, b) single cell responses to outside perturbations were investigated, c) suspended and aligned STEP fibers beginning to represent the white matter tracts were used, and d) a systematic demonstration of the influence of cytochalasin D concentrations on ‘inside-out’ and ‘outside-in’ cell response were investigated. The STEP nanonet platform demonstrates the capability of measuring single cell forces at the nanoNewton resolution and provides strategies to study the effect of drugs on cellular force modulation at the single cell resolution. Furthermore, the data suggests that inadequate drug concentrations and time of exposure may not fully compromise their invasive abilities or their ability to remodel their ECM potentially

resulting in undesired antidrug resistance of single cancer cells ¹⁹⁸. In future, through integration of this platform with microfluidic devices, we aim to elucidate the role of simultaneous biochemical drug and biophysical fiber cues on single cell disease models.

Chapter 7:

Collective cell migration dynamics

7.1 Introduction

Collective cell migration is vital to numerous physiological phenomenon including morphogenesis, wound healing, immune responses, vascularization of tissues and pathological conditions including cancer metastasis^{25,34,199–201}. Collective cell migration can be described as coordinated migration of multiple cells that maintain their cell-cell adhesion^{201,202}. *In vivo* collective cell migration in suspended cell bridges or sheets occurs under physiological conditions involving poorly developed or absent extra-cellular matrix (ECM). This is commonly observed in *Drosophila* gastrulation, during formation of sheets by corneal epithelium and epidermis in wound healing, and also in re-epithelialization of burn wounds on areas of absent or irregular ECM by keratinocytes^{26,203–206}. Additionally, tumors not surprisingly share remarkable similarities with a wound, including microenvironment remodeling, vascularization and cell migration^{37,207,208}. Studying collective cell migration in sheets requires development of platforms capable of capturing essential kinetics of fibrous ECM-cell interactions in single and multi-cell migration, leading to formation and advancement of cell sheets. Such platforms can not only allow faster, infection free wound healing, but also provide new knowledge in gastrulation, wound healing, metastasis, and the contributions of immune and inflammation responses after wound inducing interventions such as radiation and surgery^{209,210}.

Initiating the formation of suspended cell sheets *in vitro* is one of the major challenges in studying collective cell migration. Our current understanding of individual and collective cell migration is based on experiments involving cell depletion assays, cell exclusion assays,

polyacrylamide gels, flow chambers, glass bottom dishes, spin coated artificial extracellular matrix (ECM) films, animal and human models^{206,211–214}. In drug discovery and screening efforts, Boyden chamber assays²¹⁵ and wound-healing assays²¹⁶ are commonly used to assess the impact of drugs on 2D and 3D migration. Recently, use of non-deformable fibronectin patterned bridges with widths $> 10\mu\text{m}$ have enabled the investigation of suspended cell sheet migration dynamics^{203,217,218}. However, investigations of suspended cell sheets on fibers which mimic both native ECM fiber dimensions and layout, and which can be actively rearranged by cells, have not been performed before. Here, we utilize our previously described non-electrospinning Spinneret based Tunable Engineering Parameters (STEP)^{82,128,154,155} platform, to develop a new wound gap closure model using aligned and suspended 500 nm diameter nanofibers as pathways for cellular migration from monolayers cultured atop flat substrates placed several millimeters apart (Fig. 7.1A). Cells at the edge of the fiber-substrate interface are able to sense the fibers and initiate migration on the suspended fibers. We find that on single fibers, emergence of cells occurs in two main modes: single leaders recoiling away from monolayer or in chains of groups of few cells with intact cell-cell adhesions. On densely packed fibers, we observe emergence of multiple chains as collective groups. Advancing cells on suspended fibers form cell streams, which support formation of suspended cell sheets (SCS). We demonstrate that streams can merge through active deformation of fibers, resulting in formation of SCS with varying widths; an important consequence regulating both advancement rate and formation of gaps of varying shapes and sizes. We further demonstrate that gap closure kinetics is highly sensitive to size and shape of the gaps with gaps closing faster from regions of high curvature. Furthermore, we find that gaps with a physical width of over $375\ \mu\text{m}$ do not close over a 45 day period. The new role of suspended nanofibers in closure of gaps provides a novel outlook in design of tissue engineered scaffolds, means to study cell emergence

resembling metastasis and to interrogate cell behavior in non-closing diabetic and embryogenic gaps.

7.2 Materials and Methods

Scaffold preparation

Rectangular incisions were made into 300 μm thick plastic cover slips (Fischer Scientific, Pittsburgh, PA) to create gaps of $2 \times 3 \text{ mm}^2$. Polystyrene (PS, Scientific Polymer Products, Ontario, NY, M_w : $2 \times 10^6 \text{ g mol}^{-1}$) was dissolved in xylene (Fischer Scientific, Pittsburgh, PA) at 7% (w/w) to prepare a polymeric solution for fiber spinning. After at least 48 hours of solution preparation, the solution was extruded through a micropipette to deposit 500 nm diameter suspended and aligned fibers in parallel and crosshatch patterns using the previously described non-electrospinning STEP technique^{86,87,127,128}. The suspended fibers bridging the monolayers have diameters of approximately 500 nm and are comparable to those of collagen fibers found in the body (30 nm-20 μm)²¹⁹⁻²²¹. The diameter of the fibers were confirmed with scanning electron micrograph measurements. These scaffolds were tacked down in glass bottom six-well dishes (MatTek Corp., Ashland, MA) using high vacuum grease (Dow Corning, Midland, MI). The scaffolds were sterilized with ultraviolet rays in a sterile biosafety cabinet (1300 Series A2, Thermo Scientific, Waltham, MA) for twenty minutes before cell seeding.

Cell culture and seeding

NIH 3T3 mouse embryo fibroblasts were obtained as generous gifts from Jarvik lab, Carnegie Mellon University, Pittsburgh, PA. As recommended by the American Type Cell Culture (ATCC), these cells were grown in T25 cell culture flasks (Corning Inc., Corning, NY) with Dulbecco's Modified Eagle's Medium (DMEM, HyClone, Logan, UT) and 10% bovine calf

serum (ATCC, Manassas, VA). The cell culture was maintained at 37°C and 5% CO₂. Before seeding the cells onto the STEP fibers, the cells were suspended in cell media as follows. Media from a T25 flask containing adherent NIH3T3s was aspirated and the adherent cells were rinsed with phosphate buffered saline (PBS, Fischer Scientific, Pittsburgh, PA) twice. They were then incubated with 500 µl 0.25% Trypsin (HyClone, Logan, UT) for five minutes at 37°C and suspended in fresh cell culture media. Concentrated cell suspension was seeded on two sterile plastic platforms adjacent to the suspended STEP fibers as shown in Fig. 5.1A and the cells were allowed to attach overnight at 37°C and 5% CO₂. After cell attachment, 2 ml of cell culture media with 1% penicillin/streptomycin (HyClone, Logan, UT) was added to the well to facilitate further cell growth. The cell culture media was changed 3 times a week after rinsing the substrates with PBS.

Imaging

The scaffolds were imaged using a Zeiss microscope (Zeiss AxioObserver Z1, Jena, Germany) with incubating capacity (maintained at 37°C and 5% CO₂). Two distinct methods of imaging were used: a) phase contrast low magnification mosaic images of the scaffolds were obtained every day up to two weeks after the first cells started migrating onto the suspended nanofibers, and b) time lapse phase contrast images were obtained using 20× objective in order to investigate cell migration and local gap closure dynamics on STEP nanofibers every 3 to 10 minutes for up to 30 hour periods.

Data analysis

The mosaic images and time-lapse movies were analyzed using Zeiss Axiovision and ImageJ software. The number of scaffolds used have been denoted by N, and individual data points by n.

Global collective cell migration: In order to measure the area covered by cells on the suspended nanofibers, cell cluster areas from phase contrast images taken daily were measured using Axiovision. The summation of these cell cluster areas were then expressed as a percentage of the initial simulated gap. Cell stream separation distances were measured from the edge of one cell stream to the other using Axiovision. Similarly, the distance from the edge of the plastic platform to the closest point to the convex shaped suspended cell sheet was measured using Axiovision and described as ‘Suspended Cell Sheet (SCS) migration distance’ (Fig. 7.1B).

Local collective cell migration (local gap closure): Time lapse images were used to measure local closure of suspended gaps as a function of time using Axiovision software. Gaps were observed to be typically oval in shape and the aspect ratio of oval gap was defined as the ratio of major to minor axis (both measured using Axiovision). In order to describe the shape of the corners of the gaps, Shape Factor term defined as $SF = (Area\ of\ gap - AB/2) / (AB/2)$, where A and B are the major and minor axis, respectively (Chapter 11, Fig. 11.10). Gap areas with right angled corners (e.g. in a rectangle) would have a Shape Factor (SF) of 1, those with curved edges would have a SF of 0.57, and those with a straight line would have a SF of 0.

Analysis of the gaps that did not close: Phase contrast mosaic images of the suspended gaps were analyzed for gap closure using ImageJ software. Area and Circularity measurements were made for the gaps that closed and did not close over a period of 45 days. Also, gap area measurements were performed for about 5 consecutive days in order to assess the gap closure dynamics of gaps that did not close.

Immunostained images of suspended gaps that did not close over a period of 45 days were also analyzed for nucleus shape using ImageJ software. The perpendicular distance from the center of the nucleus to the circumference of the gap was defined as the ‘Distance from the edge’, and the Area and the Circularity of the nucleus were measured as a function of its distance from

the gap edge (Fig. 7.3D). The circularity of the nucleus was measured using ImageJ software. Circularity ($\frac{4\pi \text{ Area}}{\text{Perimeter}^2}$) is a measure describing the shape of the gap such that a perfect circle has a circularity of 1.

Immunostaining

Substrates containing SCS of NIH3T3s were stained for F-actin stress fibers and nucleus. Briefly, cell culture media was aspirated out of the well plates and the SCS were rinsed with PBS. Using a 4% paraformaldehyde in PBS solution for 15 minutes, the suspended cell sheets were fixed, and rinsed again with PBS twice. Next, the SCS were soaked in permeabilization solution (PBS with 0.1% Triton-X 100 solution) for 15 minutes, washed with PBS twice and Phalloidin (Santa Cruz Biotechnology, Santa Cruz, CA) was used at 1:80 dilution. After placing the substrates in room temperature for 40 minutes, they were rinsed with PBS three times and stained with DAPI (4', 6-diamidino-2-phenylindole) for 5 minutes. After rinsing the substrates twice, they were imaged using Zeiss AxioObserver Z1.

Drug studies

Immunostained images of gaps that did not close over a period of 45 days showed stretched nuclear morphology towards the edge of the gaps suggesting the presence of mechanical tension. Hence, we wanted to investigate the influence of a drug that has been shown to decrease tension. Y-27632 is a ROCK (Rho kinase) inhibitor that inhibits the action of myosin phosphatase. It ultimately compromises the interaction of actin and myosin light chain^{222–224}. In order to assess the influence of this drug on local gap closure and leader cell formation, SCS were exposed to 10 and 20 μM y-27632 (Sigma Aldrich, St. Louis, MO) concentrations. Its influence on local gap closure was investigated using time lapse images taken continuously over a period of up to 30 hours.

Statistical analysis

Statistical analysis of the data was conducted using GraphPad Prism (GraphPad Software, Inc., La Jolla, CA) software. In particular, D'Agostino & Pearson omnibus normality test was used to determine the normality of the data. Non-parametric Kruskal-Wallis and regression analysis were conducted. A p-value of 0.05 was used to determine statistical significance. Standard errors were calculated and represented as error bars in the respective figures.

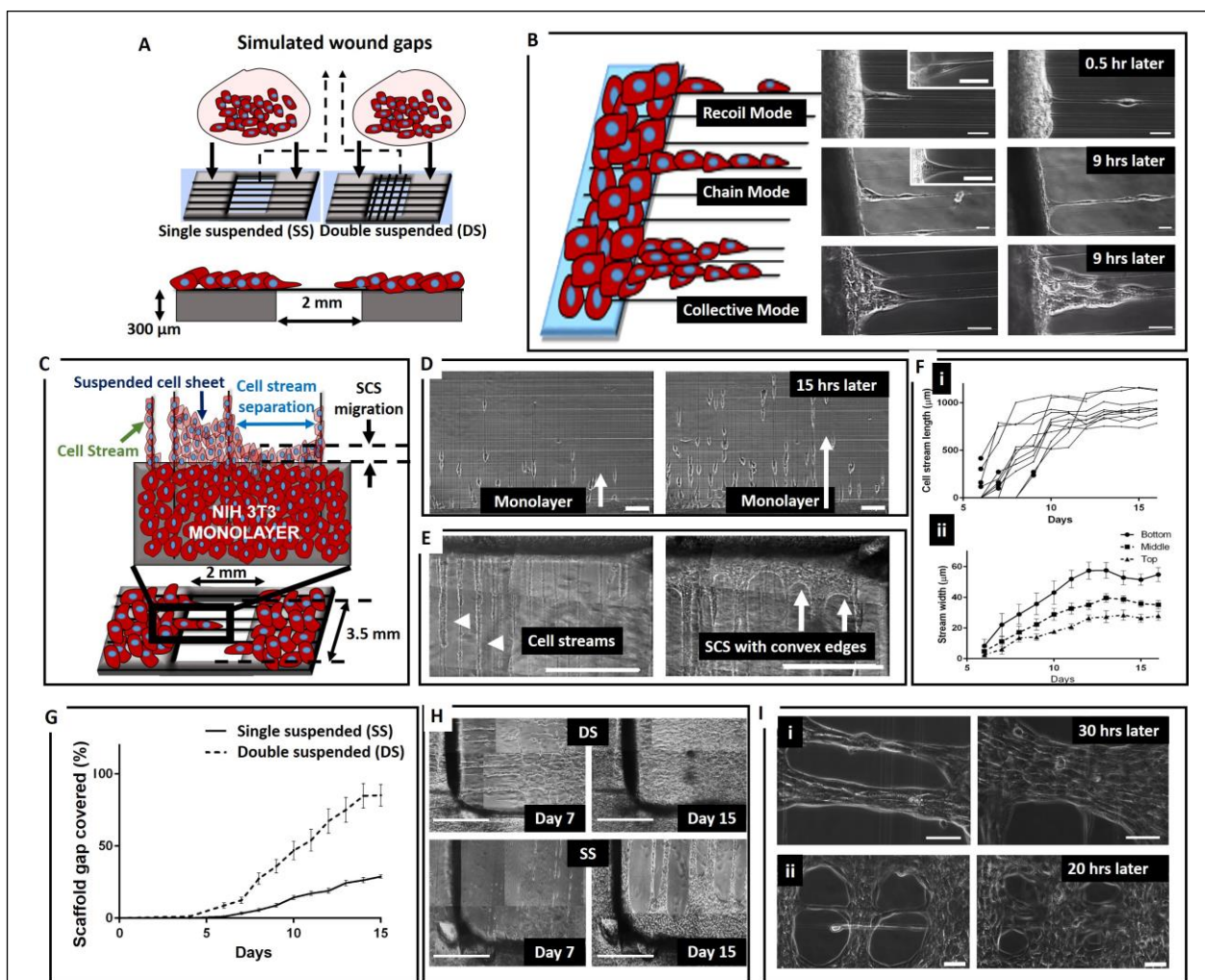


Figure 7.1. Cell emergence modes, cell stream dynamics and gap closure. (A) A schematic illustration of cell seeding, and cell stream/sheet advancement on the suspended STEP nanofibers. (B) Cells leading the monolayer exhibiting three distinct emergence modes: *single recoil leaders*, *chain* and *collective* groups. (C) Schematic illustrating cell stream and SCS. Detailed time-lapse images of (D) cells leaving monolayer, and (E) cell streams and SCS. (F) Cell stream increase in length and width over days (n=10), and black dot represents the lengths when SCS advancement reached at least 100 μ m. (G) The influence of fiber architecture on global gap closure. SS represents parallel (number of substrates, N=7), and DS (number of substrates, N=9) represents crosshatch patterned fibers. (H) Optical images of DS and SS closure over two-week period. (I) local gaps (circular (i) and oval (ii) formation (both on DS and SS, Supplementary movies 5 and 6). Scale bars are 25 μ m for B, 100 μ m for D, 500 μ m for E and H, and 50 μ m for I.

7.3 Results

Emergence of Cells and Formation of Cell Streams

Four days after seeding a concentrated suspension of NIH 3T3 fibroblasts on flat polystyrene substrates interfaced with suspended polystyrene nanofibers, confluent monolayers were formed. The cells from the confluent monolayers started sensing the nanofibers and migrated onto the suspended nanofibers (Fig. 7.1A-C). We wanted to ask how the cells emerged from the monolayers. We observed three modes of cell emergence depending upon fiber separation distance and classified the modes of emergence as *single recoil*, *chain* and *collective*. Single fibers spaced far apart facilitated *recoil* or *chain* emergence and fibers spaced densely favored *collective* emergence (Fig. 7.1 B (i-iii)). Cells emerged as *recoil* leaders primarily when the cell body was angled with the fiber axis. They underwent a conditioning phase of stretching along the fiber followed by detachment through breaking of cell-cell junctions at the rear, analogous to the recoil of a stretched rubber band. This behavior has recently been reported for metastasizing cancer cells²²⁵. Upon advancement, these cells were observed to reattach to form spindle shapes and have follower cells. In *chain* mode, cells emerged with connected followers when the cell body was symmetrically distributed around the fiber axis (Fig. 7.1 B (inset)). *Collective* emergence was predominantly found to occur in regions of densely packed fibers with multiple chains connected with each other and streaming away from the monolayer. In most cases individual cells initiated the migration process which was then followed by the emergence of cellular bundles that we termed *cell streams* (Fig. 7.1C-E). The advancing cell streams were bridged by suspended cell sheets (SCS) with distinct convex edges (Fig. 7.1E). Cells streams initially exhibited a fast emergence rate (200 $\mu\text{m}/\text{day}$), and after average of four days were observed to slow down (20 $\mu\text{m}/\text{day}$) (Fig. 7.1F (i)). Use of aligned and suspended fibers bridging monolayers cultured atop raised platforms provided well-defined geometric

environments to study single and collective cell migration. The outlined approach does not require scratching of monolayers to initiate migration, as is typically done on 2D flat substrates to obtain gaps with irregular edges. Furthermore, our method advantageously avoids interference from cellular debris and biochemical factors that are released at cell death during scratching, and are known to affect migratory behavior^{226,227}.

Gap closure is influenced by fiber network architecture, cell stream and SCS advancement dynamics

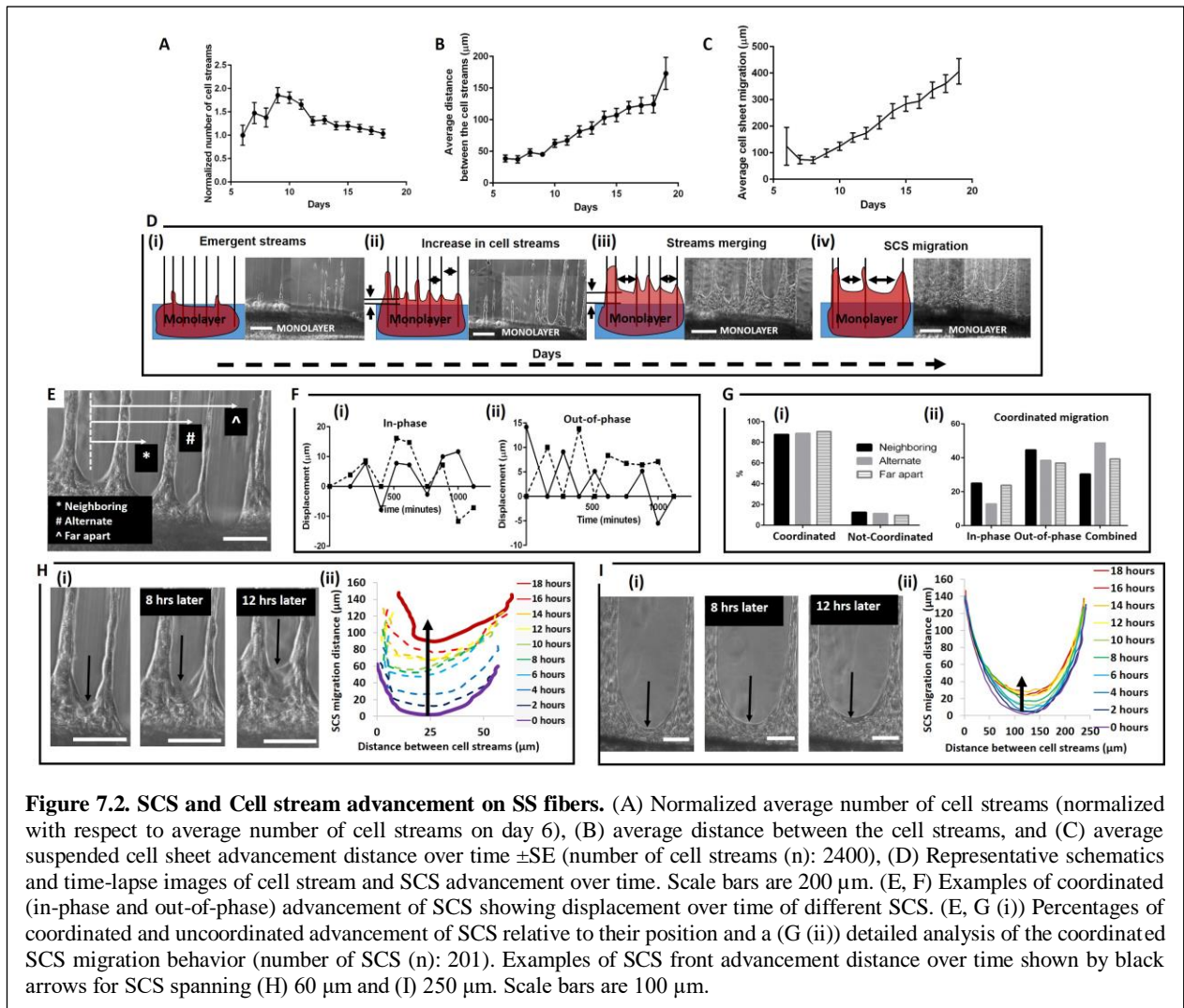
Fiber architecture: We wanted to investigate how the fiber architecture influenced cell migration. Hence, we manufactured scaffolds with two distinct fiber network architectures: single layer parallel (Single suspended, SS, N=7), and two-layer crosshatched (Double suspended, DS, N=9). While nearly entire simulated wound gaps spanned with DS fibers closed within 15 days after seeding of the fibroblast monolayer, in the same amount of time, only 30% of the gap spanned with SS fibers were closed (Fig. (7.1G, H), Chapter 11, Fig. 11.3 and 11.4). We observed the formation of oval and circular gaps on both SS and DS scaffolds, which changed their circularity over time as they closed (Fig. 7.1I). To explain the gaps that did not close, we then investigated biophysical mechanisms compromising gap closure by studying the interactions of fibers, cell streams and cell sheets over time.

Cell stream dynamics: The cell streams emerged out of the base monolayers onto the two edges of the SS substrates 6 days after seeding. Within a couple of more days, the number of cell streams emerging out of the monolayer doubled and reached a maximum (i.e. more fibers were utilized for the emergence of cell streams). In the same time period, we observed the width of the individual cell streams (measured at the base, middle and tip of streams) to increase and saturate (Fig. 7.1 F (ii)). As the cell streams advanced away from the monolayers, they were observed to merge amongst themselves causing a reduction in number of advancing cell

streams (Fig. 7.2A and D). During the merging of the cell streams, parallel fibers that were serving as the pathways for these streams also started bundling causing an increase in average gaps between the cell streams over time (Fig. 7.2B and D).

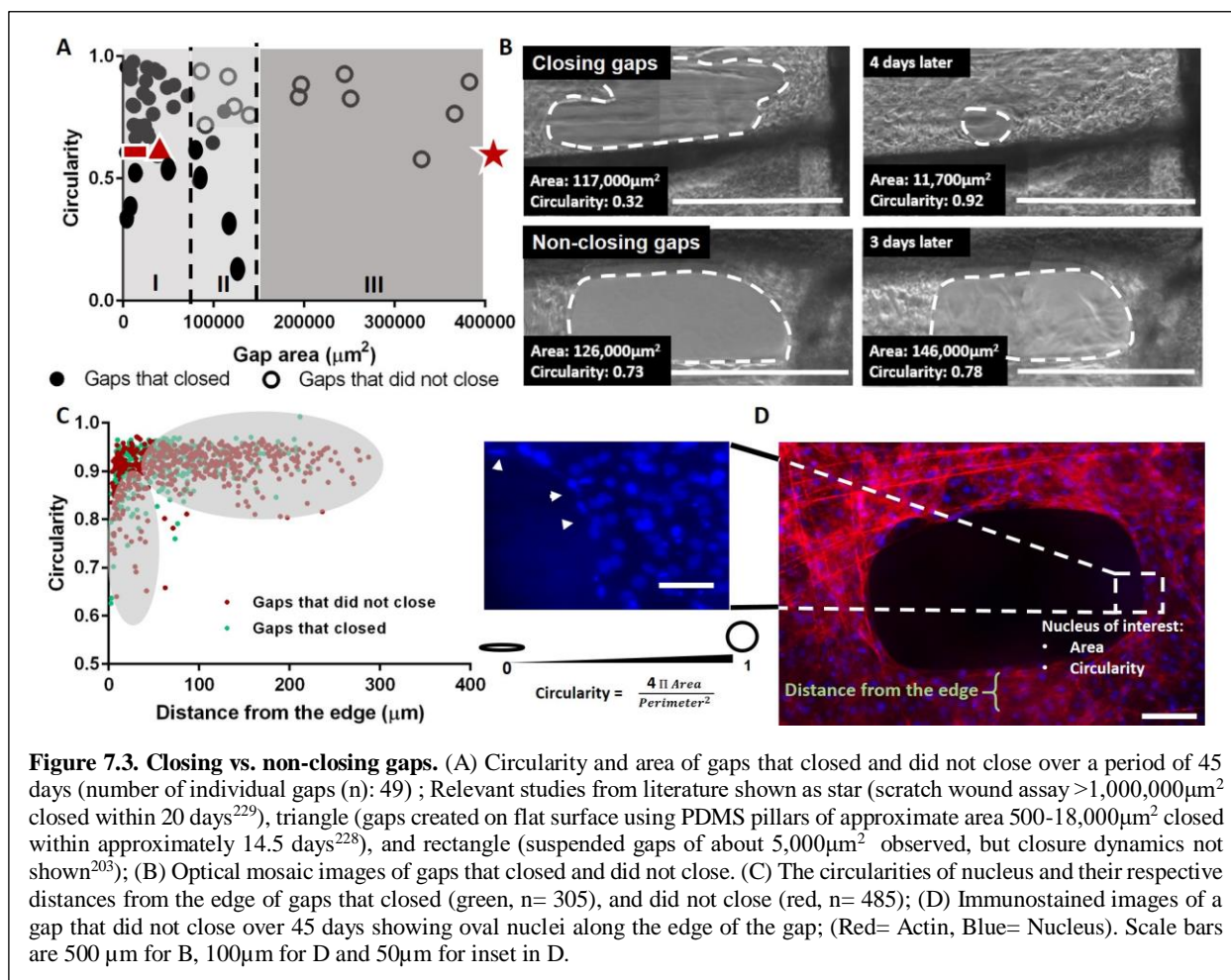
Cell stream- cell sheet dynamics: Suspended cell sheets (SCS) (Fig. 7.1E) bridging neighboring cell streams advanced away from the monolayer and contributed to closure of the gap between the monolayers on either side. As cell streams advanced away from the monolayer, the SCS distance from the base monolayer also increased (Fig. 7.2C and D). The SCS advancement distance was dependent upon its span width (i.e. separation distance between the cell streams). With merging of advancing cell streams, the SCS span width increased over time. Nonlinear regression analysis showed that lower separation widths facilitated longer SCS advancement distance, and when span width exceeded 375 μm (Chapter 11, Fig. 11.5, shown by an arrow), SCS were unable to advance forward. The inability of the SCS to advance when spanned between larger widths ultimately compromised gap closure. In a similar fashion, we found SCS speed of advancement to be compromised with increasing cell stream widths (Chapter 11, Fig. 11.5).

SCS exhibited coordinated oscillatory advancement dynamics with their neighboring, alternate, or far apart cell sheets about 90% of the cases (Fig. 7.2E-G). These coordinated modes of advancement were described as “in-phase” where two suspended sheets were moving in the same direction (forward or backward) at the same time (Fig. 7.2F (i)) or “out-of-phase” with the SCS moving in opposite directions at the same time (Fig. 7.2F (ii)). Uncoordinated advancement patterns (Chapter 11, Fig. 11.6) were also observed, but were not as common (Fig. 7.2G (i)). Further analysis of the coordinated advancement patterns showed that both out-of-phase and a combination of in-phase and out-of-phase modes (Chapter 11, Fig. 11.6) occurred 40% of the time each, and coordinated in-phase migration was observed for only about 20% of the time (Fig. 7.2G (ii)). This strongly suggests that the advancement of cell



sheets happens in an oscillatory manner, with the neighboring SCS showing a greater occurrence of out-of-phase mode. This was consistent for SCS regardless of combination of their neighboring, alternate or far apart positions including stream separation distance (Chapter 11, Fig. 11.6C).

We also investigated the shape of the advancing SCS. It was observed that SCS spanning smaller cell stream separation widths advanced away from monolayer as asymmetric high curvature convex structures (Fig. 7.2H). On the other hand, when SCS spanned larger widths, their shape remained consistently convex and symmetric (Fig. 7.2I). Next, we studied shape and size of the local gaps formed by converging of SCS from opposite sides on SS scaffolds or



by advancing cells on DS scaffolds, and investigated geometric factors contributing to gap closure dynamics.

Local gap size critically affects gap closure

Initial gap size determines gap closure: To compare gap closure with other reported methods,

we sought to determine the gap closure ability on suspended gaps of varying sizes and shapes.

We observed that local gaps were formed by cells advancing on all four intersecting fibers that formed a rectangular mesh element in DS configuration or through convergence of cell streams on SS fibers.

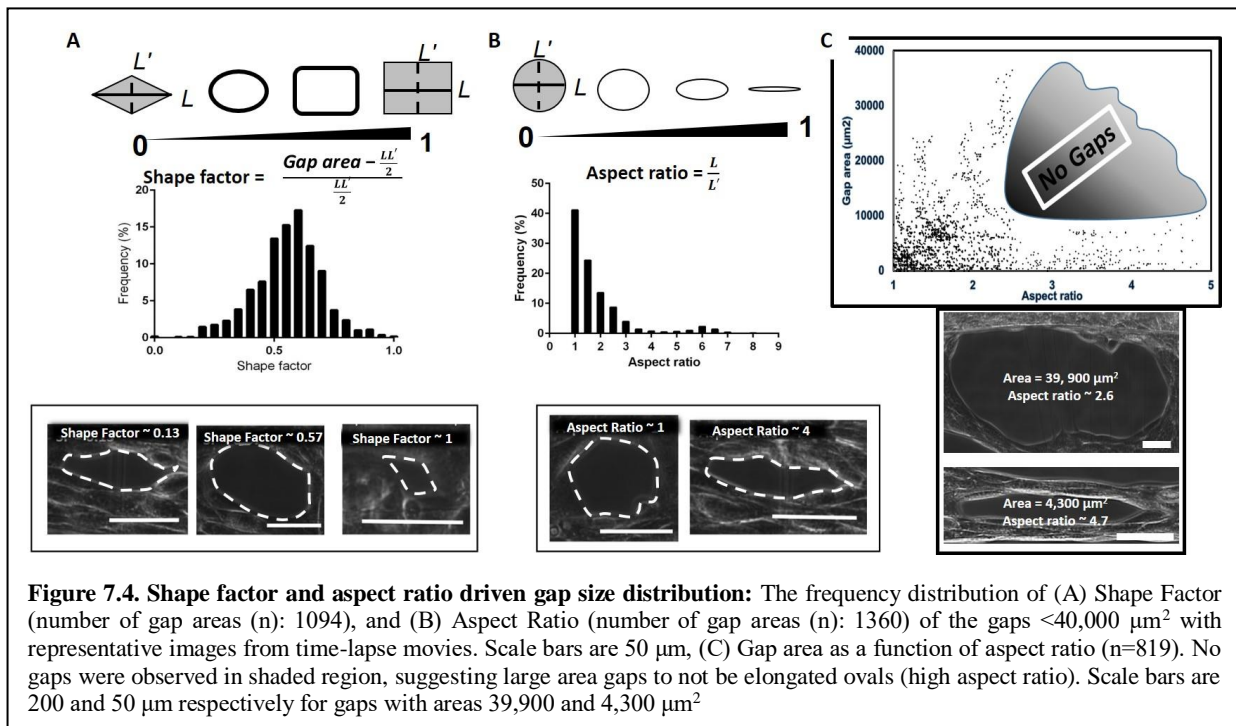
Area and circularity (defined as $\frac{4 \pi Area}{Perimeter^2}$) of gaps which closed and also of those

that did not close over a period of 45 days were measured. We observed three distinct gap size ranges that determined the ability of the gap to close over a period of 45 days (Fig. 7.3A). The

first size range (zone I) was defined by gaps of areas less than 85,000 μm². Gaps in this range

adopted a variety of shapes ranging from ovals to circles as shown by variations in circularity values. However, regardless of their circularity, these gaps were able to close completely. The second size range (zone II) was defined by gaps of areas 85,000-140,000 μm^2 . The closing of gaps in this region was dependent on their shape, with circular gaps of high circularity rarely closing and oval gaps of low circularity closing completely (Fig. 7.3B). The third size range (zone III) was defined by gaps of areas $>140,000 \mu\text{m}^2$. For this size range, regardless of the circularity, gaps were unable to close in a period of at least 45 days. In contrast, wound closure studies on 2D flat substrates of varying gap shapes and sizes (10^4 - $10^6 \mu\text{m}^2$) report significantly faster closure times (6-8 hours) and for epithelial suspended sheets having an area of 5-10,000 μm^2 in 18 hours^{203,228-230}. While these reported studies also suggest that the closure of gap is influenced by size and curvature of gaps, specific gap sizes and shapes dictating gap closure outcome have not been identified. We then examined circularity and area of cell nuclei for the cells surrounding the edge of gap. The nucleus areas were found to be similar (Chapter 11, Fig. 11.7). However, measurement of the circularity (Fig. 7.3C) showed that regardless of the ability of the gaps to close, the nucleus of the cells lining the edge of the gaps had oval shapes suggesting nuclei to be under mechanical tension (Fig. 7.3D)²³¹⁻²³⁴.

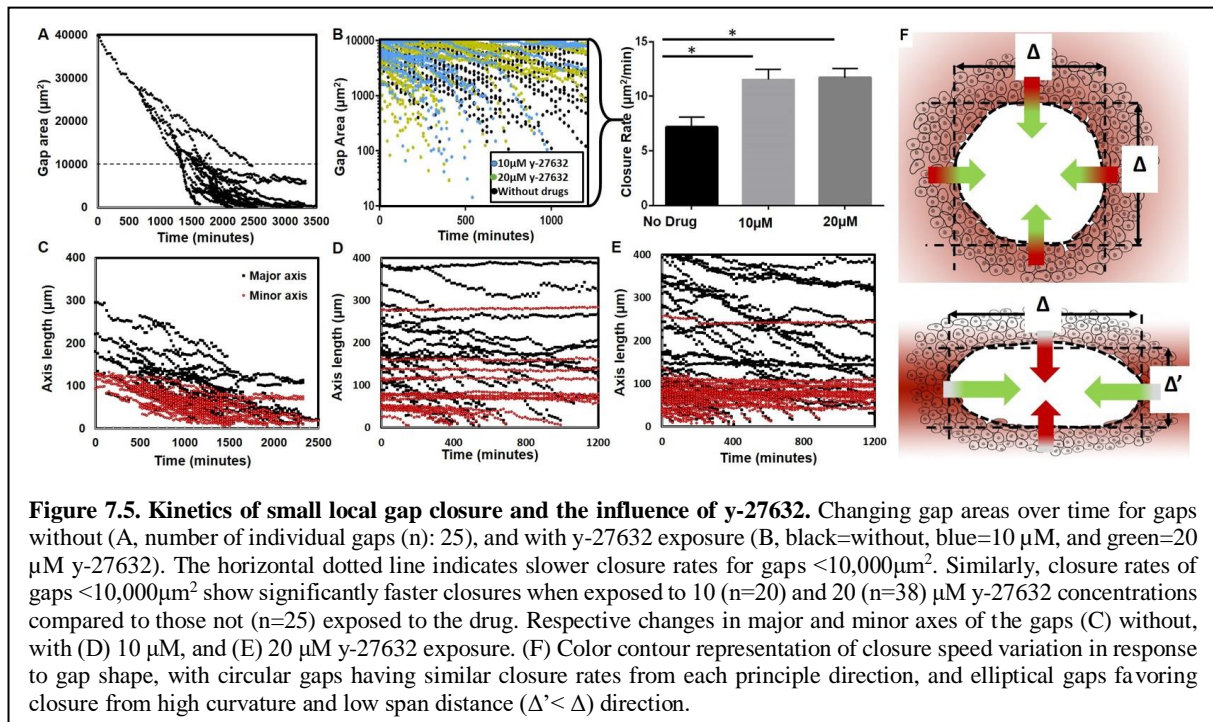
Gap shape driven closure: Next, we sought to understand the various geometrical shapes formed during closure of suspended gaps. We analyzed the shapes of gaps in zone I (completely closing) using two geometry specific metrics of Shape Factor (SF), and Aspect Ratio (AR) (Fig. 7.4). While the gaps were predominantly oval/circular, we also observed diamond and rectangular shaped gaps. The shape factor metric distinguished a diamond (SF=0), a perfect circle/ellipse (SF=0.57), or a rectangle (SF=1). In doing so, we were able to account for differences in majority of shapes, but could not distinguish between a circle and an ellipse. Probability distribution of the shape factor demonstrated that the majority of the gaps adopted



SF in the 0.57 range (Fig. 7.4A). SF distribution as a function of gap area demonstrated that larger gaps started out as circles or ovals (SF=0.57), which could also transition into rectangular and diamond shaped gaps during closure (Chapter 11, Fig. 11.8). To distinguish between circular and oval gaps, we also measured their aspect ratios (Fig. 7.4B), which showed that ~60% of gaps adopted oval and elongated morphologies with aspect ratios greater than 1. Similarly, aspect ratio distribution for varying gap sizes showed two distinct patterns shown in Fig 7.4C. While aspect ratios of larger gap sizes ranged from 1-2.5, those for smaller gaps occupied a wider range from 1-5. Importantly, gaps with aspect ratios~ 2.5-6 having areas $>\sim 10,000 \mu\text{m}^2$ were not observed. This strongly suggests that larger gap sizes are less likely to occur as elongated ovals (Aspect ratio $> \sim 2.5$).

Small local gap closure kinetics and the influence of γ -27632: Next, we wanted to investigate the closure mechanisms of small sized gaps. The temporal investigation of gap size showed that the areal closure rate ($\mu\text{m}^2/\text{min}$) of the gaps was dependent on the size of the gaps. While large gap sizes demonstrated areal closure rates of about $30 \mu\text{m}^2/\text{min}$, as time progressed and the gaps became smaller, the closure rates decreased in a non-linear fashion. Precisely, gap

closure slowed down remarkably when the gaps were smaller than 10,000 μm^2 (Fig. 7.5A). We then probed the role of acto-myosin contraction on gap closure dynamics for gaps smaller than 40,000 μm^2 . Since acto-myosin contraction is crucial for gap closure, we hypothesized that the inhibition of acto-myosin interaction would severely compromise the ability of the gaps to close. We used previously reported dosages 10 and 20 μM of Rho kinase (ROCK) inhibitor γ -27632 to compromise actin-myosin interactions^{228,235,236}. Our results show that under the influence of the drug, gap closure was significantly compromised for gaps in the range \sim 10,000-40,000 μm^2 (Kruskal-Wallis Test, $p < 0.0001$, Chapter 11, Fig. 11.9). Fig. 7.5B shows the temporal gap area measurements for gaps without (black), with 10 (blue) and 20 μM (green) γ -27632. While all the gaps were still closing in no drug condition, most gaps of sizes $> \sim$ 10,000 μm^2 did not close when exposed to γ -27632. Surprisingly, despite exposure to both concentrations of γ -27632, gaps $< \sim$ 10,000 μm^2 were able to close. In fact, the closure rate for gaps $< \sim$ 10,000 μm^2 exposed to 10 and 20 μM γ -27632 was significantly higher than those not exposed to the drug, while, there was no significant difference in gap closure rates between 10 and 20 μM γ -27632. This result is in agreement with a study by Anon *et al.*, which demonstrated that smaller circular gaps on PDMS closed in a Rho-kinase independent manner²²⁸. Closure of wounds have been associated with embryogenic and morphogenic phenomenon like palatogenesis, neural tube closure, ventral enclosure in *C. elegans*, and dorsal closure in *Drosophila*. Dorsal closure in *Drosophila* in particular is very similar to gap closure presented in our study. *Drosophila* dorsal closure has been divided into four distinct phases of initiation, epithelial sweeping, zippering and termination where the modes of closure are different. While initial gap closure is highly dependent on actin ring contraction, involvement of microtubules in forming filopodial and lamellipodial protrusions to close smaller gaps in the zippering phase have been reported^{237,238}. Since γ -27632 would not influence the microtubules, it is plausible that two different modes of closure could be contributing to local gap closure in our system



where smaller gaps close without the influence of actin-myosin contraction and is more dependent on the ability of the cells to sense each other and send out filopodial and lamellipodial protrusions to close smaller gaps.

In vitro platforms showing oval gap closures on a flat substrate show faster closure along regions of lower curvatures where cells produce lamellipodial extensions^{228,239}. Our results contradict this and demonstrate that suspended local gaps close faster in regions of higher curvature (along the major axis) (Fig. 7.5C-F). Although more subtle, this behavior was conserved when the gaps were exposed to 10 μM (Fig. 7.5D) and 20 μM (Fig. 7.5E) y-27632. These results are comparable to the SCS advancement dynamics as a function of stream separation distance demonstrated earlier (Chapter 11, Fig. 11.5A and B), suggesting that SCS advancement is exceedingly favored when SCS span widths are lower, as shown schematically in Figure 7.5F.

7.4 Discussion and Conclusion

Here we present a collective cell migration model of cell streams and suspended sheets on suspended fibers which does not involve scratching or removal of the monolayer and enables precise quantification of gap closure. Cells in the monolayer sense fibers and, depending upon the adjacent fiber separation distance, emerge in different modes: *single recoils*, *chains* or as *collective groups*. The design of fibrous scaffold layout precisely facilitated the gap closure process as cells took distinct paths along either parallel (SS) or crosshatch (DS) patterns (Chapter 11, Fig. 11.11). Emerging cells formed cell streams having an initial fast advancement rate followed by slow growth. Measurements of stream widths at the base, middle and tip of the stream length indicate streams to be conical structures with wider bases. The widths of the stream were found to increase and saturate over time, which can potentially be attributed to the formation and emergence of SCS where the cells were possibly being re-directed towards newly forming SCS. Gaps did not close completely when the span distance of SS fibers exceeded 375 μm . Hence, we suggest that there exists a critical gap size (from our network of fibers, gaps of diameters less than 375 μm (Chapter 11, Fig. 11.5)) that should be taken into consideration for the design of tissue engineering constructs for effective gap closure. As the cell streams advancing from the two monolayers converged, distinct oval structures (i.e. local gaps) formed. The ability of these gaps to close was mostly dependent on its size, and their shape. In certain cases, we observed local gaps to not close within 45 days (Fig. 7.3A). This can be explained by deconstructing the gap into four convex cell sheets (Fig. 7.5F), with each sheet having its corresponding SCS span distance (Δ or Δ'). Our previous results suggest that a span distance of 375 μm or larger significantly compromised the advancement of SCS (Chapter 11, Fig. 11.5A). If we consider the diameter of a circular gap (circularity close to 1) to be 375 μm , the gap will have an area of about 110,000 μm^2 which falls within the second region (II) (Fig. 7.3A). The SCS advancement of these gaps are highly compromised, and

hence, the gaps do not close. If the same gap area has a more oval shape (circularity <1), it will have SCS regions spanning less than $375\ \mu\text{m}$, which will contribute to closing of the gaps (Fig. 7.3B) with faster closure along the direction of the major axis. The third region (III) defined by gaps of areas $>140,000\ \mu\text{m}^2$ will always have SCS regions with span distances $>375\ \mu\text{m}$, and thus, do not close.

In conclusion, this study describes collective cell migration in a setting where the SCS are not interacting with the underlying 2D flat substrate and provides a novel perspective on gap closure that has not been presented before. In particular, our model is able to capture relevant cell-fiber interactions in distinct phases: initial emergence, collective cell migration and gap closure. We report emergence of single cells resembling release of a stretched rubber band, which allows cells to propel outwards over longer distances followed by subsequent emergence of follower cells on the same fiber. We also describe emergence of cells as chains or in collective groups of cells with intact cell-cell adhesions. Independent of emergence mode, cells advance outwards in collective setting through formation of streams and sheets. We report that SCS width is the key determinant in closure kinetics and widths of above $375\ \mu\text{m}$ severely limit the advancement of sheets and also closure of gaps. Furthermore, SCS advancement occurs via a coordinated oscillatory advancement away from the monolayer with neighboring sheets moving forward and backward simultaneously. Finally, we report that the ability of the local gaps to close depends on the size of the gaps, and in some cases, the shape of the gap (hence, by optimizing scaffold design, gaps that simulate chronic wounds could be designed *in vitro*). By being able to systematically study emergence and migration of single and collective group of cells, it is conceivable that the presented platform can serve as a foundation to generate non-closing diabetic wounds, develop cell migration efficient scaffolds for tissue engineering applications, and to study metastatic events in cancer biology.

Chapter 8: Project summary and concluding remarks

Cells are continuously interacting with their fibrous ECM in the body, and are receiving biophysical and biochemical cues. While the influence of biochemical cues has been studied relatively better, the influence of ECM biophysics is only being recognized recently. Most of the studies on how the biophysics of the ECM impacts cell behavior have probed the influence of bulk mechanical properties of substrates on cells *in vitro*. Recently, studies have highlighted that the microarchitecture and cell-fiber level biophysical properties might have a stronger influence on how cell polarization, protrusion and migration occur in physiological and diseased phenomenon like morphogenesis, wound healing, and cancer metastasis. The overarching hypothesis of this study is that metastasis occurs by a biophysical conditioning phase causing cells to become migratory leaders partly in response to biophysical cues obtained from its immediate fibrous environment. In order to investigate this, a platform that allows the manufacturing of fibrous scaffolds with highly tunable mechanical properties is required. Furthermore, the manufactured scaffolds should allow imaging at high spatiotemporal resolution, should allow the recording of dynamic cell behavior and cytoskeletal changes in response to changes in fiber properties. Therefore, previously reported non-electrospinning Spinneret based Tunable Engineered Parameters technique was used to manufacture nano-micron sized suspended fibers with user defined fiber properties like elastic modulus (N/m^2), structural stiffness (N/m), and diameter. Furthermore, these fibers were manufactured as nanonets composed of stiff and compliant fibers that defect upon being pulled by the cells allowing the measurement of nanoscale forces exerted by the cells. In order to achieve the overall goal, the study was divided into three major aspects.

Firstly, leader cell formation and detachment dynamics onto the fibers were investigated. We demonstrated that cells migrate as distinct single leaders that exhibit recoiling behavior or as a collection of cells with their cell-cell junctions intact or chain leaders. Furthermore, the

recoiling speed of the leader cells were correlated with the change in length and conditioning time during detachment suggesting that the leader cells probe their environment, utilize the energy stored as a function of their length to detach away from the monolayer in a sling shot fashion. Leader cell detachment speed and conditioning time were dependent on the diameter of the fiber with large diameter fibers (1 μ m) exhibiting high detachment speeds and low conditioning time than small diameter fibers (300nm). It was also observed that the spacing of the fiber critically affected the type of leader cell coming off of the monolayer. Furthermore, inhibition of actin-myosin interaction through 10 and 20 μ M γ -27632 significantly decreased migration speed of leader cells and compromised their ability to detach from the monolayer. The protrusion dynamics of leader cells was influenced by the curvature of the fiber, and vimentin was shown to be present in long protrusions, but deemed not necessary for the formation of one.

Through these specific aims, novel insights on how the biophysical interactions of single and collective cells with fibers influence cell dynamics like initiation of protrusion, migration, migration speed, and force exertion, collective cell migration, and gap closure can be achieved. The knowledge provided by the results obtained from these aims will be unique to what is available in literature due to the uniqueness of the STEP fiber system that allows the cells to not only interact with fiber alignment, but also the bulk mechanical property (N/m²), structural stiffness (N/m) and fiber curvature all at the same time in a suspended fiber setting. This knowledge can be utilized to understand biophysical aspects of single cell-fiber interactions that have not been investigated before. Hence, adding novel perspectives to how cell behaviors react to biophysical changes in the ECM during physiological phenomenon like wound healing, embryogenesis and cancer metastasis.

Secondly, single cell-fiber dynamics have been investigated using a glioma cell line. Glioma cells like to preferentially migrate along the white matter tracts in the central nervous system.

Hence, the fibers were manufactured to have diameters closer to those of the white matter tracts *in vivo*. Specifically, the migration, blebbing and force dynamics of cells were investigated as a function of fiber structural stiffness, cell spreading and actin polymerization inhibitor respectively. We have reported that glioma cells migrate almost three times faster on suspended nanofibers when compared to those of flat. Also, their migration speed increased with decreasing structural stiffness. We have also reported that the blebbing dynamics of glioma cells is compromised by cell spreading. Similarly, cell spread area, forces exerted by cells and their ability to withstand forces were compromised over time upon exposure to 0.05-3 μ M cytochalasin D. The results from the first specific aim highlight the importance of single cell-fiber biophysical interactions in dictating important cell behaviors.

Finally, collective cell-fiber interactions have been investigated using a novel fibroblast wound healing model. Suspended nanofibers of parallel and crisscross architecture of same diameter and elastic modulus were manufactured to bridge a gap between two fibroblast monolayers. We have reported that fiber architecture critically dictates the speed and ability of gap closure with crisscross fibers closing the gaps almost three times faster. We also observed suspended cell sheets between tightly packed cell streams migrating on the fibers. The migration of cell sheets occurred in repeatable oscillatory patterns with their span distance inversely relating to their migration speed. Upon merging of suspended cell sheets, suspended local gaps that were mostly elliptical were formed. The ability of these gaps to close was dependent on their size and in some cases, their shape. Precisely, gaps <85,000 μ m² closed regardless of shape, those >140,000 μ m² did not close regardless of shape, and those in the range 85-140,000 μ m² closed depending on their shape (while oval gaps closed, circular ones did not). Hence, by tuning the fiber manufacturing dynamics, gaps that do not close can be manufactured to potentially simulate chronic wounds like burns and diabetic ulcers *in vitro*.

Detail research objectives, hypothesis, rationale, approach, results, limitations and alternative approaches have been described below.

8.1.1 Leader cell formation and detachment dynamics

Research objective: To determine the influence of fiber properties on single cell detachment from monolayers and spheroids in order to identify fiber properties that encourage the formation of leader cells.

Hypothesis: The migratory potential of cells evading from monolayers along aligned fibers is influenced by fiber properties, thus dictating the protrusion, detachment and migration dynamics of leader cells.

Rationale: Leader cells are relevant to various physiological phenomenon including embryogenesis, morphogenesis, wound healing and diseased phenomenon like cancer metastasis. Many platforms have investigated the formation and migration dynamics of leader cells thus highlighting the biochemical triggers and associated changes in the leader cell. Most studies have identified biochemical factors that help a cell in the monolayer transform into a leader. Here, we propose that fiber properties can influence leader cell protrusion, detachment and migratory behaviors. Thus, fiber properties including spacing, curvature and diameter and their influence on the formation and detachment of leader cells were investigated.

Approach: Using the STEP platform, fibers of different diameters (200nm, 500nm, and 1 μ m) were manufactured to bridge the gap between two plastic platforms. Also, flat fibers of widths 300 and 600nm were manufactured by MicoNBase Lab and used to investigate protrusion dynamics of the cells. NIH3T3 fibroblast cells were at a high density to initiate the formation of a monolayer. Time lapse images were taken to study the cell behavior as they started protruding onto the nanofibers. The protrusion and detachment dynamics of the cells on the suspended nanofibers were recorded.

Results: Differences in fiber curvature elicited changes in protrusion dynamics. Fiber spacing dictated the ability of the cells to come out as chain or recoiling leaders. Cell detachment was dependent on parameters including change in cell length during detachment, conditioning time, and change in cell area during detachment. Cell exhibited higher detachment speeds on large diameter fibers when compared to detachment on small diameter fibers. While actin-myosin contractility was deemed important for the cells to detach as recoiling leaders, cytoskeletal protein vimentin was shown to not be necessary for cellular protrusion extension and elongation.

Limitations and Alternative Approaches: As cells are interacting with the fibers, there may be a myriad biophysical and biochemical cues that may be affecting their decision and ability to detach from the monolayer. Here, we have simplified the phenomenon and have described it using various cell morphological factors of the cell during detachment. In future, further analysis of not just cell morphological features, but also those of E-cadherin and other cytoskeletal proteins could be used to better understand the protrusive and detachment dynamics of leader cells on fibers.

8.1.2 Single cell-nanofiber interactions

Research objective: To determine the influence of fiber properties on single cell behaviors including cell migration and force generation.

Hypothesis: Cells will migrate faster on suspended nanofibers compared to a flat substrate and will respond to changes in structural stiffness (N/m).

Rationale: Cells are constantly interacting with the immediate fibrous ECM and are receiving biophysical and biochemical cues that influence cell behavior. While much of the current knowledge on the influence of environment biophysics on cell behavior stems from tuning bulk

mechanical properties of substrates, recent studies have demonstrated that single cell-fiber level interactions that include microarchitecture and single fiber properties can have a more significant impact on cell behavior. Hence, investigation of how fiber properties influence cell behavior is important to better understand physiological phenomenon including wound healing and cancer metastasis.

Approach: This aim was achieved in two parts. The first part addressed the hypothesis and investigated cell migration as a function of structural stiffness (N/m). In the second part, cell spread area and forces reaction of cells with and without the influence of actin polymerization inhibitor drug was investigated.

Using the STEP technique, mechanistically tunable polystyrene fibers of known structural stiffness were manufactured and the migration speed of a glioblastoma cell line DBTRG-05MG was investigated. Similarly, the blebbing dynamics of cells in response to cell spread area was investigated. In the second part, the STEP nanofibers were manufactured in orthogonal architecture. The orthogonal architecture comprised of highly stiff and less stiff fibers fused at the nodes forming a STEP nanonet system. As cells migrated on the fibers, the forces exerted by the cells were calculated based on measurable fiber deflections. Also, the influence of actin polymerization inhibitor drug γ -27632 on cell forces and spread area was investigated.

Results: Cell-suspended fiber interactions were fundamentally different from interactions of a cell with a flat substrate. Namely, cells wrapped around the fiber, polarized in the direction of the fiber and displayed focal adhesion clusters at the cell edges. These changes resulted in faster cell migration of cells on suspended STEP fibers. Furthermore, changing structural stiffness of the fibers elicited changes in focal adhesion patterns, ultimately influencing cell migration speed. Similarly, change in cell spread area altered actin cytoskeleton architecture and the

blebbing dynamics of cells. Also, exposure to cytochalasin D compromised cell spread area and the ability of single glioma cells to exert forces on the fibers.

Limitations and Alternative Approaches: Polystyrene is a synthetic polymer, and does not present the cells with necessary ligands for binding. Hence, ECM proteins like fibronectin or collagen could be used to coat the fibers in order to initiate cell-fiber interactions.

8.1.3 Collective cell migration dynamics

Research objective: To determine the influence of fiber architecture on collective cell migration and gap closure dynamics

Hypothesis: Suspended nanofiber architecture will affect collective cell migration of fibroblasts. In particular, crisscross patterned fibers will enhance gap closure speed.

Rationale: Collective cell migration in suspended settings are physiologically relevant to re-epithelization of wounds with absent or irregular ECM, and is poorly understood as most platforms rely on conventional flat substrates. While a recent study has shown that epithelial cells form convex suspended bridges when spanned between two PDMS pillars, a fibrous platform that recapitulates the fibrous architecture of the ECM and also investigates collective cell migration is missing. Understanding the migration dynamics of a collection of cells as they interact with fibers in a suspended setting would give us potential insights on how the biophysics of granulation tissue can facilitate wound healing, and collective migration of cancer cells during metastasis.

Approach: Using the STEP technique, polymeric fibers of parallel and crisscross architecture were manufactured to bridge a simulated gap between two plastic platforms. NIH3T3 fibroblast cells were cultured on plastic platforms interfaced with nanofibers. Time lapse images of the scaffold were taken as the cells started to migrate onto the fibers from the established monolayers. In particular, the migration dynamics of cell streams and suspended cell sheets

were investigated. Also, the gap closure dynamics of local suspended gaps were studied. Cells were also exposed to actin-myosin interaction inhibitor γ -27632 at 10 and 20 μ M concentrations in order to study the influence of actin-myosin contractility on local gap closure dynamics.

Results: Differences in suspended fiber architecture elicited different modes for collective cell migration. While cells on parallel configuration were confined to one dimensional parallel migration, those on crisscross were able to migrate on orthogonal paths that facilitated the formation of local elliptical gaps which closed over time. Local gap closure was observed to depend on the shape and size of the local gap. Also, gap closure was compromised when exposed to actin-myosin interaction inhibitor γ -27632.

Limitations and Alternative Approaches: The formation of a monolayer on the plastic platform relies on the seeding of a dense cell suspension on the plastic platform. Sometimes, cells can start migrating on the fibers before the formation of a uniform monolayer interacting with the fibers. Hence, a dense wall of fibers can be added to the edge of the plastic platform in order to ensure a full formation of the monolayer before the cells start migrating onto the fibers.

8.2 Deliverables

Overall: A comprehensive understanding of how properties of a suspended fiber influences cell behavior was achieved. Specifically, the results obtained from the aims was utilized to not only obtain a better biological understanding of how single cell-fiber level biophysics influences cell migration, force generation, blebbing dynamics, collective cell migration and leader cell detachment, but also to translate the findings to disease phenomenon like wound healing and cancer metastasis. In particular, the studies demonstrated the following:

Leader cell formation and detachment dynamics: Migration of leader cells was observed to occur in distinct single cell recoiling or collective cell chain fashion. Detachment mode was

highly dependent on the spacing of the fibers interacting with the cell monolayer. Through cellular protrusions, recoiling cells were observed to probe their environment for about two hours then detach onto the fiber by utilizing the energy stored via their cell length. The protrusion dynamics of the cells was influenced by the curvature of the fibers. Large diameter fibers (1 μ m) were better facilitators of leader cell detachment than small diameter fibers (200nm) as the cells were detaching at higher speeds on large diameter fibers. Recoiling behavior of the leader cell was severely compromised when cells were exposed to actin-myosin interaction inhibitor γ -27632. Similarly, cytoskeletal protein vimentin was shown to be present, but not necessary for protrusions.

Single cell-nanofiber interactions: For the first time, the influence of structural stiffness (N/m) on glioma cell migration was investigated to show that glioma cells migrate almost 3 times faster on suspended and aligned fibers than on conventional flat substrates. Furthermore, their migration speed was shown to increase with decreasing structural stiffness. Blebbing dynamics of glioma cells was shown to depend on the spread area of cells. Also, cells were shown to exert nN range forces as they migrated. Their ability to spread and exert force was diminished over time upon actin polymerization inhibition.

Collective cell migration dynamics: Collective cell migration of fibroblasts was shown to occur in densely packed cell streams and suspended cell sheets. Fiber architecture was shown to critically affect gap closure speed and ability with orthogonal fibers closing the gaps almost three times faster than those with parallel fibers. Migration of suspended cell sheets was shown to be a function of span distance which increased due to bundling of fibers over time. For the specific fibers used, suspended cell sheets spanning greater than a threshold distance was unable to migrate further suggesting the critical role of fiber bundling during gap closure. Contrary to what is observed in literature, the local gaps were closing faster along the major axis with high curvature. The ability of the gaps to close was shown to be dependent on size

and sometime the shape of the gap. This information could be utilized to engineer scaffolds of specific size and shape in order to create chronic wound healing models like those for burns and diabetic ulcer *in vitro*. Furthermore, it was shown that inhibition of actin-myosin interactions compromised the ability of large gaps to close, but those $<10,000\mu\text{m}^2$ closed without acto-myosin machinery.

Chapter 9: Impact and Future Directions

9.1 The bigger picture

Contribution of biophysical cues in dictating single and collective cell behavior cannot be underestimated. In the last few decades, biophysical influence of bulk mechanical properties of a substrate in cell migration, differentiation, force and intracellular tension have been well studied. However studies highlighting the importance of single cell-ECM interactions have shown that local substrate biophysics including pore size, alignment and size of the fibers might have a more influential role in cell behaviors. In this study, we utilize a previously reported non-electrospinning Spinneret based Tunable Engineered Parameters (STEP) technique to manufacture suspended and aligned fiber network with user defined mechanical properties including elastic modulus, structural stiffness and diameter in order to investigate cell behavior. Cell behavior have been investigated on three levels. First, fiber properties that tempt individual cells to detach from the monolayer and migrate onto the fibers have been investigated. Secondly, single cell-fiber interactions have been utilized to investigate its influence on cell migration, blebbing and force generation. Finally, collective cell migration has been investigated using fibers of parallel and crisscross architecture.

These findings offer a novel perspective on cell-fiber interactions than those present in literature because the unique STEP suspended fiber system allows cells to interact with the fibers on many levels. Cells are aligning the cell body along the direction of the fiber, adjusting their focal adhesion and cytoskeletal patterns, using the fibers as highways to migrate in parallel and perpendicular directions, and wrapping around the fibers simultaneously. By tuning the properties of the fibers, the effects of single and collective fiber properties can be investigated.

The results obtained from the study can be utilized to better understand myriad physiological phenomenon including morphogenesis, wound healing and cancer metastasis. In particular, the

influence of ECM biophysics, cell spread area-blebbing relationship, the efficacy of anticancer drugs in compromising cell migration forces, influence of ECM topography on single and collective cell migration could be better understood. Besides, knowledge on cell-fiber interactions could also contribute to the design of better tissue engineering scaffolds that can lead to effective treatment of chronic wounds like diabetic ulcers and burns. In future, the influence of biochemical cues can be incorporated into the study of these cell behaviors to obtain a more holistic understanding of how cell behavior is potentially controlled *in vivo* in diseased and developmental biology phenomenon.

9.2 Future Directions

Leader cell formation and detachment dynamics: Results obtained from this specific aim suggests that leader cells migrate in recoiling and non-recoiling fashion, and that the recoiling dynamics of leader cells is influenced by fiber properties. Here, the elastic modulus of the fiber is the same as all the fibers tested were polystyrene. Other polymeric materials like polyurethane can be used to investigate the influence of elastic modulus independent of fiber diameter. Similarly, the plastic platform could be coated with polyacrylamide gels of known stiffness (N/m^2) in order to assess how the base stiffness can influence the transition and initiation of leader cells. Furthermore, the leader cells can be captured via micro aspiration techniques and analyzed for up and down regulated genes using next generation gene sequencing. Also, the platform could be coupled with biochemical gradients in a microfluidic chamber in order to assess the simultaneous influence of biochemical and biophysical cues on cancer cell leader formation.

Single cell-nanofiber interactions: Results obtained from this specific aim suggests that glioma cells respond to changes in structural stiffness and show reduced blebbing dynamics when the

spread area of the cells increases. In future, fibers of different elastic modulus (polyurethane instead of polystyrene) can be utilized in order to investigate the influence of fiber curvature. Also, in order to further investigate the influence of environment on glioma migration, the fibers can be spun on plastic cover slips so that the cells are interacting with the plastic and the fibers at the same time. Similarly, other glioma cell lines can be used to investigate if the influence of fiber properties is conserved in all glioma cell types. Similarly, DBTRG-05MG cells can be exposed to cytoskeletal compromising drugs γ -27632 (actin-myosin interaction inhibitor) and cytochalasin D (actin polymerization inhibitor) in order to study the role of actin cytoskeleton on blebbing dynamics.

Similar to the study of the influence of cytochalasin D (actin polymerization inhibitor), glioma cells can be exposed to other cytoskeletal compromising drugs like nocodazole (microtubule polymerization inhibitor), γ -27632 (actin-myosin interaction inhibitor), paclitaxel (stabilizes microtubules), blebbistatin (actin-myosin interaction inhibitor), and calyculin A (increases myosin II activity) in order to systematically assess the influence of each cytoskeletal component on cell force generation and migration on suspended and aligned fibers.

Collective cell migration dynamics: Results obtained from this specific aim suggests that collective cell migration is different on parallel and crisscross patterned suspended fibers. It has also shown that gap closure dynamics depends on the shape and size of the gaps. However, in this study, only one fiber diameter was used. Hence, the experiment could be repeated with fibers of different diameters and material in order to investigate if the shape and size dependence on gap closure remains conserved.

9.3 Publications

Publications in Peer-Reviewed Journals and Books

1. P. Sharma, A. R. Kim, A. Gill, J Wang, K. Sheets, B. Behkam, A. Nain. Aligned and Suspended Fiber Force Probes for Drug Testing at Single Cell Resolution. *Biofabrication*. 2014. 6. 045006.
2. K. Sheets, P. Sharma, B. Koons, A. Nain. Cell Interactions in Wire (Fiber)-Based Structures and Scaffolds. *Handbook of Imaging in Biological Mechanics*. 2014. p. 299-311
3. P. Sharma, K. Sheets, S. Elankumaran, A Nain. The Mechanistic Influence of Aligned Nanofibers on Cell Shape, Migration and Blebbing Dynamics of Glioma Cells. *Integrative Biology*. 2013. 5 (8), p. 1036-1044
4. K. Sheets, J. Wang, S. Meehan, P. Sharma, C. Ng, M. Khan, B. Koons, B. Behkam, A. Nain. Cell-Fiber Interactions on Aligned and Suspended Nanofiber Scaffolds. *Journal of Biomaterials and Tissue Engineering*. 2013. 3 (4), p. 355-368
5. R. D. Godard, P. Sharma, C. J. Wagner, C. M. Wilson, A. Fleming-Haddock, R. L. Beach. Repeated detection of microbes in beverages dispensed from soda fountain machines and the effect of flushing on microbial density. *International Journal of Food Microbiology*. 2013. 163 (2), p. 218-222

Publication in Preparation

1. P. Sharma, C. Ng, P. Szymanski, Lee J. S. H., B. Behkam, A. Nain. Suspended and aligned fiber networks for investigation of gap closure dynamics. In Preparation.
2. B. Koons, P. Sharma, Z Ye, B. Behkam, A. S. Nain., Cancer protrusions on a tightrope- Nanofiber curvature platform reveals protrusion dynamics independent of cell migration. Manuscript Submitted.

3. P. Sharma, A. S. Nain. Leader cell formation and detachment dynamics on STEP Nanofibers. In preparation.

Abstract Presentations in Conferences

1. P. Sharma, AR Kim, A Gill, K Sheets, J Wang, B Behkam, A Nain. The influence of Cytochalasin D on inside-out glioma cell forces. *SBES Symposium Poster Presentation May 15th, 2014*
2. P. Sharma, S. Bhatia, C. Hughes, A. Nain. Cancer cell migration dynamics in mechanistically tunable fibrous scaffolds. *SBES Symposium Poster Presentation May 16th, 2013*
3. P. Sharma, K. Sheets, A. Nain. Geometry induced Altered Cytoplasmic Bleb Dynamics of GBM cells on STEP Polymeric Fibers. *GSA Symposium Oral Presentation March 28th 2012*
4. P. Sharma, K. Sheets, A Nain. Glioblastoma Dynamics in Mechanically Tunable Fibrous Scaffolds: Cytoskeleton Arrangement, Migration and Blebbing Dynamics. *SBES Symposium Poster Presentation May 11th 2012*
5. P. Sharma, S. Bhatia, C. Hughes, A. S. Nain. Prostate cancer cell migration is influenced by suspended fiber structural stiffness. *American Institute of Chemical Engineers Annual Meeting Oral Presentation November 7th, 2013*
6. B Koons, P. Sharma, A S Nain. Nanofiber based cellular protrusions of cancerous cells. *American Institute of Chemical Engineers Annual Meeting, San Francisco, California, 2013*

7. P. Sharma, S. Bhatia, C. Hughes, A. S. Nain. The influence of alignment and suspended fiber structural stiffness on cancer cell migration. *Biomedical Engineering Society (BMES) Annual Meeting, Poster Presentation September 27th, 2013*
8. E. Marquez, J. Wang, P. Sharma, A. S. Nain. Migratory Single Cell Force Measurement using STEP Nanonets. *Biomedical Engineering Society (BMES) Annual Meeting Oral Presentation October 26th, 2012*
9. P. Sharma, B. Koons, A. S. Nain. Force Measurement of Glioblastoma Multiforme (DBTRG Cells) Using STEP Nanofiber Networks. *Biomedical Engineering Society (BMES) Annual Meeting Poster Presentation October 25th, 2012*
10. S. Bhatia, P. Sharma, A. S. Nain. Effect of Curcumin on Glioma Single Cell Force Generation. *Biomedical Engineering Society (BMES) Annual Meeting. Poster Presentation. October 27th, 2012*
11. C. Hughes, P. Sharma, A. S. Nain. Fused Nanofiber Scaffolds as Force Measurement Probes for Migratory Breast Cancer Cells. *Biomedical Engineering Society (BMES) Annual Meeting. Poster Presentation October 27th, 2012*
12. T. O'Brien, K. Sheets, P. Sharma, A. S. Nain. The Application of Inverse Mathematics and Beam Theory to Determine Migratory Single Cell Forces. *Biomedical Engineering Society (BMES) Annual Meeting. Poster Presentation October 27th, 2012*
13. P. Sharma, B. Koons, T. O'Brien, A. S. Nain. Single Cell Force Measurements of Glioblastoma Multiforme Using Aligned Nanofiber Networks. *American Institute of Chemical Engineers Annual Meeting. Oral Presentation. November 2nd, 2012*
14. P. Sharma, B. Koons, A S Nain. Blebbing dynamics, single cell force measurements, and the influence of Cytochalasin D on glioblastoma multiforme cells using STEP

fibers. *2012 ASME Global Congress on Nano Engineering for Medicine and Biology. Poster Presentation. February 4-6, 2013*

15. P. Sharma, K. Sheets, A. S. Nain. The influence of polymeric fiber stiffness and alignment on cytoplasmic bleb dynamics and migration of glioblastoma multiforme cells. *ASME 2012 Summer Bioengineering Conference. Oral Presentation. June 20-23, 2012.*
16. P. Sharma, K. Sheets, A Nain. Geometry Induced Altered Cytoplasmic Bleb Dynamics of Glioblastoma Multiforme Cells on STEP Polymeric Fibers. *Annual Conference North Carolina Tissue Engineering and Regenerative Medicine Society Poster Accepted. November 4th 2011*

References

1. Engel, J. and Chiquet, M. *An Overview of Extracellular Matrix Structure and Function. Structure*, 1-39 (Springer, 2011).
2. Mecham, R. P. *Overview of extracellular matrix. Curr. Protoc. Cell Biol.*, 10.1.1-10.1.14 (John Wiley & Sons, 2001).
3. Yamada, K. M., Pankov, R. & Cukierman, E. Dimensions and dynamics in integrin function. *Braz. J. Med. Biol. Res.* **36**, 959–66 (2003).
4. Huttenlocher, A. & Horwitz, A. R. Integrins in Cell Migration. *Cold Spring Harb. Perspect. Biol.* **3**, a005074 (2011).
5. Schwartz, M. A. Integrins and extracellular matrix in mechanotransduction. *Cold Spring Harb. Perspect. Biol.* **2**, a005066 (2010).
6. Zamir, E. & Geiger, B. Molecular complexity and dynamics of cell-matrix adhesions. *J. Cell Sci.* **114**, 3583–90 (2001).
7. Lo, S. H. Focal adhesions: what's new inside. *Dev. Biol.* **294**, 280–91 (2006).
8. Schaller, M. D. Paxillin: a focal adhesion-associated adaptor protein. *Oncogene* **20**, 6459–72 (2001).
9. Paszek, M. J. *et al.* Tensional homeostasis and the malignant phenotype. *Cancer Cell* **8**, 241–54 (2005).
10. Kumar, S. & Weaver, V. M. Mechanics, malignancy, and metastasis: the force journey of a tumor cell. *Cancer Metastasis Rev.* **28**, 113–27 (2009).
11. Webster, K. D., Ng, W. P. & Fletcher, D. A. Tensional homeostasis in single fibroblasts. *Biophys. J.* **107**, 146–55 (2014).
12. Ridley, A. J. Stress fibres take shape. *Nat. Cell Biol.* **1**, E64–6 (1999).

13. Omelchenko, T., Vasiliev, J. M., Gelfand, I. M., Feder, H. H. & Bonder, E. M. Mechanisms of polarization of the shape of fibroblasts and epitheliocytes: Separation of the roles of microtubules and Rho-dependent actin-myosin contractility. *Proc. Natl. Acad. Sci. U. S. A.* **99**, 10452–7 (2002).
14. McBeath, R., Pirone, D. M., Nelson, C. M., Bhadriraju, K. & Chen, C. S. Cell shape, cytoskeletal tension, and RhoA regulate stem cell lineage commitment. *Dev. Cell* **6**, 483–95 (2004).
15. Ramachandran, C., Patil, R. V, Combrink, K., Sharif, N. A. & Srinivas, S. P. Rho-Rho kinase pathway in the actomyosin contraction and cell-matrix adhesion in immortalized human trabecular meshwork cells. *Mol. Vis.* **17**, 1877–90 (2011).
16. Engler, A. J., Sen, S., Sweeney, H. L. & Discher, D. E. Matrix elasticity directs stem cell lineage specification. *Cell* **126**, 677–89 (2006).
17. Pathak, A. & Kumar, S. Biophysical regulation of tumor cell invasion: moving beyond matrix stiffness. *Integr. Biol. (Camb)*. **3**, 267–78 (2011).
18. Meehan, S. & Nain, A. S. Role of suspended fiber structural stiffness and curvature on single-cell migration, nucleus shape, and focal-adhesion-cluster length. *Biophys. J.* **107**, 2604–2611 (2014).
19. Lo, C. M., Wang, H. B., Dembo, M. & Wang, Y. L. Cell movement is guided by the rigidity of the substrate. *Biophys. J.* **79**, 144–52 (2000).
20. Solon, J., Levental, I., Sengupta, K., Georges, P. C. & Janmey, P. A. Fibroblast adaptation and stiffness matching to soft elastic substrates. *Biophys. J.* **93**, 4453–61 (2007).
21. Ng, M. R., Besser, A., Danuser, G. & Brugge, J. S. Substrate stiffness regulates cadherin-dependent collective migration through myosin-II contractility. *J. Cell Biol.*

- 199**, 545–63 (2012).
22. Maruthamuthu, V., Sabass, B., Schwarz, U. S. & Gardel, M. L. Cell-ECM traction force modulates endogenous tension at cell-cell contacts. *Proc. Natl. Acad. Sci. U. S. A.* **108**, 4708–13 (2011).
 23. Kim, D.-H. & Wirtz, D. Focal adhesion size uniquely predicts cell migration. *FASEB J.* 1–11 (2012).
 24. Humphrey, J. D., Dufresne, E. R. & Schwartz, M. A. Mechanotransduction and extracellular matrix homeostasis. *Nat. Rev. Mol. Cell Biol.* **15**, 802–12 (2014).
 25. Iliina, O. & Friedl, P. Mechanisms of collective cell migration at a glance. *J. Cell Sci.* **122**, 3203–8 (2009).
 26. McMahon, A., Supatto, W., Fraser, S. E. & Stathopoulos, A. Dynamic analyses of *Drosophila* gastrulation provide insights into collective cell migration. *Science* **322**, 1546–50 (2008).
 27. Omelchenko, T., Vasiliev, J. M., Gelfand, I. M., Feder, H. H. & Bonder, E. M. Rho-dependent formation of epithelial ‘leader’ cells during wound healing. *Proc. Natl. Acad. Sci. U. S. A.* **100**, 10788–93 (2003).
 28. Zhang, H. *et al.* A tension-induced mechanotransduction pathway promotes epithelial morphogenesis. *Nature* **471**, 99–103 (2011).
 29. Huang, S. & Ingber, D. E. Cell tension, matrix mechanics, and cancer development. *Cancer Cell* **8**, 175–6 (2005).
 30. Mahoney, Z. X., Stappenbeck, T. S. & Miner, J. H. Laminin alpha 5 influences the architecture of the mouse small intestine mucosa. *J. Cell Sci.* **121**, 2493–502 (2008).
 31. Schedin, P. & Keely, P. J. Mammary gland ECM remodeling, stiffness, and

- mechanosignaling in normal development and tumor progression. *Cold Spring Harb. Perspect. Biol.* **3**, a003228–a003228 (2010).
32. Gilbert, T. W., Stewart-Akers, A. M., Simmons-Byrd, A. & Badylak, S. F. Degradation and remodeling of small intestinal submucosa in canine Achilles tendon repair. *J. Bone Joint Surg. Am.* **89**, 621–30 (2007).
 33. Lu, P., Takai, K., Weaver, V. M. & Werb, Z. Extracellular matrix degradation and remodeling in development and disease. *Cold Spring Harb. Perspect. Biol.* **3**, (2011).
 34. Rørth, P. Collective cell migration. *Annu. Rev. Cell Dev. Biol.* **25**, 407–29 (2009).
 35. Broughton, G., Janis, J. E. & Attinger, C. E. The basic science of wound healing. *Plast. Reconstr. Surg.* **117**, 12S–34S (2006).
 36. Martin, P. Wound healing--aiming for perfect skin regeneration. *Science* **276**, 75–81 (1997).
 37. Rybinski, B., Franco-Barraza, J. & Cukierman, E. The wound healing, chronic fibrosis, and cancer progression triad. *Physiol. Genomics* **46**, 223–44 (2014).
 38. Sandberg, M. E. C. *et al.* Change of mammographic density predicts the risk of contralateral breast cancer--a case-control study. *Breast Cancer Res.* **15**, R57 (2013).
 39. Boyd, N. F. *et al.* Mammographic densities and breast cancer risk. *Breast Dis.* **10**, 113–26 (1998).
 40. El-Serag, H. B. Hepatocellular carcinoma. *N. Engl. J. Med.* **365**, 1118–27 (2011).
 41. Plodinec, M. *et al.* The nanomechanical signature of breast cancer. *Nat. Nanotechnol.* **7**, 757–65 (2012).
 42. Provenzano, P. P. *et al.* Collagen reorganization at the tumor-stromal interface facilitates local invasion. *BMC Med.* **4**, 38 (2006).

43. Provenzano, P. P., Inman, D. R., Eliceiri, K. W., Trier, S. M. & Keely, P. J. Contact guidance mediated three-dimensional cell migration is regulated by Rho/ROCK-dependent matrix reorganization. *Biophys. J.* **95**, 5374–84 (2008).
44. Conklin, M. W. *et al.* Aligned collagen is a prognostic signature for survival in human breast carcinoma. *Am. J. Pathol.* **178**, 1221–32 (2011).
45. Riching, K. M. *et al.* 3D Collagen alignment limits protrusions to enhance breast cancer cell persistence. *Biophys. J.* **107**, 2546–58 (2014).
46. Provenzano, P. P., Eliceiri, K. W. & Keely, P. J. Multiphoton microscopy and fluorescence lifetime imaging microscopy (FLIM) to monitor metastasis and the tumor microenvironment. *Clin. Exp. Metastasis* **26**, 357–70 (2009).
47. Zhang, K. *et al.* The collagen receptor discoidin domain receptor 2 stabilizes SNAIL1 to facilitate breast cancer metastasis. *Nat. Cell Biol.* **15**, 677–87 (2013).
48. Levental, K. R. *et al.* Matrix crosslinking forces tumor progression by enhancing integrin signaling. *Cell* **139**, 891–906 (2009).
49. Maller, O., DuFort, C. C. & Weaver, V. M. YAP forces fibroblasts to feel the tension. *Nat. Cell Biol.* **15**, 570–2 (2013).
50. Carey, S. P., Kraning-Rush, C. M., Williams, R. M. & Reinhart-King, C. A. Biophysical control of invasive tumor cell behavior by extracellular matrix microarchitecture. *Biomaterials* **33**, 4157–65 (2012).
51. Tate, M. C. & Aghi, M. K. Biology of angiogenesis and invasion in glioma. *Neurotherapeutics* **6**, 447–57 (2009).
52. Zhang, F. *et al.* In vivo MRI tracking of cell invasion and migration in a rat glioma model. *Mol. Imaging Biol.* **13**, 695–701 (2011).

53. Huang, H. *et al.* Distinctive disruption patterns of white matter tracts in Alzheimer's disease with full diffusion tensor characterization. *Neurobiol. Aging* **33**, 2029–45 (2012).
54. Agudelo-Garcia, P. A. *et al.* Glioma cell migration on three-dimensional nanofiber scaffolds is regulated by substrate topography and abolished by inhibition of STAT3 signaling. *Neoplasia* **13**, 831–40 (2011).
55. Makino, M., Mimatsu, K., Saito, H., Konishi, N. & Hashizume, Y. Morphometric study of myelinated fibers in human cervical spinal cord white matter. *Spine (Phila. Pa. 1976)*. **21**, 1010–6 (1996).
56. Benninger, Y. *et al.* Beta1-integrin signaling mediates premyelinating oligodendrocyte survival but is not required for CNS myelination and remyelination. *J. Neurosci.* **26**, 7665–73 (2006).
57. Baumann, K. Switching to 3D. *Nat. Rev. Mol. Cell Biol.* **13**, 338 (2012).
58. Hostanska, K., Rostock, M., Melzer, J., Baumgartner, S. & Saller, R. A homeopathic remedy from arnica, marigold, St. John's wort and comfrey accelerates in vitro wound scratch closure of NIH 3T3 fibroblasts. *BMC Complement. Altern. Med.* **12**, 100 (2012).
59. Ashby, W. J. & Zijlstra, A. Established and novel methods of interrogating two-dimensional cell migration. *Integr. Biol. (Camb)*. **4**, 1338–50 (2012).
60. Somersalo, K., Salo, O. P., Björkstén, F. & Mustakallio, K. K. A simplified boyden chamber assay for neutrophil chemotaxis based on quantitation of myeloperoxidase. *Anal. Biochem.* **185**, 238–42 (1990).
61. Chaubey, S., Ridley, A. J. & Wells, C. M. Using the Dunn chemotaxis chamber to analyze primary cell migration in real time. *Methods Mol. Biol.* **769**, 41–51 (2011).

62. Yamaguchi, H., Pixley, F. & Condeelis, J. Invadopodia and podosomes in tumor invasion. *Eur. J. Cell Biol.* **85**, 213–8 (2006).
63. Keenan, T. M. & Folch, A. Biomolecular gradients in cell culture systems. *Lab Chip* **8**, 34–57 (2008).
64. Schoen, I., Hu, W., Klotzsch, E. & Vogel, V. Probing cellular traction forces by micropillar arrays: contribution of substrate warping to pillar deflection. *Nano Lett.* **10**, 1823–30 (2010).
65. Knoll, S. G., Ali, M. Y. & Saif, M. T. A. A novel method for localizing reporter fluorescent beads near the cell culture surface for traction force microscopy. *J. Vis. Exp.* 51873 (2014).
66. Thomas, G., Burnham, N. A., Camesano, T. A. & Wen, Q. Measuring the mechanical properties of living cells using atomic force microscopy. *J. Vis. Exp.* (2013).
67. Hochmuth, R. M. Micropipette aspiration of living cells. *J. Biomech.* **33**, 15–22 (2000).
68. Tozluoğlu, M. *et al.* Matrix geometry determines optimal cancer cell migration strategy and modulates response to interventions. *Nat. Cell Biol.* **15**, 751–62 (2013).
69. Charras, G. & Paluch, E. Blebs lead the way: how to migrate without lamellipodia. *Nat. Rev. Mol. Cell Biol.* **9**, 730–6 (2008).
70. Lee, G. Y., Kenny, P. A., Lee, E. H. & Bissell, M. J. Three-dimensional culture models of normal and malignant breast epithelial cells. *Nat. Methods* **4**, 359–65 (2007).
71. Hughes, C. S., Postovit, L. M. & Lajoie, G. A. Matrigel: a complex protein mixture required for optimal growth of cell culture. *Proteomics* **10**, 1886–90 (2010).

72. Raub, C. B. *et al.* Noninvasive assessment of collagen gel microstructure and mechanics using multiphoton microscopy. *Biophys. J.* **92**, 2212–22 (2007).
73. Tsai, J.-W. & Vallee, R. B. Live microscopy of neural stem cell migration in brain slices. *Methods Mol. Biol.* **750**, 131–42 (2011).
74. Yan, J. *et al.* Effect of fiber alignment in electrospun scaffolds on keratocytes and corneal epithelial cells behavior. *J. Biomed. Mater. Res. A* **100**, 527–35 (2012).
75. Hadjizadeh, A., Aji, A., Jolicoeur, M., Liberelle, B. & De Crescenzo, G. Effects of electrospun nanostructure versus microstructure on human aortic endothelial cell behavior. *J. Biomed. Nanotechnol.* **9**, 1195–209 (2013).
76. Jayasinghe, S. N. Cell electrospinning: a novel tool for functionalising fibres, scaffolds and membranes with living cells and other advanced materials for regenerative biology and medicine. *Analyst* **138**, 2215–23 (2013).
77. Koosha, M. & Mirzadeh, H. Electrospinning, mechanical properties, and cell behavior study of chitosan/PVA nanofibers. *J. Biomed. Mater. Res. A* (2015).
78. Wang, H. B., Mullins, M. E., Cregg, J. M., McCarthy, C. W. & Gilbert, R. J. Varying the diameter of aligned electrospun fibers alters neurite outgrowth and Schwann cell migration. *Acta Biomater.* **6**, 2970–8 (2010).
79. Binan, L. *et al.* Differentiation of neuronal stem cells into motor neurons using electrospun poly-L-lactic acid/gelatin scaffold. *Biomaterials* **35**, 664–74 (2014).
80. Nain, A. S. *et al.* Control of cell behavior by aligned micro/nanofibrous biomaterial scaffolds fabricated by spinneret-based tunable engineered parameters (STEP) technique. *Small* **4**, 1153–9 (2008).
81. Wang, J., Hou, J., Marquez, E., Moore, R. B. & Nain, A. S. Aligned assembly of nano and microscale polystyrene tubes with controlled morphology. *Polymer (Guildf)*. **55**,

- 3008–3014 (2014).
82. Nain, A. S. *et al.* Control of cell behavior by aligned micro/nanofibrous biomaterial scaffolds fabricated by spinneret-based tunable engineered parameters (STEP) technique. *Small* **4**, 1153–9 (2008).
 83. Nain, A. S., Amon, C. & Sitti, M. Proximal Probes Based Nanorobotic Drawing of Polymer Micro/Nanofibers. *IEEE Trans. Nanotechnol.* **5**, 499–510 (2006).
 84. Nain, A. S. & Wang, J. Polymeric nanofibers: isodiametric design space and methodology for depositing aligned nanofiber arrays in single and multiple layers. *Polym. J.* **45**, 695–700 (2013).
 85. Bakhru, S. *et al.* Direct and cell signaling-based, geometry-induced neuronal differentiation of neural stem cells. *Integr. Biol. (Camb)*. **3**, 1207–14 (2011).
 86. Sheets, K., Wunsch, S., Ng, C. & Nain, A. S. Shape-dependent cell migration and focal adhesion organization on suspended and aligned nanofiber scaffolds. *Acta Biomater.* **9**, 7169–77 (2013).
 87. Sharma, P., Sheets, K., Elankumaran, S. & Nain, A. S. The mechanistic influence of aligned nanofibers on cell shape, migration and blebbing dynamics of glioma cells. *Integr. Biol. (Camb)*. **5**, 1036–44 (2013).
 88. Sharma, P. *et al.* Aligned and suspended fiber force probes for drug testing at single cell resolution. *Biofabrication* **6**, 045006 (2014).
 89. Cheung, K. J., Gabrielson, E., Werb, Z. & Ewald, A. J. Collective invasion in breast cancer requires a conserved basal epithelial program. *Cell* **155**, 1639–51 (2013).
 90. Tse, J. M. *et al.* Mechanical compression drives cancer cells toward invasive phenotype. *Proc. Natl. Acad. Sci. U. S. A.* **109**, 911–6 (2012).

91. Larsen, M., Artym, V. V, Green, J. A. & Yamada, K. M. The matrix reorganized: extracellular matrix remodeling and integrin signaling. *Curr. Opin. Cell Biol.* **18**, 463–71 (2006).
92. Ewald, A. J., Brenot, A., Duong, M., Chan, B. S. & Werb, Z. Collective epithelial migration and cell rearrangements drive mammary branching morphogenesis. *Dev. Cell* **14**, 570–81 (2008).
93. Khalil, A. A. & Friedl, P. Determinants of leader cells in collective cell migration. *Integr. Biol. (Camb)*. **2**, 568–74 (2010).
94. Chapnick, D. A. & Liu, X. Leader cell positioning drives wound-directed collective migration in TGF β -stimulated epithelial sheets. *Mol. Biol. Cell* **25**, 1586–93 (2014).
95. Riahi, R. *et al.* Notch1–Dll4 signalling and mechanical force regulate leader cell formation during collective cell migration. *Nat. Commun.* **6**, 6556 (2015).
96. Grose, R. *et al.* A crucial role of beta 1 integrins for keratinocyte migration in vitro and during cutaneous wound repair. *Development* **129**, 2303–15 (2002).
97. Danjo, Y. & Gipson, I. K. Actin ‘purse string’ filaments are anchored by E-cadherin-mediated adherens junctions at the leading edge of the epithelial wound, providing coordinated cell movement. *J. Cell Sci.* **111**, 3323–32 (1998).
98. Zelenka, P. S. & Arpitha, P. Coordinating cell proliferation and migration in the lens and cornea. *Semin. Cell Dev. Biol.* **19**, 113–24 (2008).
99. Lamouille, S., Xu, J. & Derynck, R. Molecular mechanisms of epithelial-mesenchymal transition. *Nat. Rev. Mol. Cell Biol.* **15**, 178–96 (2014).
100. Oyanagi, J. *et al.* Epithelial-Mesenchymal Transition Stimulates Human Cancer Cells to Extend Microtubule-based Invasive Protrusions and Suppresses Cell Growth in Collagen Gel. *PLoS One* **7**, e53209 (2012).

101. Nguyen, B. P., Ryan, M. C., Gil, S. G. & Carter, W. G. Deposition of laminin 5 in epidermal wounds regulates integrin signaling and adhesion. *Curr. Opin. Cell Biol.* **12**, 554–62 (2000).
102. Zeisberg, M. & Neilson, E. G. Biomarkers for epithelial-mesenchymal transitions. *J. Clin. Invest.* **119**, 1429–37 (2009).
103. Sun, B. O., Fang, Y., Li, Z., Chen, Z. & Xiang, J. Role of cellular cytoskeleton in epithelial-mesenchymal transition process during cancer progression. *Biomed. reports* **3**, 603–610 (2015).
104. Trentham-Dietz, A. *et al.* Collagen fiber alignment in relation to prognostic markers for ductal carcinoma in situ of the breast. *Cancer Epidemiol. Biomarkers Prev.* **23**, 565 (2014).
105. Riching, K. M. *et al.* 3D collagen alignment limits protrusions to enhance breast cancer cell persistence. *Biophys. J.* **107**, 2546–58 (2014).
106. Grover, W. H. *et al.* Measuring single-cell density. *Proc. Natl. Acad. Sci. U. S. A.* **108**, 10992–6 (2011).
107. Friedl, P. & Alexander, S. Cancer invasion and the microenvironment: plasticity and reciprocity. *Cell* **147**, 992–1009 (2011).
108. Li, X. & Gorodeski, G. Non-muscle myosin-II-B filament regulation of paracellular resistance in cervical epithelial cells is associated with modulation of the cortical actomyosin. *J. Soc. Gynecol. Investig.* **13**, 579–91 (2006).
109. Cramer, L. P. Forming the cell rear first: breaking cell symmetry to trigger directed cell migration. *Nat. Cell Biol.* **12**, 628–32 (2010).
110. Treppe, X. *et al.* Physical forces during collective cell migration. *Nat. Phys.* **5**, 426–430 (2009).

111. Trepap, X. & Fredberg, J. J. Plithotaxis and emergent dynamics in collective cellular migration. *Trends Cell Biol.* **21**, 638–46 (2011).
112. Zeng, Q. *et al.* Endothelial cell retraction is induced by PAK2 monophosphorylation of myosin II. *J. Cell Sci.* **113**, 471–82 (2000).
113. Wysolmerski, R. B. & Lagunoff, D. Involvement of myosin light-chain kinase in endothelial cell retraction. *Proc. Natl. Acad. Sci. U. S. A.* **87**, 16–20 (1990).
114. Ishizaki, T. *et al.* Pharmacological properties of Y-27632, a specific inhibitor of rho-associated kinases. *Mol. Pharmacol.* **57**, 976–83 (2000).
115. Chernouvanenko, I. S., Minin, A. A. & Minin, A. A. Role of vimentin in cell migration. *Russ. J. Dev. Biol.* **44**, 144–157 (2013).
116. Osborn, M. & Weber, K. Tumor diagnosis by intermediate filament typing: a novel tool for surgical pathology. *Lab. Invest.* **48**, 372–94 (1983).
117. Schoumacher, M., Goldman, R. D., Louvard, D. & Vignjevic, D. M. Actin, microtubules, and vimentin intermediate filaments cooperate for elongation of invadopodia. *J. Cell Biol.* **189**, 541–56 (2010).
118. Charras, G. & Sahai, E. Physical influences of the extracellular environment on cell migration. *Nat. Rev. Mol. Cell Biol.* **15**, 813–824 (2014).
119. Guvendiren, M. & Burdick, J. A. Stiffening hydrogels to probe short- and long-term cellular responses to dynamic mechanics. *Nat. Commun.* **3**, 792 (2012).
120. Hickman, J. A. *et al.* Three-dimensional models of cancer for pharmacology and cancer cell biology: capturing tumor complexity in vitro/ex vivo. *Biotechnol. J.* **9**, 1115–28 (2014).
121. Weiswald, L.-B., Bellet, D. & Dangles-Marie, V. Spherical cancer models in tumor

- biology. *Neoplasia* **17**, 1–15 (2015).
122. Friedrich, J., Seidel, C., Ebner, R. & Kunz-Schughart, L. A. Spheroid-based drug screen: considerations and practical approach. *Nat. Protoc.* **4**, 309–24 (2009).
 123. Waleh, N. S. *et al.* Selective down-regulation of integrin receptors in spheroids of squamous cell carcinoma. *Cancer Res.* **54**, 838–43 (1994).
 124. Dangles, V. *et al.* Gene expression profiles of bladder cancers: evidence for a striking effect of in vitro cell models on gene patterns. *Br. J. Cancer* **86**, 1283–9 (2002).
 125. Vadivelu, R. K. *et al.* Generation of three-dimensional multiple spheroid model of olfactory ensheathing cells using floating liquid marbles. *Sci. Rep.* **5**, 15083 (2015).
 126. Chen, Y.-C. *et al.* High-Throughput Cancer Cell Sphere Formation for Characterizing the Efficacy of Photo Dynamic Therapy in 3D Cell Cultures. *Sci. Rep.* **5**, 12175 (2015).
 127. Wang, J. & Nain, A. S. Suspended Micro/Nanofiber Hierarchical Biological Scaffolds Fabricated using Non-Electrospinning STEP Technique. *Langmuir* **30**, 13641–13649 (2014).
 128. Nain, A. S., Sitti, M., Jacobson, A., Kowalewski, T. & Amon, C. Dry spinning based spinneret based tunable engineered parameters (STEP) technique for controlled and aligned deposition of polymeric nanofibers. *Macromol. Rapid Commun.* **30**, 1406–12 (2009).
 129. Salmenperä, P. *et al.* Formation and activation of fibroblast spheroids depend on fibronectin-integrin interaction. *Exp. Cell Res.* **314**, 3444–52 (2008).
 130. Society, A. C. *Cancer Facts and Figures 2010*. (2010).
 131. Holland, E. C. Glioblastoma multiforme: the terminator. *Proc. Natl. Acad. Sci. U. S. A.*

- 97**, 6242–4 (2000).
132. Louis, D. N. *et al.* The 2007 WHO classification of tumours of the central nervous system. *Acta Neuropathol.* **114**, 97–109 (2007).
 133. *Central Brain Tumor Registry of the United States Statistical Report.* (2002).
 134. Nakada, M. *et al.* Aberrant signaling pathways in glioma. *Cancers (Basel)*. **3**, 3242–78 (2011).
 135. Ulrich, T. a, de Juan Pardo, E. M. & Kumar, S. The mechanical rigidity of the extracellular matrix regulates the structure, motility, and proliferation of glioma cells. *Cancer Res.* **69**, 4167–74 (2009).
 136. Mehlen, P. & Puisieux, A. Metastasis: a question of life or death. *Nat. Rev. Cancer* **6**, 449–58 (2006).
 137. Hanahan, D. & Weinberg, R. A. Hallmarks of cancer: the next generation. *Cell* **144**, 646–74 (2011).
 138. Sykova, E. *The Neuronal Environment Brain Homeostasis in Health and Disease.* (2002).
 139. Swaminathan, V. *et al.* Mechanical stiffness grades metastatic potential in patient tumor cells and in cancer cell lines. *Cancer Res.* **71**, 5075–80 (2011).
 140. Schrader, J. *et al.* Matrix stiffness modulates proliferation, chemotherapeutic response, and dormancy in hepatocellular carcinoma cells. *Hepatology* **53**, 1192–205 (2011).
 141. Yeung, T. *et al.* Effects of substrate stiffness on cell morphology, cytoskeletal structure, and adhesion. *Cell Motil. Cytoskeleton* **60**, 24–34 (2005).
 142. Ng, M. R. & Brugge, J. S. A stiff blow from the stroma: collagen crosslinking drives tumor progression. *Cancer Cell* **16**, 455–7 (2009).

143. Johnson, J. *et al.* Quantitative analysis of complex glioma cell migration on electrospun polycaprolactone using time-lapse microscopy. *Tissue Eng. Part C. Methods* **15**, 531–40 (2009).
144. Caspani, E. M., Echevarria, D., Rottner, K. & Small, J. V. Live imaging of glioblastoma cells in brain tissue shows requirement of actin bundles for migration. *Neuron Glia Biol.* **2**, 105–14 (2006).
145. Babiychuk, E. B., Monastyrskaya, K., Potez, S. & Draeger, a. Blebbing confers resistance against cell lysis. *Cell Death Differ.* **18**, 80–9 (2011).
146. Fackler, O. T. & Grosse, R. Cell motility through plasma membrane blebbing. *J. Cell Biol.* **181**, 879–84 (2008).
147. Shea, K. F., Wells, C. M., Garner, A. P. & Jones, G. E. ROCK1 and LIMK2 interact in spread but not blebbing cancer cells. *PLoS One* **3**, e3398 (2008).
148. Charras, G. T. A short history of blebbing. *J. Microsc.* **231**, 466–78 (2008).
149. Ridley, A. Blebbing: motility research moves in a new direction. *Nat. Rev. Mol. Cell Biol.* **10**, 164–164 (2009).
150. Blaser, H. *et al.* Migration of zebrafish primordial germ cells: a role for myosin contraction and cytoplasmic flow. *Dev. Cell* **11**, 613–27 (2006).
151. Gong, J. *et al.* Microparticles and their emerging role in cancer multidrug resistance. *Cancer Treat. Rev.* **38**, 226–34 (2012).
152. Gisselsson, D. *et al.* Abnormal Nuclear Shape in Solid Tumors Reflects Mitotic Instability. *Am. J. Pathol.* **158**, 199–206 (2001).
153. Di Vizio, D. *et al.* Oncosome formation in prostate cancer: association with a region of frequent chromosomal deletion in metastatic disease. *Cancer Res.* **69**, 5601–9 (2009).

154. Nain, A. S., Wong, J. C., Amon, C. & Sitti, M. Drawing suspended polymer micro/nanofibers using glass micropipettes. *Appl. Phys. Lett.* **89**, 183105 (2006).
155. Nain, A. S., Amon, C. & Sitti, M. Proximal probes based nanorobotic drawing of polymer micro/nanofibers. *IEEE Trans. Nanotechnol.* **5**, 499–510 (2006).
156. Chuang, J., Anderson, M., Wu, K and Hsieh, S. *Nanomechanics of Materials and Structures*, 13-22 (Springer-Verlag, 2006).
157. Tan, E. P. S. & Lim, C. T. Effects of annealing on the structural and mechanical properties of electrospun polymeric nanofibres. *Nanotechnology* **17**, 2649–54 (2006).
158. Baker, E. L., Bonnecaze, R. T. & Zaman, M. H. Extracellular matrix stiffness and architecture govern intracellular rheology in cancer. *Biophys. J.* **97**, 1013–21 (2009).
159. Giese, A., Loo, M. A., Rief, M. D., Tran, N. & Berens, M. E. Substrates for astrocytoma invasion. *Neurosurgery* **37**, 294–301; discussion 301–2 (1995).
160. McDonough, W., Tran, N., Giese, A., Norman, S. A. & Berens, M. E. Altered gene expression in human astrocytoma cells selected for migration: I. Thromboxane synthase. *J. Neuropathol. Exp. Neurol.* **57**, 449–55 (1998).
161. Romano, A., Scheel, M., Hirsch, S., Braun, J. & Sack, I. In vivo waveguide elastography of white matter tracts in the human brain. *Magn. Reson. Med.* **68**, 1410–22 (2012).
162. Charras, G. T., Hu, C.-K., Coughlin, M. & Mitchison, T. J. Reassembly of contractile actin cortex in cell blebs. *J. Cell Biol.* **175**, 477–90 (2006).
163. Tumminia, S. J. *et al.* Mechanical stretch alters the actin cytoskeletal network and signal transduction in human trabecular meshwork cells. *Invest. Ophthalmol. Vis. Sci.* **39**, 1361–71 (1998).

164. Tysnes, B. B. & Mahesparan, R. Biological mechanisms of glioma invasion and potential therapeutic targets. *J. Neurooncol.* **53**, 129–47 (2001).
165. Mariani, L. *et al.* Glioma cell motility is associated with reduced transcription of proapoptotic and proliferation genes: a cDNA microarray analysis. *J. Neurooncol.* **53**, 161–76 (2001).
166. Farwell, L. M. & Joshi, V. A. DNA sequencing of cancer-related genes for biomarker discovery. *Methods Mol. Biol.* **520**, 205–20 (2009).
167. Suresh, S. Biomechanics and biophysics of cancer cells☆. *Acta Mater.* **55**, 3989–4014 (2007).
168. Mierke, C. T., Bretz, N. & Altevogt, P. Contractile forces contribute to increased glycosylphosphatidylinositol-anchored receptor CD24-facilitated cancer cell invasion. *J. Biol. Chem.* **286**, 34858–71 (2011).
169. Lekka, M. *et al.* Cancer cell detection in tissue sections using AFM. *Arch. Biochem. Biophys.* **518**, 151–6 (2012).
170. Shin, D. & Athanasiou, K. Cytoindentation for obtaining cell biomechanical properties. *J. Orthop. Res.* **17**, 880–90 (1999).
171. Guck, J. *et al.* Optical deformability as an inherent cell marker for testing malignant transformation and metastatic competence. *Biophys. J.* **88**, 3689–98 (2005).
172. Guo, Q., Park, S. & Ma, H. Microfluidic micropipette aspiration for measuring the deformability of single cells. *Lab Chip* **12**, 2687–95 (2012).
173. Shieh, A. C. & Swartz, M. A. Regulation of tumor invasion by interstitial fluid flow. *Phys. Biol.* **8**, 015012 (2011).
174. Viator, J. A. *et al.* Gold nanoparticle mediated detection of prostate cancer cells using

- photoacoustic flowmetry with optical reflectance. *J. Biomed. Nanotechnol.* **6**, 187–91 (2010).
175. Powers, A. D., Liu, B., Lee, A. G. & Palecek, S. P. Macroporous hydrogel micropillars for quantifying Met kinase activity in cancer cell lysates. *Analyst* **137**, 4052–61 (2012).
176. Peschetola, V. *et al.* Time-dependent traction force microscopy for cancer cells as a measure of invasiveness. *Cytoskeleton (Hoboken)*. **70**, 201–14 (2013).
177. Burton, K. & Taylor, D. L. Traction forces of cytokinesis measured with optically modified elastic substrata. *Nature* **385**, 450–4 (1997).
178. Chen, J. Nanobiomechanics of living cells: a review. *Interface Focus* **4**, 20130055–20130055 (2014).
179. Rodriguez, M. L., McGarry, P. J. & Sniadecki, N. J. Review on Cell Mechanics: Experimental and Modeling Approaches. *Appl. Mech. Rev.* **65**, 060801 (2013).
180. Discher, D. E., Janmey, P. & Wang, Y.-L. Tissue cells feel and respond to the stiffness of their substrate. *Science* **310**, 1139–43 (2005).
181. Pelham, R. J. & Wang, Y. L. Cell locomotion and focal adhesions are regulated by the mechanical properties of the substrate. *Biol. Bull.* **194**, 348–9 (1998).
182. Wang, Y., Wang, G., Luo, X., Qiu, J. & Tang, C. Substrate stiffness regulates the proliferation, migration, and differentiation of epidermal cells. *Burns* **38**, 414–20 (2012).
183. Sheets, K. *et al.* Cell-Fiber Interactions on Aligned and Suspended Nanofiber Scaffolds. *J. Biomater. Tissue Eng.* **3**, 355–368 (2013).
184. Wakatsuki, T., Schwab, B., Thompson, N. C. & Elson, E. L. Effects of cytochalasin D and latrunculin B on mechanical properties of cells. *J. Cell Sci.* **114**, 1025–36 (2001).

185. Casella, J. F., Flanagan, M. D. & Lin, S. Cytochalasin D inhibits actin polymerization and induces depolymerization of actin filaments formed during platelet shape change. *Nature* **293**, 302–305 (1981).
186. Burridge, K. & Wittchen, E. S. The tension mounts: stress fibers as force-generating mechanotransducers. *J. Cell Biol.* **200**, 9–19 (2013).
187. Romet-Lemonne, G. & Jégou, A. Mechanotransduction down to individual actin filaments. *Eur. J. Cell Biol.* **92**, 333–8
188. Timoshenko, S. *Strength of Materials*. 66-74 (Robert E Krieger Publishing Company, 1983).
189. Gestos, A., Whitten, P. G., Spinks, G. M. & Wallace, G. G. Tensile testing of individual glassy, rubbery and hydrogel electrospun polymer nanofibres to high strain using the atomic force microscope. *Polym. Test.* **32**, 655–664 (2013).
190. Carlisle, C. R., Coulais, C. & Guthold, M. The mechanical stress-strain properties of single electrospun collagen type I nanofibers. *Acta Biomater.* **6**, 2997–3003 (2010).
191. Hibbeler, R. C. *Statics and Mechanics of Materials*. 501-550 (Pearson, 2011).
192. Cuenot, S., Frétiigny, C., Demoustier-Champagne, S. & Nysten, B. Surface tension effect on the mechanical properties of nanomaterials measured by atomic force microscopy. *Phys. Rev. B* **69**, 165410 (2004).
193. Olson, M. F. & Sahai, E. The actin cytoskeleton in cancer cell motility. *Clin. Exp. Metastasis* **26**, 273–87 (2009).
194. Torgerson, R. R. & McNiven, M. a. The actin-myosin cytoskeleton mediates reversible agonist-induced membrane blebbing. *J. Cell Sci.* **111**, 2911–22 (1998).
195. Koch, T. M., Münster, S., Bonakdar, N., Butler, J. P. & Fabry, B. 3D Traction forces

- in cancer cell invasion. *PLoS One* **7**, e33476 (2012).
196. Mierke, C. T., Frey, B., Fellner, M., Herrmann, M. & Fabry, B. Integrin $\alpha 5\beta 1$ facilitates cancer cell invasion through enhanced contractile forces. *J. Cell Sci.* **124**, 369–83 (2011).
 197. Mierke, C. T., Rösel, D., Fabry, B. & Brábek, J. Contractile forces in tumor cell migration. *Eur. J. Cell Biol.* **87**, 669–76 (2008).
 198. De Souza, R., Zahedi, P., Badame, R. M., Allen, C. & Piquette-Miller, M. Chemotherapy dosing schedule influences drug resistance development in ovarian cancer. *Mol. Cancer Ther.* **10**, 1289–99 (2011).
 199. Aman, A. & Piotrowski, T. Cell migration during morphogenesis. *Dev. Biol.* **341**, 20–33 (2010).
 200. Deisboeck, T. S. & Couzin, I. D. Collective behavior in cancer cell populations. *Bioessays* **31**, 190–7 (2009).
 201. Friedl, P. & Gilmour, D. Collective cell migration in morphogenesis, regeneration and cancer. *Nat. Rev. Mol. Cell Biol.* **10**, 445–57 (2009).
 202. Haeger, A., Wolf, K., Zegers, M. M. & Friedl, P. Collective cell migration: guidance principles and hierarchies. *Trends Cell Biol.* (2015).
 203. Vedula, S. R. K. *et al.* Epithelial bridges maintain tissue integrity during collective cell migration. *Nat. Mater.* **13**, 87–96 (2014).
 204. Weiss, P. & Matoltsy, A. G. Wound healing in chick embryos in vivo and in vitro. *Dev. Biol.* **1**, 302–326 (1959).
 205. Oskeritzian, C. A. Mast Cells and Wound Healing. *Adv. wound care* **1**, 23–28 (2012).
 206. Vedula, S. R. K., Ravasio, A., Lim, C. T. & Ladoux, B. Collective cell migration: a

- mechanistic perspective. *Physiology (Bethesda)*. **28**, 370–9 (2013).
207. Schäfer, M. & Werner, S. Cancer as an overhealing wound: an old hypothesis revisited. *Nat. Rev. Mol. Cell Biol.* **9**, 628–38 (2008).
208. Arwert, E. N., Hoste, E. & Watt, F. M. Epithelial stem cells, wound healing and cancer. *Nat. Rev. Cancer* **12**, 170–80 (2012).
209. Schaeue, D. & McBride, W. H. Opportunities and challenges of radiotherapy for treating cancer. *Nat. Rev. Clin. Oncol.* **12**, 527–540 (2015).
210. Wyld, L., Audisio, R. A. & Poston, G. J. The evolution of cancer surgery and future perspectives. *Nat. Rev. Clin. Oncol.* **12**, 115–24 (2015).
211. Kaur, H., Heeney, R., Carriveau, R., Sosne, G. & Mutus, B. Whole blood, flow-chamber studies in real-time indicate a biphasic role for thymosin β -4 in platelet adhesion. *Biochim. Biophys. Acta* **1800**, 1256–61 (2010).
212. Fong, E., Tzlil, S. & Tirrell, D. A. Boundary crossing in epithelial wound healing. *Proc. Natl. Acad. Sci. U. S. A.* **107**, 19302–7 (2010).
213. Keane, F. M. *et al.* Quantitation of fibroblast activation protein (FAP)-specific protease activity in mouse, baboon and human fluids and organs. *FEBS Open Bio* **4**, 43–54 (2013).
214. Sullivan, T. P., Eaglstein, W. H., Davis, S. C. & Mertz, P. The pig as a model for human wound healing. *Wound Repair Regen.* **9**, 66–76
215. BOYDEN, S. The chemotactic effect of mixtures of antibody and antigen on polymorphonuclear leucocytes. *J. Exp. Med.* **115**, 453–66 (1962).
216. Todaro, G. J., Lazar, G. K. & Green, H. The initiation of cell division in a contact-inhibited mammalian cell line. *J. Cell. Comp. Physiol.* **66**, 325–333 (1965).

217. Brugués, A. *et al.* Forces driving epithelial wound healing. *Nat. Phys.* **10**, 683–690 (2014).
218. Vedula, S. R. K. *et al.* Emerging modes of collective cell migration induced by geometrical constraints. *Proc. Natl. Acad. Sci. U. S. A.* **109**, 12974–9 (2012).
219. Berkovitz, B. K., Weaver, M. E., Shore, R. C. & Moxham, B. J. Fibril diameters in the extracellular matrix of the periodontal connective tissues of the rat. *Connect. Tissue Res.* **8**, 127–32 (1981).
220. Kolt, G and Snyder-Mackler. *Physical Therapies in Sport and Exercise*. Chapter 2, (Elsevier Health Sciences, 2007).
221. Ushiki, T. Collagen fibers, reticular fibers and elastic fibers. A comprehensive understanding from a morphological viewpoint. *Arch. Histol. Cytol.* **65**, 109–26 (2002).
222. Vicente-Manzanares, M., Ma, X., Adelstein, R. S. & Horwitz, A. R. Non-muscle myosin II takes centre stage in cell adhesion and migration. *Nat. Rev. Mol. Cell Biol.* **10**, 778–90 (2009).
223. Totsukawa, G. *et al.* Distinct roles of ROCK (Rho-kinase) and MLCK in spatial regulation of MLC phosphorylation for assembly of stress fibers and focal adhesions in 3T3 fibroblasts. *J. Cell Biol.* **150**, 797–806 (2000).
224. Sakamoto, K. *et al.* Inhibition of high K⁺-induced contraction by the ROCKs inhibitor Y-27632 in vascular smooth muscle: possible involvement of ROCKs in a signal transduction pathway. *J. Pharmacol. Sci.* **92**, 56–69 (2003).
225. Weigelin, B., Bakker, G.-J. & Friedl, P. Intravital third harmonic generation microscopy of collective melanoma cell invasion. *IntraVital* **1**, 32–43 (2014).
226. Block, E. R., Matela, A. R., SundarRaj, N., Iszkula, E. R. & Klarlund, J. K. Wounding

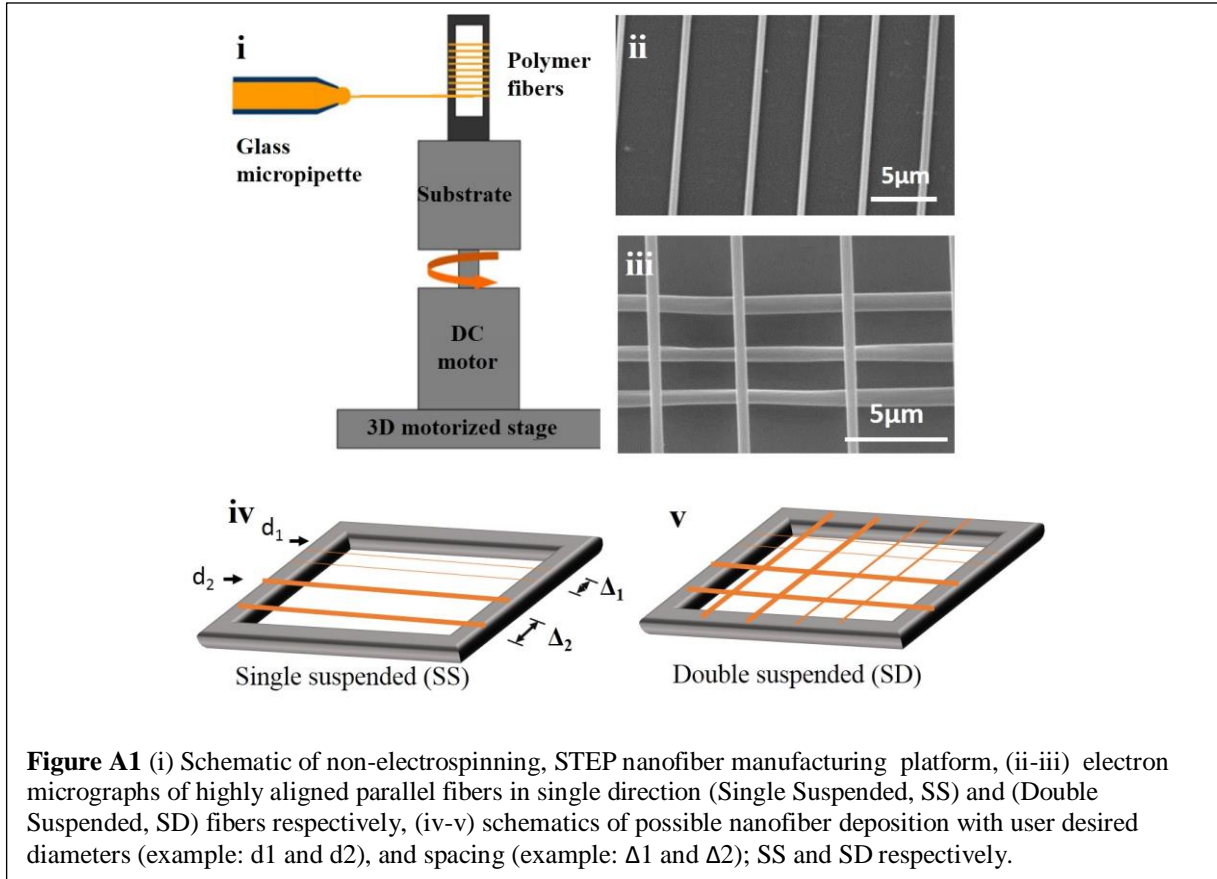
- induces motility in sheets of corneal epithelial cells through loss of spatial constraints: role of heparin-binding epidermal growth factor-like growth factor signaling. *J. Biol. Chem.* **279**, 24307–12 (2004).
227. Klepeis, V. E., Cornell-Bell, A. & Trinkaus-Randall, V. Growth factors but not gap junctions play a role in injury-induced Ca²⁺ waves in epithelial cells. *J. Cell Sci.* **114**, 4185–95 (2001).
228. Anon, E. *et al.* Cell crawling mediates collective cell migration to close undamaged epithelial gaps. *Proc. Natl. Acad. Sci. U. S. A.* **109**, 10891–6 (2012).
229. Lu, K. V, Jong, K. A., Rajasekaran, A. K., Cloughesy, T. F. & Mischel, P. S. Upregulation of tissue inhibitor of metalloproteinases (TIMP)-2 promotes matrix metalloproteinase (MMP)-2 activation and cell invasion in a human glioblastoma cell line. *Lab. Investig.* **84**, 8–20 (2003).
230. Vedula, S. R. K. *et al.* Mechanics of epithelial closure over non-adherent environments. *Nat. Commun.* **6**, 6111 (2015).
231. Versaevel, M., Grevesse, T. & Gabriele, S. Spatial coordination between cell and nuclear shape within micropatterned endothelial cells. *Nat. Commun.* **3**, 671 (2012).
232. Lovett, D. B., Shekhar, N., Nickerson, J. A., Roux, K. J. & Lele, T. P. Modulation of Nuclear Shape by Substrate Rigidity. *Cell. Mol. Bioeng.* **6**, 230–238 (2013).
233. Matyas, J. *et al.* Ligament tension affects nuclear shape in situ: an in vitro study. *Connect. Tissue Res.* **31**, 45–53 (1994).
234. Chancellor, T. J., Lee, J., Thodeti, C. K. & Lele, T. Actomyosin tension exerted on the nucleus through nesprin-1 connections influences endothelial cell adhesion, migration, and cyclic strain-induced reorientation. *Biophys. J.* **99**, 115–23 (2010).
235. Supryniewicz, F. A. *et al.* Conditionally reprogrammed cells represent a stem-like state

- of adult epithelial cells. *Proc. Natl. Acad. Sci. U. S. A.* **109**, 20035–40 (2012).
236. Tinevez, J.-Y. *et al.* Role of cortical tension in bleb growth. *Proc. Natl. Acad. Sci. U. S. A.* **106**, 18581–6 (2009).
237. Jankovics, F. *et al.* Transiently reorganized microtubules are essential for zippering during dorsal closure in *Drosophila melanogaster*. *Dev. Cell* **11**, 375–85 (2006).
238. Jacinto, A. *et al.* Dynamic Analysis of Dorsal Closure in *Drosophila*. *Dev. Cell* **3**, 9–19 (2002).
239. Jacinto, A., Martinez-Arias, A. & Martin, P. Mechanisms of epithelial fusion and repair. *Nat. Cell Biol.* **3**, E117–23 (2001).
240. Somà, A. & Ballestra, A. Residual stress measurement method in MEMS microbeams using frequency shift data. *J. Micromechanics Microengineering* **19**, 095023 (2009).

Appendix

Appendix A

Single cell-nanofiber interactions



Single cell-nanofiber interactions

a) The equation used to calculate the forces exerted by the DBTRG-05 MG cells is described below. Similar to previously reported force measurement strategies involving inverse methods, we modeled the fibers as a tie rod with lateral loading. The deflection of the beam obtained experimentally can be used to solve the forces causing the deflection. The structural stiffness of the beam (k), which varies along the length of the beam due to its suspension, can therefore be described by the following equation¹⁸⁸ :

$$k = \frac{-\sinh(\lambda(L-a)) \sinh(\lambda a)}{S\lambda \sinh(\lambda L)} + \frac{(L-a)a}{SL} \quad (i)$$

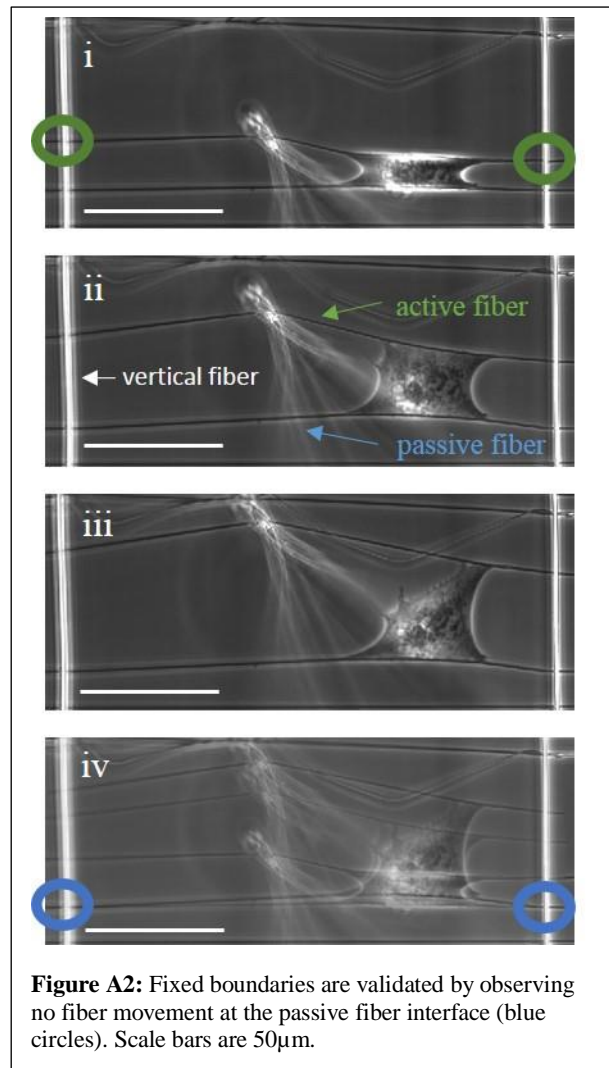
However, $F = k\delta$ in the linear domain, therefore:

$$F = \left(\frac{-\sinh(\lambda(L-a)) \sinh(\lambda a)}{S\lambda \sinh(\lambda L)} + \frac{(L-a)a}{SL} \right) \delta \quad (ii)$$

Where variables are defined as follows (Table 1):

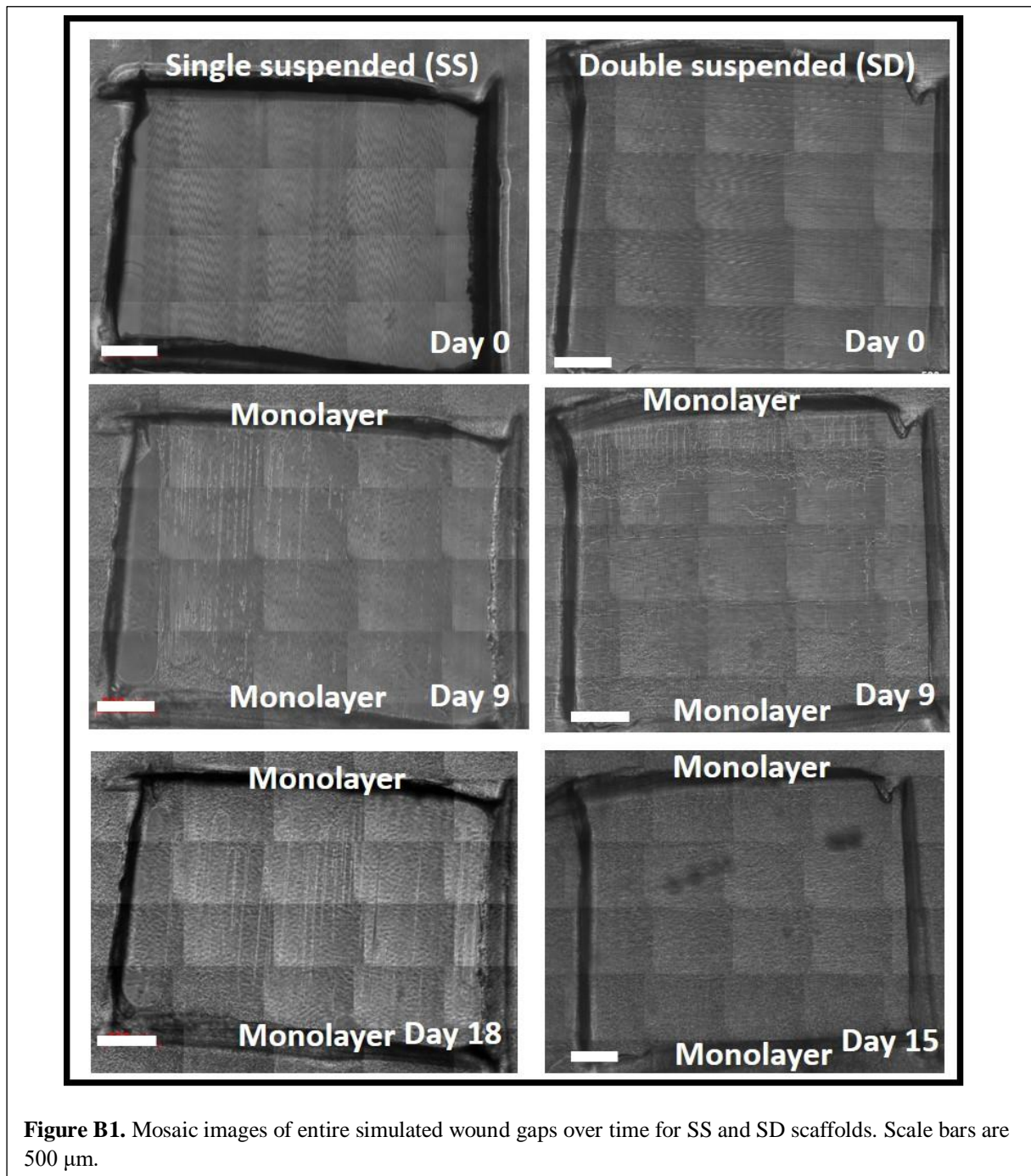
Nomenclature	Value
S (Tensile Force (N))	S= Tensile Stress (4.1MPa) * Cross sectional area of the nanofiber ([2] and Nain unpublished data)
d (Diameter (nm))	200-300
E (Young's modulus (GPa))	E = 0.97 (Obtained from AFM measurements, [2] and Nain unpublished data)
I (Moment of Inertia (m ⁴))	$I = \frac{\pi d^4}{64}$
λ (Lambda (m ⁻¹))	$\lambda = \left(\frac{S}{EI}\right)^{0.5}$
L (Length of the fiber between fixed ends (μ m))	Variable: 100-500
a (Location of intermediate load (m))	$0 < a < L$
δ (Fiber deflection (m))	~3.1% of L for inside-out; ~4.2% of L for outside-in

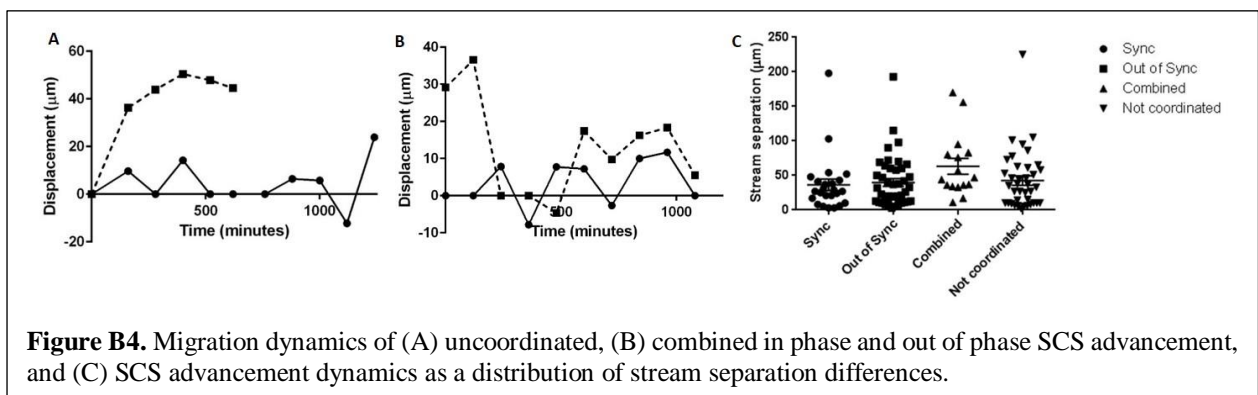
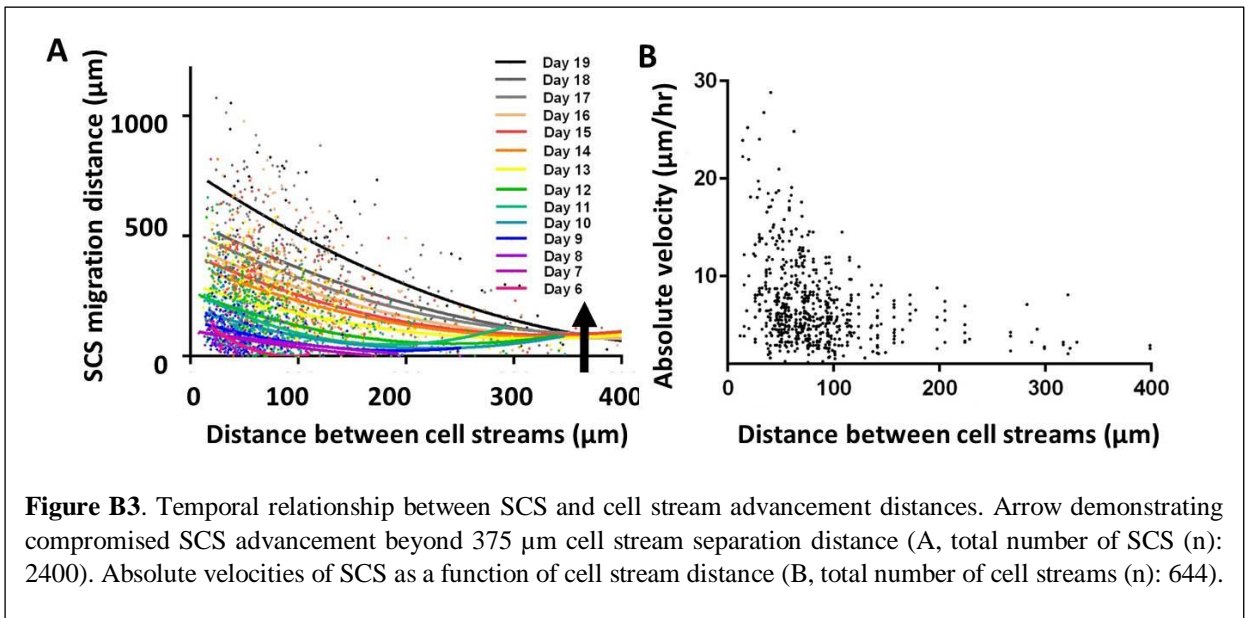
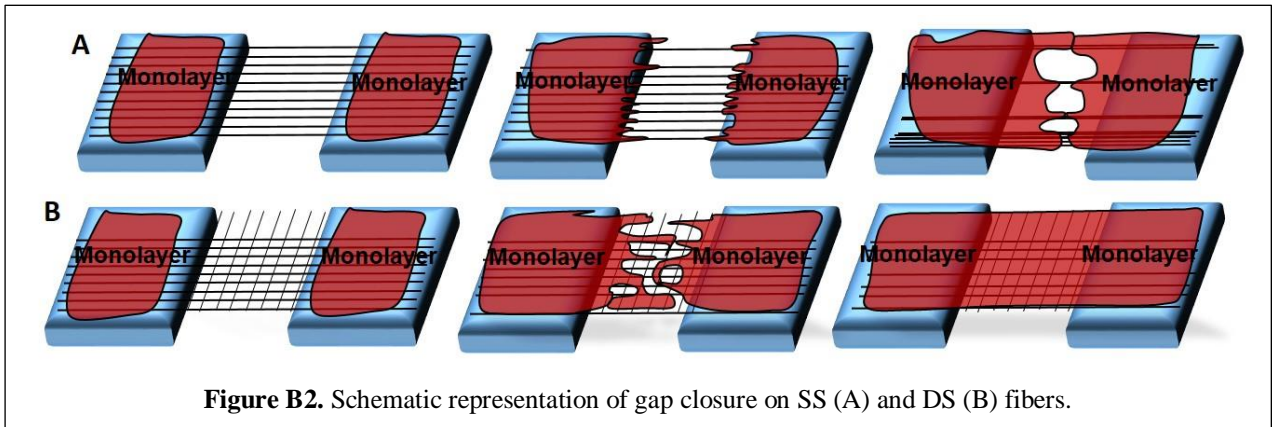
b) Maintenance of fixed boundary conditions during force measurement experiments are demonstrated in Fig 10.2. In this figure, the nodes of the active leading fiber (in contact with the probe) have been broken (i) to avoid buckling of the fibers (shown in green). Upon actuation by the probe, both the active leading and passive trailing fibers demonstrated deflections ((ii) & (iii)), whereas the vertical fibers remained stationary and maintained the boundary conditions. This is also shown by stacking the images together (iv), where the blue circles represent the fixed nodes with no buckling.

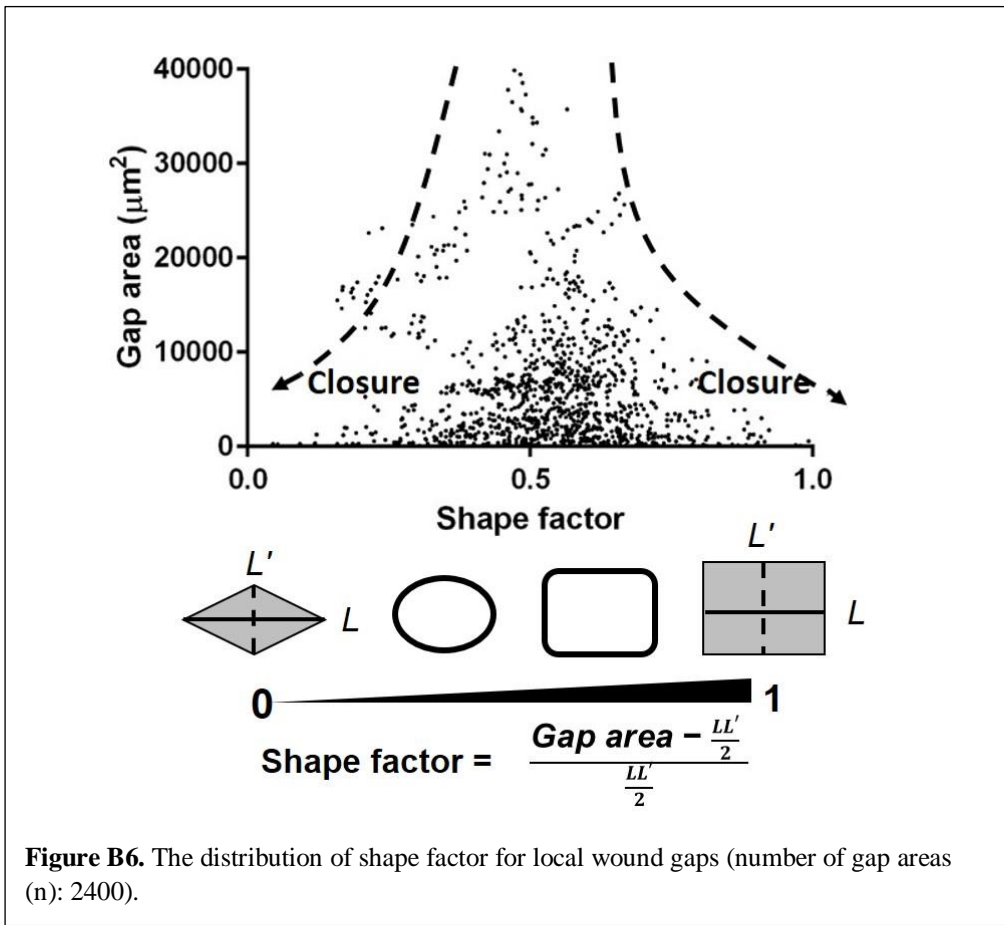
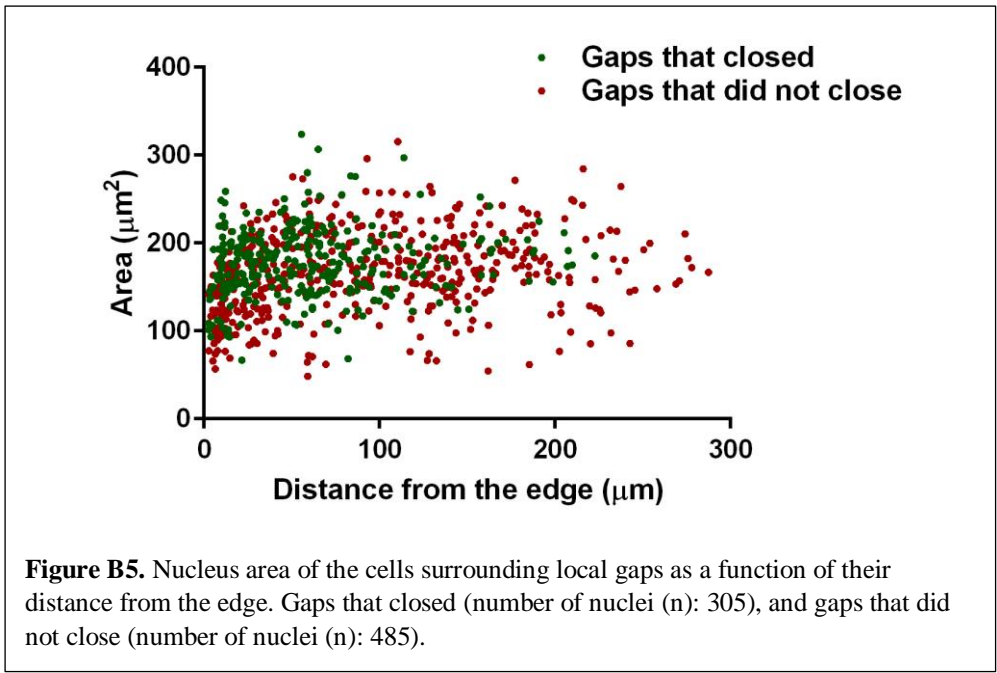


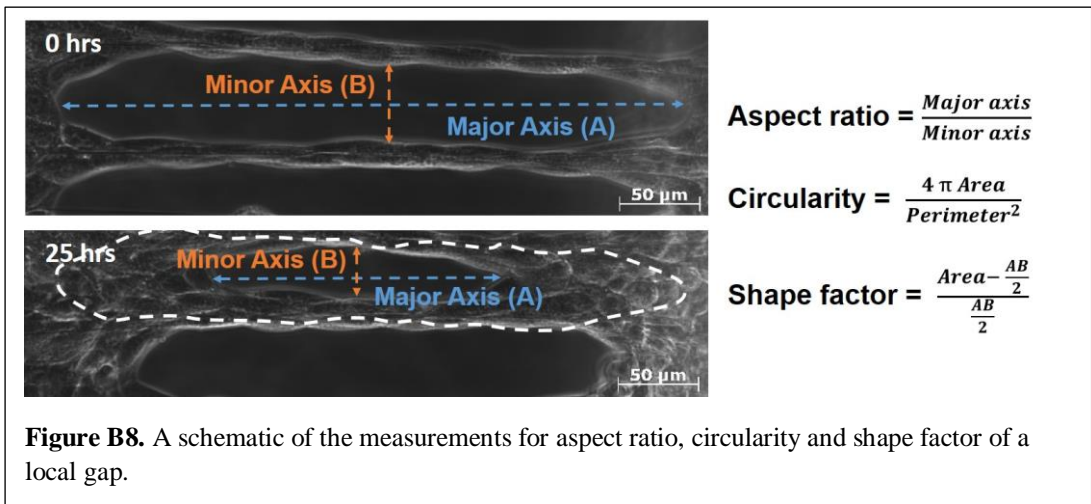
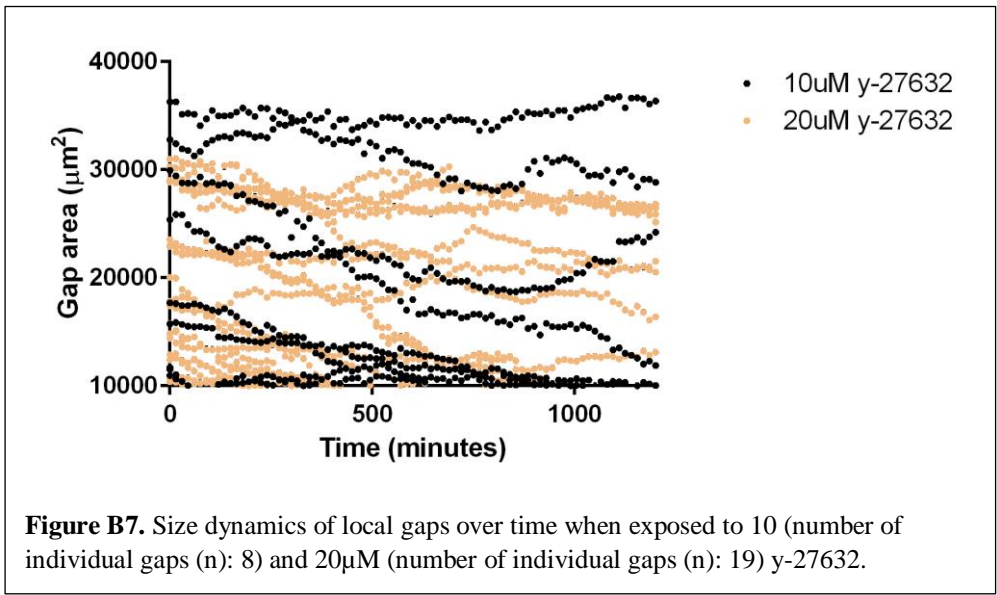
Appendix B

Collective cell migration dynamics









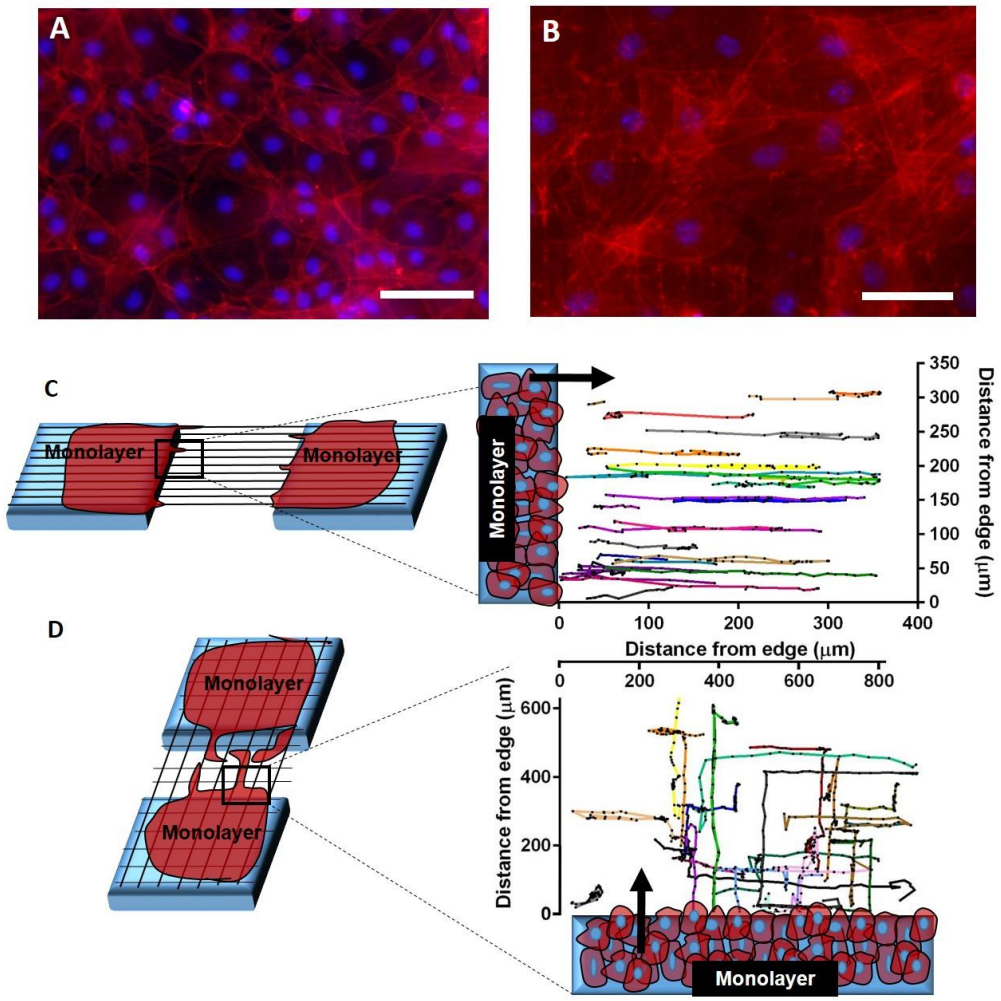


Figure B9. Immunostained images of cell monolayers showing the arrangement of cells on a flat substrate (A), and on SS or DS suspended fiber networks (B). (Red= Actin, Blue= Nucleus). Scale bars are 100 μm for A and 50 μm for B. Single cell migration pathways on SS (C, number of cells (n): 26) and DS (D, number of cells (n): 25) fibers.